Democratic and Popular Republic of Algeria

Ministry of High Education and Scientific Research

جامعة فرحات عباس سطيف

Ferhat ABBAS University of Setif

THESIS

Presented at the Faculty of Sciences

Department of Physics

To acquire the degree of

Doctor

Option: Condensed Matter Physics By

SELMA KARKOUR

Title

Ab initio study of some physical properties of the newly synthesized selenides Tl_2CdXSe_4(X = Ge, Sn).

Publicly discussed with the board of examiners on 02 /07/ 2024, which included the following members:

Mr. T. CHIHI	Professor	Univ. F. ABBAS SETIF 1	Chairman
Mr. A. BOUHEMADOU	Professor	Univ. F. ABBAS SETIF 1	Supervisor
Mr. K. HADDADI	Professor	Univ. F. ABBAS SETIF 1	Co-supervisor
Mr. D. ALLALI	M.C.A	Univ. M. BOUDIAF M’SILA	Examiner
Mr. S. S. SAOUD	M.C.A	Univ. M. BOUDIAF M’SILA	Examiner
Mr. R. MISSOUM	M.C.A	Univ. Y. FARES, MEDEA	Examiner

Acknowledgment

First and last thanks to Allah who gives me the power to go forward in a way illuminated with His merciful guidance.

I would like to express my deep and sincere gratitude to my research supervisor Prof. Dr. A. BOUHEMADOU, Department of Physics, Laboratory for Developing New Materials and Their Characterization, for giving me the chance to be one of his students and for his generous advice, patience, and valuable discussions, which helped me greatly. It was a great privilege and honor to work and study under his guidance. I am extremely grateful for what he has offered me.

I would like to express my thanks to co-supervisor Prof. Dr. K. HADDADI, Physics and Chemistry of Materials Lab.

I would like to thank my thesis committee members

I am thankful to all members and colleagues, Laboratory for Developing New Materials and Their Characterization, and Solid State Department for their support and appreciated help.

I am so grateful to all my teachers and professors throughout my academic career, from elementary school to the University. Especially my teacher in elementary school, Abdehamid Boukari.

I express deep gratitude towards my parents for their unwavering love, prayers, care, and sacrifices in educating and equipping me for my future endeavors. I am immensely thankful to my husband for their love, understanding, prayers, and continuous support throughout the completion of this research work. Additionally, I extend my appreciation to my mother and father-in-law, sister, brother, sister-in-law, and brother-in-law for their unwavering support and invaluable prayers. I would like to extend a special thanks to my friend for their sincere interest and assistance in completing this thesis.

Dedication

To my Mother my Heaven
To my *father my inspiration*
To **my husband**

S.Karkour

Abstract

Motivated by the increasing need for high-performance semiconductor materials, we conducted a comprehensive investigation into the structural, elastic, electronic, and optical properties of two recently synthesized compounds, namely $Tl_2CdGeSe_4$ and $Tl_2CdSnSe_4$, using the full potential linearized augmented plane wave (FP-LAPW) and pseudopotential plane wave (PP-PW) employing density functional theory calculations. The calculations were carried out with the inclusion of relativistic effects, specifically accounting for spin-orbit coupling (SOC). The resulting equilibrium structural parameters obtained from the computations exhibit remarkable agreement with available measurements. It should be noted that the calculations for all the properties examined were carried out using the theoretic equilibrium lattice parameters. The obtained results for both monocrystalline and polycrystalline elastic constants indicate that the investigated compounds exhibit softness, ductility, mechanical stability, and significant structural and elastic anisotropy. By employing the Tran-Blaha modified Becke-Johnson potential and considering the inclusion of spin-orbit coupling (SOC), our calculations reveal that both $Tl_2CdGeSe_4$ and $Tl_2CdSnSe_4$ are direct bandgap semiconductors. Incorporating SOC leads to a reduction in the fundamental bandgap of $Tl_2CdGeSe_4$ from 1.123 to 0.981 eV and that of $Tl_2CdSnSe_4$ from 1.097 to 0.953 eV. The l-decomposed atom-projected densities of states were utilized to determine the individual contributions of each constituent atom to the electronic states within the energy bands. The upper valence subband predominantly arises from the Se-4p states, while the bottom of the conduction band primarily originates from the Se-4p and Ge-4p/Sn-5p states. Furthermore, frequency-dependent linear optical parameters, including the complex dielectric function, absorption coefficient, refractive index, reflectivity, and energy-loss function, were calculated across a wide energy range for electromagnetic waves polarized parallel and perpendicular to the c-axis. Efforts were made to elucidate the microscopic origins of the observed peaks and structures in the calculated optical spectra.

Keywords: First-principles calculations; Spin-orbit coupling; Effective masse; DFT; FP-LAPW; GGA; TB-mBJ.

ملخص

بدافع الحاجة المتزايدة لمواد أشباه الموصلات عالية الأداء، أجرينا تحقيقًا شاملاً في الخصائص البنيوية والمرنة والإلكترونية والضوئية لمركبين تم تصنيعهما مؤخرًا، وهما $Tl_2CdGeSe_4$ و$Tl_2CdSnSe_4$ ، ، وذلك باستخدام الموجة المستوية المتزايدة خطيا (FP-LAPW) والموجة المستوية الكاذبة (PP-PW) اللذان يستخدمان حسابات نظرية دالية الكثافة. تم إجراء الحسابات مع تضمين التأثيرات النسبية ، على وجه التحديد لحساب اقتران الدوران والمدار(SOC) . تظهرنتائج الثوابت البنيوية للتوازن التي تم الحصول عليها من الحسابات اتفاقًا ملحوظًا مع القياسات المتاحة. وتجدر الإشارة إلى أن العمليات الحسابية لجميع الخصائص التي تم فحصها أجريت باستخدام ثوابت شبكة التوازن النظري. النتائج التي تم الحصول عليها لكل من الثوابت المرنة أحادية البلورية ومتعددة التبلور تشير إلى أن المركبات التي تم فحصها تظهر ليونة ، صلابة، إستقرار ميكانيكي ، وتباين بنيوي ومرن كبير. من خلال استخدام كمون Becke-Johnson المعدلة من Tran-Blaha والنظر في ادخال اقتران مدار الدوران (SOC)، تكشف حساباتنا أن كلا من $Tl_2CdGeSe_4$ و $Tl_2CdSnSe_4$ هما أشباه نواقل ذات فجوة نطاق مباشرة. يؤدي دمج SOC إلى تقليل فجوة النطاق الأساسية لـ $Tl_2CdGeSe_4$ من 1.123 إلى 0.981 فولت وتلك الخاصة بـ $Tl_2CdSnSe_4$ من 1.097 إلى 0.953 فولت. تم استخدام كثافات الدول المتحللة لتحديد المساهمات الفردية لكل ذرة مكونة للحالات الإلكترونية داخل نطاقات الطاقة. ينشأ النطاق الفرعي التكافؤ العلوي في الغالب من حالات Se-4p، بينما ينشأ الجزء السفلي من نطاق التوصيل بشكل أساسي من حالات Se-4p و Ge-4p / Sn-5p. علاوة على ذلك ، تم حساب اطياف الدوال الضوئية المعتمدة على التردد ، بما في ذلك دالة العزل الكهربائي المعقدة ، ومعامل الامتصاص ، ومعامل الانكسار ، والانعكاسية ، ووظيفة فقدان الطاقة ، عبر نطاق طاقة واسع للموجات الكهرومغناطيسية المستقطبة المتوازية والعمودية على المحورc .بُذلت جهود لتوضيح الأصول المجهرية للقمم والتراكيب التي لوحظت في الأطياف الضوئية المحسوبة .

الكلمات المفتاحية: حسابات المبادئ الأولية؛ اقتران دوران المدار؛ كتلة فعالة؛ GGA؛ TB-mBJو DFT؛ FP-LAPW.

Résumé

Motivés par le besoin croissant de matériaux semi-conducteurs hautes performances, nous avons mené une enquête approfondie sur les propriétés structurelles, élastiques, électroniques et optiques de deux composés récemment synthétisés, à savoir $Tl_2CdGeSe_4$ et $Tl_2CdSnSe_4$, en utilisant l'onde plane augmentée linéarisée à plein potentiel (FP-LAPW) et l'onde plane pseudopotentielle (PP-PW) en utilisant des calculs de théorie fonctionnelle de la densité. Les calculs ont été effectués en tenant compte des effets relativistes, notamment en tenant compte du couplage spin-orbite (SOC). Les paramètres structurels d'équilibre résultants obtenus à partir des calculs présentent un accord remarquable avec les mesures disponibles. Il convient de noter que les calculs pour toutes les propriétés examinées ont été effectués en utilisant les paramètres de réseau d'équilibre théoriques. Les résultats obtenus pour les constantes élastiques monocristallines et polycristallines indiquent que les composés étudiés présentent une douceur, une ductilité, une stabilité mécanique et une anisotropie structurelle et élastique significative. En utilisant le potentiel de Becke-Johnson modifié par Tran-Blaha et en tenant compte de l'inclusion du couplage spin-orbite (SOC), nos calculs révèlent que $Tl_2CdGeSe_4$ et $Tl_2CdSnSe_4$ sont des semi-conducteurs à bande interdite directe. L'incorporation de SOC conduit à une réduction de la bande interdite fondamentale de $Tl_2CdGeSe_4$ de 1.123 à 0.981 eV et celle de $Tl_2CdSnSe_4$ de 1.097 à 0.953 eV. Les densités d'états projetées par les atomes l-décomposés ont été utilisées pour déterminer les contributions individuelles de chaque atome constitutif aux états électroniques dans les bandes d'énergie. La sous-bande de valence supérieure provient principalement des états Se-4p, tandis que la partie inférieure de la bande de conduction provient principalement des états Se-4p et Ge-4p/Sn-5p. De plus, les paramètres optiques linéaires dépendant de la fréquence, y compris la fonction diélectrique complexe, le coefficient d'absorption, l'indice de réfraction, la réflectivité et la fonction de perte d'énergie, ont été calculés sur une large gamme d'énergie pour les ondes électromagnétiques polarisées parallèlement et perpendiculairement à l'axe c. Des efforts ont été faits pour élucider les origines microscopiques des pics et des structures observées dans les spectres optiques calculés.

Mots-clés: Calculs ab-initio; Couplage spin-orbite; Masse efficace; DFT; FP-LAPW; GGA; TB-mBJ.

Contents

General introduction

Chapter I: Density Functional Theory (DFT)

Chapter II: Pseudo-Potential Plane Wave and Full-Potential Linearized Augmented Plane Wave

Chapter III: Results and Discussion

Appendix

List of Symbols

Ψ	Wave function.
$\hat{H}$	Hamiltonian operator.
DFT	Density Functional Theory.
ρ	Electronic density.
HK	Hohenberg and Kohn.
KS	Kohn-Sham.
XC	Exchange-Correlation.
LDA	Local Density Approximation.
GGA	Generalized Gradient Approximations.
PBEsol	Perdew-Burke-Ernzerhof functional for Solids.
BJ	Becke and Johnson.
TB-mBJ	Tran-Blaha modified Becke-Johnson
PP	Pseudo-potential
APW	Augmented Plane Wave.
FP-LAPW	Full-potential linearized augmented plane wave.
LO	Local orbitals.
MT	muffin-tin.
E_l	Linearization energies.
U_l	Radial functions.
SG	Space groupe.
NN	Nearest neighbor
BZ	Brillouin zone.
a.u	Atomic unit.

E_i	Internal energy
C_{ij}	Elastic constants.
B	Bulk modulus.
G	Shear modulus.
E	Young’s modulus
H_V	Vicker’s hardness
B/G	Pugh’s indicator.
σ	Poisson’s coefficient.
T_D	Debye temperature.
v_m	Average sound wave velocity.
v_t	Transversal sound velocities.
v_l	Longitudinal sound velocities.
A^U	Universal anisotropy.
E_g	Band gap energy.
VB	Valence Band.
CB	Conduction Band.
E_F	Fermi level energy.
SOC	Spin-orbit coupling.
m^*	Effective charge-carrier mass.
T-DOS	Total Density of States.
P-DOS	Partial Density of States.
ε	Dielectric function.
ω	frequency
α	Absorption coefficient.

n	Refractive index.
k	Extinction coefficient.
R	Reflectivity.

List of Figures

Chapter I

Chapter II

Chapter III

Appendix

List of Tables

Chapter III

GENERAL INTRODUCTION

General Introduction

1. Preamble

The field of condensed matter physics and materials science has yielded numerous exciting discoveries, leading to the development of new materials and their subsequent applications. These advancements are closely tied to our comprehension and utilization of interacting systems involving electrons and nuclei. Understanding and describing the fundamental interactions within such systems necessitates the application of the laws of quantum mechanics and electrostatics.

Computational materials science endeavors to unravel the various properties and phenomena exhibited by materials, as well as to design and fabricate improved materials that contribute to scientific and technological progress. This field employs computer-based modeling techniques, employing theories and algorithms rooted in physics, mathematics, chemistry, materials science, and computer science. In many instances, computational approaches become indispensable when dealing with materials under extreme and inhospitable conditions that cannot be replicated in a laboratory setting, such as high pressures, elevated temperatures, exposure to hazardous substances or nuclear radiation, or due to material cost considerations.

Presently, computational materials science has transitioned from being a specialized subject to a commonplace and routine practice. It has become as familiar as analyzing X-ray diffraction (XRD) patterns or examining scanning electron microscopy (SEM) or transmission electron microscopy (TEM) images. Moreover, the significance of computational materials science is widely acknowledged, with many scientists embracing the approach of "computation first, then experiment" or advocating for "material design by computation" [1].

The properties of a solid are predominantly governed by the behavior of its electrons. To model and predict these properties, the field of materials science employs a variety of theoretical and computational methods for electronic structure calculations. These methods encompass highly accurate ab initio quantum chemistry techniques, which operate based on explicitly correlated multi-electron wave functions. These techniques are rooted in quantum theory and do not rely on any adjustable or empirical parameters. The only essential input data are the atomic numbers of the constituent atoms and initial structural information. Semi-empirical methods, on the other hand, rely on atomic parameters and experimental data to predict properties that have not been determined experimentally. Empirical methods utilize experimental data to determine the values of specific parameters. In the realm of electronic structure calculations, first-principles simulations have emerged as a dependable and computationally feasible tool in condensed matter physics. These simulations employ density functional theory, specifically utilizing approximations such as the local density approximation (LDA) and generalized gradient approximations (GGA). Overall, these theoretical and computational approaches play a vital role in materials science, enabling researchers to model and predict the properties of materials with a high degree of accuracy and computational efficiency.

In this thesis, the focus lies on performing quantum-mechanical calculations to determine the optimized structural parameters and monocrystalline and polycrystalline elastic moduli of the considered materials. To achieve this, an efficient method called the pseudopotential plane wave (PP-PW) approach, which is based on density functional theory (DFT), was employed. These calculations were carried out using the Cambridge Sequential Total Energy Package (CASTEP) software [2]. To investigate the electronic and optical properties of the materials under study, another computational method known as the full-potential (linearized) augmented plane wave plus local orbitals (FPL/APW+lo) was utilized. This approach, implemented in the WIEN2k code [3], is recognized as one of the most accurate methods for calculating electronic structures and related properties.

2. Problematic, Statement of the problem and research objectives

Semiconductors have garnered significant attention from researchers due to their versatile applications in various fields. Alkali metals based on chalcogenide materials have particularly gained high regard for their potential in a wide range of technologies. In 1965, it was recognized that binary chalcogenides could be intercalated with different species, including alkali metals. Subsequently, in 1967, HAHN and STRICK [4] attempted to synthesize quaternary chalcogenides with metals, resulting in the formation of compounds with the general formula $CuC^{III}D^{IV}X_4$ (where C^{III} represents elements such as B, Al, Ga, In; D^{IV} denotes elements like Si, Ge, Sn; and X stands for S, Se, Te).

In recent years, extensive research has been conducted on the semiconducting and optical properties of ternary and quaternary chalcogenides, where oxygen atoms in silicates, germinates, and stannates are replaced with S, Se, or Te. These compounds are of interest from a structural perspective as they exhibit various anionic groups formed by connecting a fundamental structural unit, $D^{IV}X4$ (D^{IV} = Si, Ge, Sn; X = S, Se, Te), in a tetrahedral configuration [5]. Furthermore, compounds with general compositions A^{I}_{2} $B^{II}D^{IV}X_2$ (where A^{I} represents elements like Cu, Ag; B^{II} represents Cd, Zn; D^{IV} denotes Sn, Ge; and X stands for S, Se) were synthesized by researchers [6]. Additional investigations have focused on two-dimensional or layered metal chalcogenides with different quaternary systems, such as $A^{I}/Cu/D^{IV}/X$ (A^{I} = Na, K, Cs, Tl; D^{IV} = Ti, Zr; X =S, Se, Te) and $A^{I}Cu_2E^{V}X_4$ (E^{V} = Nb, Ta) systems, as well as ternary $A^{I}D^{IV}X$ (D^{IV} = Zr, Hf) systems [6; 7]. The study of metal chalcogenides is motivated by the structural differences observed between metal oxides and metal chalcogenides [8]. The Roman numerals in the formula correspond to the number of valence electrons, while the subscripts indicate the quantity of that particular ion in the formula unit. Throughout the years, leading up to the 20th century, scientists explored various elemental forms in the case of A^{I}, including alkali metals, alkaline earth metals, other metals like thallium, and transition metals like copper, silver, and gold, resulting in several formulas for quaternary chalcogenides. In this study, we specifically focus on the compound with the formula $A^{I}_{2}B^{II}D^{IV}X_4$.

Quaternary chalcogenide compounds described by the formula $A^{I}_{2}B^{II}$ $D^{IV}X_4$ (2-1-1-4), where A^{I} represents Cu or Ag, B^{II} represents Zn, Cd, or Hg, D^{IV} represents Si, Ge, or Sn, and X represents S, Se, or Te, have been extensively studied and documented in the literature [9; 10-13]. These compounds are often synthesized in quasi-binary or quasi-ternary systems and predominantly crystallize in tetragonal structures, such as stannite (space group I-42m) or kesterite (space group I-4). In some cases, an orthorhombic structure, known as the Wurtz-stannite structure, is observed, which is derived from the sphalerite or wurtzite structure. This structure is characterized by the tetrahedral coordination of atoms [14].

Since the early 20th century, numerous experimental and theoretical studies have been conducted on quaternary chalcogenides involving copper, silver, and alkali metals [10-24]. Compounds with A^{I} = Li, such as Li_2ZnGeS_4 [15], $Li_2Hg(Si/Ge/Sn)S_4$, $Li_2Cd(Ge/Sn)S_4$[25], and $Li_2Cd(Sn/Ge)Se_4$[16], crystallize in an orthorhombic structure with space group Pna21 (no: 33). These materials have been extensively investigated for their nonlinear optical properties and as lithium ionic conductors for all-solid lithium batteries, offering potential solutions to safety concerns associated with rechargeable lithium-ion batteries using non-aqueous liquid electrolytes [25-28].

Compounds with A^I = Ag, such as Ag_2ZnSnS_4, $Ag_2HgSnSe_4$, Ag_2HgSnS_4, and Ag_2PbGeS_4, have also been synthesized [17-20]. These compounds exhibit noncentrosymmetric structures, making them suitable for nonlinear optics applications. Furthermore, A^I = Cu compounds, including $CuMn_2InSe_4$, $Cu_2Cd(Ge/Si)S_4$, $Cu_2Mg(Si/Ge)S_4$, $Cu_2CdSnSe_4$, and $Cu_2CdGeSe_4$, crystallize in various structures such as I-42m and at high temperatures Pmn21. These compounds have demonstrated promising properties in diverse applications [10-13; 24].

There are four known compounds with B^{II} = Pb, namely Cu_2PbSiS_4 [29], Ag_2PbGeS_4 [30], and Tl_2PbSiS_4 [31, 41], along with Tl_2PbGeS_4, discovered as early as 1980 [42]. These compounds contribute to improving efficiency in various applications [43]. Quaternary chalcogenides based on copper, silver, and alkali metals offer diverse stable crystal structures, compositional flexibility, high thermal stability, semiconductivity, photovoltaic effects, spintronics, non-linear optical properties, and favorable thermoelectricity. As a result, they find applications in photovoltaic cells, optoelectronics, nonlinear optical devices, and photocatalytic water splitting for hydrogen gas production [3-8; 25-28].

Despite their appealing properties, there are concerns regarding chalcogenides containing alkali metals. The low electronegativity and reactivity of alkali metals may hinder their technological applications. To overcome these drawbacks, researchers have explored substituting alkali metals with thallium (Tl) due to its similar chemistry to alkali metals while offering some advantageous properties. Tl has a lower electronegativity than alkali metals, leading to smaller bandgaps and improved charge carrier mobility. Additionally, Tl is heavier, resulting in lower lattice thermal conductivity and improved thermoelectric efficiency. Furthermore, Tl+ possesses a lone pair of electrons, making Tl-containing materials less sensitive to air and moisture compared to alkali metal-based compounds [35].

One interesting advantage of substituting alkali metals with thallium is the possibility of achieving isostructural compounds. By replacing an alkali metal atom with a Tl atom in a material, it is possible to maintain the same crystal structure. This characteristic has sparked significant research interest in exploring Tl-based chalcogenides as alternatives to alkali metal-containing chalcogenides [34; 35].

Despite numerous reports on the synthesis and characterization of Tl-based quaternary chalcogenides, such as $Tl_2B^{II}D^{IV}X_4$ (B^{II} = Mn, Cd, Hg, Pb, Fe, Zn; DIV = Si, Ge, Sn; X = S, Se, Te) systems [34–47], the research on these materials remains insufficient. However, their potential applications make them a subject of current interest.

Tl-based chalcogenides offer several advantages, including diverse crystal structures, compositional flexibility, high thermal stability, semiconductivity, photovoltaic effects, spintronics, and non-linear optical properties. Moreover, their potential as solid electrolytes in all-solid lithium batteries holds promise for resolving safety concerns associated with rechargeable lithium-ion batteries that employ non-aqueous liquid electrolytes.

In summary, quaternary chalcogenide compounds with the formula $A^{I}_2B^{II}D^{IV}X_4$, where A^I represents Cu and Ag or Li, B^{II} represents Zn, Cd, or Hg, D^{IV} represents Si, Ge, or Sn, and X represents S, Se, or Te, have attracted significant attention in research. Their unique properties and structural characteristics make them suitable for various applications in fields such as photovoltaics; optoelectronics, nonlinear optics, and energy storage [10-24]. The exploration of Tl-based chalcogenides as alternatives to alkali metal-based compounds offers opportunities to overcome certain limitations and improve their technological potential.

Quaternary chalcogenides based on thallium have shown great promise in the search for new phases and materials. The systems where A^I = Tl have been extensively studied with various formulas and compositions. For example, $Tl_2HgSnSe_4$, $Tl_2HgSiSe_4$, and $Tl_2HgGeSe_4$ were synthesized in 2012 by Mozolyuk [38; 39], and Tl_2PbSiS_4 with an orthorhombic structure (space group P21/a) was studied experimentally in 2017 by Mozolyuk and L. Piskach [31] and theoretically in 2019 [41]. In 1980, G. Eulenberger [42] investigated Tl_2PbGeS_4, which crystallizes in a monoclinic structure (space group P21/a). The thermoelectric properties of $Tl_2(Cd/Hg/Mn)(Ge/Sn)Te_4$ were measured by Michael A. in 2005 [35], and the six compounds in this series crystallize in the tetragonal space group I-42m. Selezen synthesized $Tl_2(Cd/Hg)(Si/Ge)(Se/Te)_4$ in 2020 [44], focusing on four compounds: $Tl_2CdGeSe_4$, $Tl_2CdSnSe_4$, $Tl_2CdSiTe_4$, and $Tl_2HgSiTe_4$, which all crystallize in the tetragonal space group I-42m. The crystal structures, formation conditions, absorption coefficient spectra, and some electronic properties of $Tl_2CdGeSe_4$ and $Tl_2CdSnSe_4$ have been studied [37; 44-47], including ab initio calculations of their band structures and optical coefficients [11; 13].

Previous studies combining experimental and theoretical approaches have shown that $Tl_2CdSnSe_4$ and $Tl_2CdGeSe_4$ could be very promising compounds for applications in solar cells, thin films, and optoelectronics [45]. Understanding the fundamental properties of a material, such as its structural, elastic, electronic, and optical properties, is crucial for predicting its potential applications [48]. However, to the best of our knowledge, the elastic properties of $Tl_2CdGeSe_4$ and $Tl_2CdSnSe_4$ have not yet been explored either experimentally or theoretically. In addition, there is still a need for in-depth theoretical exploration of the electronic and optical properties of these compounds. To address these gaps, we conducted a detailed investigation of the structural, elastic, electronic, and optical properties of the newly synthesized materials $Tl_2CdGeSe_4$ and $Tl_2CdSnSe_4$ using two complementary density functional theory (DFT) methods: pseudopotential plane wave (PP-PW) and full-potential (linearized) augmented plane wave plus local orbitals (FP-(L)APW + lo) methods. It's worth noting that DFT calculations have become a powerful tool for predicting the fundamental properties of materials and their applications, and they play a crucial role in both theoretical and applied studies [49; 50].

3.Thesis outline

In this thesis, we have conducted the following work:

The thesis is divided into two parts, in addition to the introduction and conclusion.

The first part:

The introduction provides the context of the thesis, outlines the themes addressed, discusses the state of the art prior to our work, specifies the objectives, and outlines the thesis structure.

Chapters 1 and 2 present the theoretical framework in which our work was conducted.

Chapter 1 covers the fundamentals of density functional theory (DFT) and the approximations used to handle exchange and correlation effects, such as the local density approximation (LDA), the generalized gradient approximation (GGA), and the Tran-Blaha modified Becke-Johnson potential (TB-mBJ).

Chapter 2 explains the principles of the pseudopotential plane wave (PP PW) method employed in the CASTEP code, as well as the linearized augmented plane waves (FP-LAPW) method implemented in the WIEN2k code.

The second part:

Chapter 3 presents the computational settings used in our study. We discuss and analyze the obtained results, including the crystal structure, elastic moduli, electronic structure, and optical coefficients and functions.

The thesis concludes with a general summary, highlighting the main findings of our study. Several appendices provide additional information on the CASTEP and WIEN2k programs, along with a brief overview of spin-orbit coupling.

We aim for the reported data to provide theoretical support to existing experimental and theoretical findings, while serving as a foundation for future experimental and theoretical investigations. Ultimately, our goal is to contribute towards a better understanding of the potential technological applications of the materials studied in this thesis.

References

[1] J. G. Lee, *Computational Materials Science An Introduction Second Edition*, ISBN 9781498749732 (2017).

[2] S.J. Clark, M.D. Segall, C.J. Pickard, P.J. Hasnip, M.J. Probert, K. Refson, M.C. Payne, *First principles methods using CASTEP*. J. Z. Kristallogr, Vol 220, No.4, pp. 567–570 (2005)

[3] S. Baroni, S. de Gironcoli, A. Dal Corso, P. Giannozzi, *Phonons and related crystal properties from density functional perturbation theory*. Rev. Mod. Phys, Vol 73, pp. 515–562 (2001)

[4] H. Hahn and G. Strick, *On Quaternary Chalcogenides of Zincblende-like Structure*, J. Naturwissenschaften. Vol. 54, pp. 225 (1967).

[5] Y. Nakamura, A. Aruga, I. Nakai, K. Nagashima, *Preparation and Characterization of the New Quaternary Chalcogenides TI-III-IV-*S_4 *(III= AI, Ga, In; IV = Si, Ge)*, Mat. Res. Bul., Vol.19, pp. 563-570, (1984).

[6] E. Parthe, K. Yvon, R.H. Deitch, *The crystal structure of* Cu_2CdGeS_4 *and other · quaternary normal tetrahedral structure compounds*, J. Acta Crystallogr. B. Vol. 25, pp. 1164-1174, (1969)

[7] Patricia M. Keane and James A. Ibers, *Synthesis of* K_4M3Te_{17} *(M = Zr, Hf) and the Structure of* $K_4Hf_3Te_{17}$*, a New One-Dimensional Solid-state Ternary Polytelluride*. J. Inorg. Chem, Vol. 30, pp. 1327-1329, (1991)

[8] Michael A. Pell and James A. *Layered Ternary and Quaternary Metal Chalcogenides*, J. Chemische Berichte, Vol.130, No. 1, pp 1-8 (1997)

[9] S. Saidia, S. Zriouelb, L.B. Drissib, M. Maaroufia, *First principles study of electronic and optical properties of* Ag_2CdSnS_4 *chalcogenides for photovoltaic applications*. J. Comp. Materials Science. Vol 152, pp. 291-299, 2018

[10] A.P. Litvinchuk, V.M. Dzhagan, V.O. Yukhymchuk, M. Ya. Valakh, I.S. Babichuk, O.V. Parasyuk, L.V. Piskach, O.D. Gordan, D.R.T. Zahn, *Electronic structure, Optical properties and lattice dynamics of orthorhombic* Cu_2CdGeS_4 *and* Cu_2CdSiS_4 *semiconductors*. Phys. Rev. B, Vol. 90, No. 16, pp. 165201–165208, 2014

[11] A. Bedjaoui, A. Bouhemadou, S. Aloumi, R. Khenata, S. Bin-Omran, Y. Al-Douri, F. Saad Saoud, S. Bensalem, *Structural, elastic, electronic and optical properties of the novel quaternary diamond-like semiconductors* Cu_2MgSiS_4 *and* Cu_2MgGeS_4, *J.* Solid State Sci. Vol 70, pp. 21–35, 2017

[12] C. Rincon, M. Quintero, E. Moreno, E. Ch Power, J.A. Quintero, M.A. Henao, Macıas, *Raman spectrum of* $Cu_2CdSnSe_4$ *stannite structure semiconductor compound*, J. Superlattices Microstruct, Vol. 88, pp. 99–103, 2015

[13] M.G. Brik, O.V. Parasyuk, G.L. Myronchuk, I.V. Kityk, *Specific features of band structure and optical anisotropy of Cu2CdGeSe4 quaternary compounds*. J. Mater. Chem. Phys, Vol. 147, pp. 155–161, 2014

[14] Schafer, W.; Nitsche, R. *Tetrahedral quaternary chalcogenides of the type* Cu_2*-II-IV-*$S_4(Se_4)$, J. Mater. Res. Bull. Vol. 9, pp. 645–654, 1974

[15] R. Kanno, T. Hata, Y. Kawamoto, M. Irie, *Synthesis of a new lithium ionic conductor, thio-LISICON–lithium germanium sulfide system. J.* Solid State Ion, Vol. 130, pp. 97–104, 2000

[16] J.-H. Zhang, D.J. Clark, A. Weiland, S.S. Stoyko, Y.S. Kim, J.I. Jang, J. Aitken, $Li_2CdGeSe_4$ *and* $Li_2CdSnSe_4$*: biaxial nonlinear optical materials with strong infrared second-order responses and laser-induced damage thresholds influenced by photoluminescence.* J. Inorg. Chem. Front. Vol. 4, pp. 1472–1484, 2017

[17] B.N. Schumer, R.T. Downs, K.J. Domanik, M.B. Andrade, M.J. Origlieri, Pirquitasite, Ag_2ZnSnS_4. Acta Cryst. E 69, i8–i9 (2013)

[18] O.V. Parasyuk, L.D. Gulay, L.V. Piskach, Yu.O. Kumanska, *The* Ag_2Se*–*$HgSe$*–*$SnSe_2$ *system and the crystal structure of the* $Ag_2HgSnSe_4$ *compound*, J. Alloys and Compounds, Vol 339, pp. 140–143, 2002

[19] O.V. Parasyuk, S.I. Chykhrij, V.V. Bozhko, L.V. Piskach, M.S. Bogdanyuk, I.D. Olekseyuk, L.V. Bulatetska, V.I. Pekhnyo, *Phase diagram of the* Ag_2S*–*HgS*–*SnS_2 *system and single crystal preparation, crystal structure and properties of* Ag_2HgSnS_4, J. Alloys and Compounds, Vol. 399, pp. 32–37, 2005

[20] Yu. Kogut, A. Fedorchuk, O. Zhbankov, Ya. Romanyuk, I. Kityk, L. Piskach, O. Parasyuk, *Isothermal section of the* Ag_2S*–PbS–*GeS_2 *system at 300 K and the crystal structure of* Ag_2PbGeS_4. J. Alloys Compd, Vol. 509, pp. 4264–4267, 2011

[21] O.V. Parasyuka, A.O. Fedorchuk, Yu.M. Kogut, L.V. Piskacha, I.D. Olekseyuka, *The* Ag_2S*–ZnS–*GeS_2 *system: Phase diagram, glass-formation region and crystal structure of* Ag_2ZnGeS_4. J. Alloys and Compounds, Vol. 500, pp. 26–29, 2010

[22] L. Piskachl, O. Velychko, A. Fedorchuk, Y. Kogut, I. Olekseyuk, O. Parasyuk, *Physico-chemical interaction in the* Ag_2Se*–Zn(Cd, Hg, Pb)–* $SnSe_2$ *systems. J.* Chem. Proc, 2021

[23] O.V. Parasyuk, L.D. Gulay, L.V. Piskach, I.D. Olekseyuk, *The Ag Se–CdSe–SnSe system at 670 K and the crystal structure of the* $Ag_2CdSnSe_4$ *compound*. J. Alloys and Compounds, Vol. 335, pp. 176–180, 2002

[24] L. Salik, A. Bouhemadou, K. Boudiaf, F. Saad Saoud, S. Bin-Omran, R. Khenata, Y. Al-Douri, A.H. Reshak, *Structural, elastic, electronic, magnetic, optical, and thermoelectric properties of the diamond-like quaternary semiconductor* $CuMn_2InSe_4$. J. Supercond. Nov. Magn. Vol. 33, pp. 1091–1102, 2020

[25] A. H. Reshak, *Revealing the origin of the strong second harmonic generation of* Li_2CdXS_4 *and* Li_2CdXS_4 *(X = Ge or Sn)*, J. Appl. Phys, 2016

[26] S. Alnujaim, A. Bouhemadou, A. Bedjaoui, S. BinOmran, Y. Al-Douri, R. Khenata, S. Maabed, *Ab initio prediction of the elastic, electronic and optical properties of a new family of diamond-like semiconductors,* Li_2HgMS_4 *(M = Si, Ge and Sn).* J. Alloys Compd. Vol. 843, pp. 155991–156014, 2020

[27] J.W. Lekse, M.A. Moreau, K.L. McNerny, J. Yeon, P. Shiv Halasyamani, J.A. Aitken, *Second-Harmonic Generation and Crystal Structure of the Diamond-like Semiconductors* Li_2CdGeS_4 *and* Li_2CdSnS_4*,* J. Inorg. Chem. Vol. 48, pp. 7516-7518, 2009

[28] Y. Huang, K. Wu, J. Cheng, Y. Chu, Z. Yang, S. Pan, Li_2ZnGeS_4*: A Promising Diamond-like Infrared Nonlinear Optical Material with High Laser Damage Threshold and Outstanding Second-Harmonic Generation Response*, J. Royal Society of Chemistry, 2013

[29] I.D. Olekseyuk, L.V. Piskach, O.Ye. Zhbankov, O.V. Parasyuk, Y.M. Kogut, *Phase diagrams of the quasi-binary systems* Cu_2S*–*SiS_2 *and* Cu_2SiS_3*–PbS and the crystal structure of the new quaternary compound* Cu_2PbSiS_4. J. Alloys and Compounds, pp. 399-149–154, 2005

[30] Y. Kogut, A. Fedorchuk, O. Zhbankova, Y. Romanyukc, I. Kityk, L. Piskacha, O. Parasyuka, *Isothermal section of the* Ag_2S*–PbS–*GeS_2 *system at 300 K and the crystal structure of* Ag_2PbGeS_4, *J.* Alloys and Compounds, Vol. 509, pp. 4264–4267, 2011

[31] M.Y. Mozolyuk, L.V. Piskach, A.O. Fedorchuk, I.D. Olekseyuk, O.V. Parasyuk, O.Y. Khyzhun, *The* Tl_2S*-PbS-*SiS_2 *system and the crystal and electronic structure of quaternary chalcogenide* Tl_2PbSiS_4, *J.* Materials Chemistry and Physics. Vol. 195, pp. 132-142, 2017

[32] G.Q. Yao, H.S. Shen, E.D. Honig, R. Kershaw, R. Dwight, A. Wold, *Solid State Ionics*, Vol. 24, pp. 249-252, 1981

[33] N. Greenwood, A. Earnshaw, *Chemistry of the Elements* (Pergamon Press, Elmsford, 1984)

[34] M.A. McGuire, T.K. Reynolds, F.J. DiSalvo, *Exploring thallium compounds as thermoelectric materials: seventeen new thallium chalcogenides*, J. Chem. Mater, Vol. 17, pp. 2875–2884, 2005

[35] M.A. McGuire, T.J. Scheidemantel, J.V. Badding, F.J. DiSalvo, Tl_2AXTe_4 *(A = Cd, Hg, Mn; X = Ge, Sn): crystal structure, electronic structure, and thermoelectric properties*, J. Chem. Mate, 2005

[36] A.A. Lavrentyev, B.V. Gabrelian, T.V. Vu, L.N. Ananchenko, G.L. Myronchuk, O.V. Parasyuk, V.A. Tkach, K.I. Kopylova, O.Y. Khyzhun, *Electronic and optical properties of quaternary sulfide* Tl_2HgSnS_4*, a promising optoelectronic semiconductor: a combined experimental and theoretical study, J.* Opt. Mater, Vol. 92, pp. 294–302, 2019

[37] A.O. Selezen, L.V. Piskach, O.V. Parasyuk, I.D. Olekseyuk, *The Tl2SnSe3-CdSe system and the crystal structure of the Tl2CdSnSe4 compound.* J. Phase Equilib. Diffus. Vol. 40, No. 6, pp. 797–801, 2019

[38] MYu. Mozolyuk, L.V. Piskach, A.O. Fedorchuk, I.D. Olekseyuk, O.V. Parasyuk, *Physico-chemical interaction in the* Tl_2Se*–HgSe–DIV*Se_2 *systems (DIV – Si, Sn), J.* Mater. Res. Bull, Vol. 47, pp. 3830–3834, 2012

[39] M. Yu Mozolyuk, L.V. Piskach, A.O. Fedorchuk, I.D. Olekseyuk, O.V. Parasyuk, *The Tl2Se–HgSe–GeSe2 system and the crystal structure of* $Tl_2HgGeSe_4$, J. Chem. Met. Alloys, Vol. 6, pp. 55–62, 2013

[40] L.V. Piskach, M. Yu Mozolyuk, A.O. Fedorchuk, I.D. Olekseyuk, O.V. Parasyuk, *Phase equilibria in the* Tl_2S*–HgS–*SnS_2 *system at 520 K and crystal structure of* Tl_2HgSnS_4*, J.* Chem. Met. Alloys, Vol. 10, pp. 136–141, 2017

[41] V. Vu, A.A. Lavrentyev, B.V. Gabrelian, H.D. Tong, O.V. Parasyuk, O.Y. Khyzhun, *Calculations within DFT framework of the electronic and optical properties of quaternary sulfide* Tl_2PbSiS_4*, a prospective optoelectronic semiconductor*, J. Comput. Condens. Matter, Vol. 21, (2019)

[42]G. Eulenberger, *Preparation and Crystal Structure of Dithallium (I) Lead(II) Tetrathiogermanate (IV) Tl2PbGeS4, J.* Naturforsch. Vol 35 b, pp. 335-339, 1980

[43] H. Nhalil, D. Han, Mao-Hua Du, S. Chen, D. Antonio, K. Gofryk, B. Saparov, *Optoelectronic properties of candidate photovoltaic* Cu_2PbSiS_4*,* Ag_2PbGeS_4 *and* KAg_2SbS_4 *semiconductors,* J. Elsevier, 2018

[44] A.O. Selezen, I.D. Olekseyuk, G.L. Myronchuk, O.V. Smitiukh, L.V. Piskach, *Synthesis and structure of the new semiconductor compounds* $Tl_2B^{II}D^{IV}X_4$ *(*B^{II}*–Cd, Hg;* D^{IV}*–Si, Ge; X–Se, Te) and isothermal sections of the* Tl_2Se*–CdSe–Ge(Sn)*Se_2 *systems at 570 K.* J. Solid State Chem, Vol. 289, pp. 121422–121427, 2020

[45] T.V. Vu, A.A. Lavrentyev, B.V. Gabrelian, A.O. Selezen, L.V. Piskach, G.L. Myronchuk, M. Denysyuk, V.A. Tkach, K.D. Pham, O.Y. Khyzhun, *Crystal growth, electronic and optical properties of* $Tl_2CdSnSe_4$*, a recently discovered prospective semiconductor for application in thin film solar cells and optoelectronics.* J. Opt. Mater. Vol. 111, pp. 110656–110712, 2021

[46] O.V. Parasyuk, V.S. Babizhetskyy, O.Y. Khyzhun, V.O. Levytskyy, I.V. Kityk, G.L. Myronchuk, O.V. Tsisar, L.V. Piskach, J. Jedryka, A. Maciag, M. Piasecki, *Novel quaternary* $TlGaSn_2Se_6$ *single crystal as promising material for laser operated infrared nonlinear optical modulators,* J. Curr. Comput.-Aided Drug Des, Vol. 7, pp. 341–416, 2017

[47] T.V. Vu, A.A. Lavrentyev, B.V. Gabrelian, A.O. Selezen, L.V. Piskach, I.D. Olekseyuk, G.L. Myronchuk, M. Denysyuk, V.A. Tkach, N.N. Hieu, K.D. Pham, O.Y. Khyzhun,

Quaternary $Tl_2CdGeSe_4$ selenide: electronic structure and optical properties of a novel semiconductor for potential application in optoelectronics. J. Solid State Chem, Vol. 302, pp. 122453–122513, 2021

[48] O.Y. Khyzhun, V.L. Bekenev, V.V. Atuchin, L.D. Pokrovsky, V.N. Shlegel, N.V. Ivannikova, *The electronic structure of Pb_2MoO_5: first-principles DFT calculations and X-ray spectroscopy measurements*, J. Mater. Des, Vol. 105, pp. 315–322, 2016

[49] P.K. Bayannavar, A.C. Mendhe, B.R. Sankapal, M.S. Sannaikar, S.K.J. Shaikh, S.R. Inamdar, R.R. Kamble, *Synthesis of metal free organic dyes: experimental and theoretical approach to sensitize one-dimensional cadmium sulphide nanowires for solar cell application.* J. Mol. Liq, Vol. 336, pp. 116862–116869, 2021

[50] S. Majumder, P.K. Baviskar, B.R. Sankapal, *Straightening of chemically deposited CdS nanowires through annealing towards improved PV device performance*, J. Ceram. Int, Vol. 42, pp. 6682–6691, 2016

Chapter I

Density Functional Theory (DFT)

Chapter I

I.1. Schrödinger equation of a crystal

The physical realm is constituted by electrons, which carry a negative charge, and a limited number (typically a few or a few hundred) of heavy nuclei with a positive charge. The overarching objective is to effectively characterize the attributes of a specific set of atoms by employing the principles of quantum mechanics, specifically by employing the time-independent Schrödinger equation in its simplest form.

$$\hat{H}\Psi = E\Psi \qquad \text{(I.1)}$$

E represents the energy of the lowest possible state in a crystal, which is known as the ground state. Ψ represents the wave function that describes the quantum system. H is the Hamiltonian operator, which is responsible for determining the total energy of a specific wave function. The specific form of H depends on the situation.

$$\hat{H}_{tot} = -\frac{\hbar}{2}\sum_{i=1}^{n}\frac{\nabla^2_{\vec{r}_i}}{m_e} - \frac{\hbar}{2}\sum_{I=1}^{N}\frac{\nabla^2_{\vec{R}_i}}{M} + \frac{1}{8\pi\epsilon_0}\sum_{i=1,\ j\neq i}^{n}\frac{e^2}{|\vec{r}_i-\vec{r}_j|} + \frac{1}{8\pi\epsilon_0}\sum_{I=1,\ J\neq I}^{N}\frac{e^2 Z_I Z_J}{|\vec{R}_I-\vec{R}_J|} - \frac{1}{4\pi\epsilon_0}\sum_{i=1}^{n}\sum_{I=1}^{N}\frac{e^2 Z_I}{|\vec{R}_I-\vec{r}_i|} \qquad \text{(I.2)}$$

ħ: Planck constant

m: The mass of the electron

r_i, r_j: are the positions of the electrons i and j, respectively.

M: is the mass of the nucleus.

R_I, R_J: are the positions of the nuclei I and J respectively.

Z_I, Z_J: are the atomic numbers of the nuclei I and J respectively.

In equation (I.2), the first two terms represent the kinetic energies of electrons and nuclei (T_e and T_N), the third and fourth terms represents the Coulomb repulsion between electrons, designated as V_{e-e}, and nucleis as V_{N-N}, and the fifth term represents the Coulomb attraction between electrons and nuclei, designated as V_{N-e}.

The Schrödinger equation (Eq. I.1) can be solved for systems with simple structures, such as the hydrogen atom, where only one nucleus and one electron. However, for solids, the system is described by the many-body problem, involving all the electrons and nuclei in the crystal lattice. In practice, dealing with such a large number of particles, typically on the order of 10^{23}, makes the problem extremely complex. The Hamiltonian (Eq. I.2) describes a strongly coupled system involving both electrons and nuclei. The last three terms in the Hamiltonian have a complex structure, making it challenging to solve the Schrödinger equation exactly. To address this complexity and find suitable approximate solutions, several methods are employed at three distinct levels: the Born-Oppenheimer approximation, density functional theory, and solving the Kohn-Sham equation.

I.2. Level 1: Born Oppenheimer approximation

A fundamental observation in the application of quantum mechanics to atoms is that the mass of atomic nuclei is significantly greater than that of individual electrons. Each proton or neutron in a nucleus possesses a mass that is more than 1800 times greater than that of an electron. This substantial disparity in mass implies that electrons exhibit considerably more rapid responses to changes in their surroundings than nuclei. Consequently, it becomes possible to distinguish between two components of our physical inquiries. We commence our analysis by examining the equations that describe the motion of electrons in the presence of fixed atomic nuclei. In this context, we determine the lowest energy configuration or state of the electrons while they interact with the nuclei. This state, designated the ground state of the electrons, represents the configuration with the lowest energy level. The division of nuclei and electrons into separate mathematical problems is referred to as the Born-Oppenheimer approximation. [1].

If this hypothesis is assumed, the nuclei lose all their kinetic energy, and the interaction energy among them remains constant, serving as a reference point for measuring energies.

$$\mathrm{H_{tot}} = \mathrm{H_e} + \mathrm{V_{N-N}} \qquad \text{(I.4)}$$

$$\mathrm{H_e} = \mathrm{T_e} + \mathrm{V_{N-e(ext)}} + \mathrm{V_{e-e}} \qquad \text{(I.5)}$$

The remaining energies in the system consist of the kinetic energy of the electron gas, the potential energy resulting from electron-electron interactions, and the potential energy of the electrons influenced by the external potential of the nuclei (which is now considered external to the system). This part is universal. However, the specific details regarding the nuclei involved and their positions are solely determined by the external potential, denoted as V_{ext} [2].

I.2.1. The Hartree and Hartree-Fock approximation

In an effort to describe the ground state of the many-electron system with a single determinant state, the Hartree approximation is employed. This approximation treats the electrons within an atom as if they were independently moving in an average potential. The average potential is formed by combining the external potential due to the nuclei and the

Coulomb potential originating from the electron density. In other words, in the Hartree approximation, each electron is treated as moving in an average potential that is determined by the combined influence of the external potential of the nuclei and the electron density itself.

$$\left[\frac{-h^2}{2m}\nabla^2 + V_{eff}(r_i, R)\right]\phi_i(r) = \varepsilon_i\phi_i(r) \qquad (I.6)$$

With

$$V_{eff}(r_i, R) = V_H(r_i) + V_{ext}(r_i) \qquad (I.7)$$

Where

$T_e = \langle \phi_e | \hat{T}_e | \phi_e \rangle$ is the kinetic energy of the electrons

$V_H = \langle \phi_e | \hat{V}_{e-e} | \phi_e \rangle$ The Hartree potential of electron-electron interactions

$V_{ext} = \langle \phi_e | \hat{V}_{e-n} | \phi_e \rangle$ The electron-nuclei potential interactions.

Using a variational argument, we obtain from this the single-particle Hartree equations:

$$\left\{-\frac{h^2}{2m}\nabla_i^2 + V_H(r_i) + V_{ext}(r_i)\right\}\phi(r_i) = \varepsilon_i\phi_i(r_i) \qquad (I.8)$$

$V_H(r_i)$ Called: Hartree potential. It is given by:

$$V_H(r_i) = ke^2\sum_{j\neq i}\left\langle \phi(r_i)\left|\frac{1}{|\vec{r}_i-\vec{r}_j|}\right|\phi(r_i)\right\rangle \qquad (I.9)$$

V_{ext}: is the external potential (Hartree effective field)

U_i: The Coulomb potential arising from the electron density

$$\left[\frac{-1}{2}\frac{h^2}{m}\Delta_i + U_i(r_i) + V_i(r_i)\right]\phi_i(r) = \varepsilon_i\phi_i(r) \qquad (I.10)$$

$$H_i = -\frac{h^2}{2m}\Delta_i + V(r) \qquad (I.11)$$

V(r) is the average potential and gives the approximate wave function in the product form as:

$$\phi_{Hartree}(r_1, r_2, \dots, r_N) = \phi^1(r_1)\phi^2(r_2), \dots, \phi^N(r_N) \qquad (I.12)$$

The Hartree equation necessitates a self-consistent solution. The density plays a pivotal role in determining the average potential, as postulated by Hartree [3]. However, the Hartree method fails to account for the impact of antisymmetry in many-electron wave functions (exchange) and the correlations between electrons. In this method, each electron is represented by an orbital, and the overall wave function is expressed as a product of [4].

In 1930, Fock [5] demonstrated that the Hartree wave function violates the Pauli Exclusion Principle. In constructing the Hartree wave function, the Pauli Exclusion Principle is respected by assigning only one electron with a specific spin to each orbital. However, if electrons are considered indistinguishable fermions (particles with a spin of 1/2), the overall wave function must be antisymmetric, meaning that it changes sign when any two electrons are interchanged. The fundamental premise of the Hartree-Fock theory is the utilization of a Slater determinant, which conveniently organizes the orbitals. [3, 6].

$$\phi \approx \Phi_{SD} = \frac{1}{\sqrt{N!}} \begin{vmatrix} \phi_1(\vec{r}_1) & \phi_2(\vec{r}_1) & \cdots & \phi_N(\vec{r}_1) \\ \phi_1(\vec{r}_2) & \phi_2(\vec{r}_2) & \cdots & \phi_N(\vec{r}_2) \\ \vdots & \vdots & & \vdots \\ \phi_1(\vec{r}_N) & \phi_2(\vec{r}_N) & \cdots & \phi_N(\vec{r}_N) \end{vmatrix} \qquad (I.13)$$

N! is the normalization constant.

The equation (I.10) system is self-consistently solvable, as the potential depends on the wave functions. This approximation yields satisfactory results, particularly in the context of molecular physics. However, in the case of extended systems, such as solids, it remains challenging to apply.

I.3. Level 2: Density Functional Theory

Despite its simplified form, Equation (Eq. I.5) presents a significant challenge in its resolution. Various techniques can be utilized to simplify this equation, including the Hartree-Fock (H.F.) method, which directly addresses the many-body wave function. While the Hartree-Fock method is highly effective for atoms and molecules, its accuracy is reduced when applied to solids.

However, a more contemporary and sophisticated methodology, Density Functional Theory (DFT), reinterprets the many-body problem using a considerably smaller mathematical entity, necessitating the utilization of considerably less information to encode it. In particular, the electron density, denoted as ρ, becomes a function of only three variables: x, y, and z. This transition from E[ϕ] to E[ρ] effectively reduces the computational effort required to comprehend the electronic properties of atoms, molecules, and solids.

The pioneering density-based technique for addressing many-electron systems (consisting of N electrons) was introduced by Thomas and Fermi in 1927 [7;8]. The Thomas-Fermi method, so named for its pioneers, approximates the kinetic energy expression associated with the homogeneous electron gas, which is expressed as a functional of the local electron density. This approximation assumes that electrons are non-interacting. The kinetic energy density, representing the kinetic energy per unit volume, pertains to non-interacting electrons moving within a constant potential.

Subsequently, Hohenberg and Kohn extended this approach to encompass any electronic system, including inhomogeneous electron gases [9].

I.3.1. Hohenberg-Kohn Theorems (HK)

Density Functional Theory (DFT) is a theoretical framework that aims to ascertain the fundamental characteristics of the ground state of a system containing a specific number of electrons interacting through Coulomb forces with fixed nuclei. The theory postulates that the total energy, denoted as E, of an interacting system of non-spin-polarized electrons within an external potential (such as the Coulomb potential arising from solid-state nuclei) can be precisely expressed as a functional of the electronic density ρ in its ground state [10] .

The formulation of DFT, known as Hohenberg-Kohn (HK), is based on two pivotal theorems introduced by Hohenberg and Kohn in 1964 [5]. These theorems represent a departure from the conventional approaches to the problem.:

First theorem: The Density as a Basic Variable

The first Hohenberg-Kohn theorem is stated as follows:

« The external potential Vext(r) is (to within a constant) a unique functional of ρ(r); since in turn, Vext(r) fixes the Hamiltonian, we see that the full many-particle ground state is a unique functional of ρ(r) » [9].

This theorem can be proved by assuming a group of an arbitrary number of electrons, enclosed within a large box and subject to an external potential V(r) as well as mutual Coulomb repulsion. Additionally, let us assume that another potential V'_{ext} (r), characterized by a ground state ρ_0, yields the same density ρ(r). It is important to note that we are exclusively considering situations where the ground state is nondegenerate. By applying Rayleigh-Ritz's variational principle, we have [11]:

$$E < \rho(r)[V_{ext}(r) - V'_{ext}(r)]dr + E' \int dr^3 \quad ...... (1)$$

$$E' < \rho(r)[V'_{ext}(r) - V_{ext}(r)]dr + E \int dr^3 \quad ...... (2)$$

The combination of the two equations (1) and (2) leads to the following contradiction: E + E′< E + E′! . We reached a contradiction in the inequality because, for a non-degenerate system, there cannot be two distinct external potentials producing the same ground-state Density Functional Theory density (unless they differ only by an insignificant additive constant); the potential Vext(r) can be uniquely determined based on the ground state density. It is important to note that this demonstration, which relies on the variational principle, applies exclusively to the ground state.

The consequence of this initial theorem is that the ground state density serves as an exclusive determinant for various aspects:

- The external potential and the system's Hamiltonian with the exception of a constant term.
- By solving the Schrödinger equation utilizing this Hamiltonian, the wave function of any state can be determined. This includes the unique ground state wave function, which possesses the lowest energy [12].

By this theorem, the total energy of interacting electrons in an external potential is precisely expressed as a functional of the ground state electronic density ρ

$$E = E[\rho] \qquad (I.14)$$

$$E_{[\rho]} = \langle \phi | H | \phi \rangle \qquad (I.15)$$

$$= \langle \phi | T + V_{e-e} + V_{ext} | \phi \rangle \qquad (I.16)$$

$$= \langle \phi | T + V_{e-e} | \phi \rangle + \langle \phi | V_{ext} | \phi \rangle \qquad (I.17)$$

$$E_{[\rho]} = F_{HK}\,[\rho] + \int \rho\,(r)\,V_{ext}\,dr \qquad (I.18)$$

The functional $F_{HK}[\rho]$ is a universal functional applicable to any many-electron system, irrespective of the external potential. This functional incorporates exchange and correlation effects. The question that arises is how to identify the ground state density and determine the universal functional. The second theorem is of assistance in answering this question.

Second theorem: The variational principle

The total energy functional of any many-particle system attains its minimum value when the density is equal to the exact density of the ground state. Consequently, to ascertain the energy of the ground state, it is necessary to seek to minimize the functional energy. This can be achieved by applying an analogous variational principle.

« Hohenberg and Kohn demonstrated that, for a potential $V_{ext}(r)$ and a given number of electrons N, the system's total energy attains its minimum when the density ρ(r) corresponds to the exact density of the ground state. »

$$E\,[\rho_0] = \text{Min } E[\rho] \qquad (I.19)$$

it remains to formally determine $F_{HK}\,[\rho]$:

$$F_{HK}\,[\rho]=T[\rho(r)] + V_{ext}\,[\rho(r)] \qquad (I.20)$$

To effectively employ the theorems of Hohenberg and Kohn, it is necessary to utilize approximations that align with the Kohn-Sham equations [13]. These equations were developed to establish the fundamental principles required to use the theorems above.

II.3.2 The Kohn-Sham equations

Kohn and Sham transformed Density Functional Theory (DFT) into a practical tool by relying on the Hohenberg-Kohn equation. The innovative concept involves substituting the complex system of N interacting real particles, which is challenging to analyze, with a hypothetical system of independent, non-interacting particles (a fictitious system). This alternative system is easier to study and is constructed such that, in the ground state, both systems share the same density. The approach begins with a reference Hamiltonian where the electrons do not interact with each other and are influenced solely by the effective external Kohn-Sham potential. Furthermore, they employed the total energy functional, which encompasses the precise kinetic and electron-electron potential energy functionals, to identify the correlation energy.

$$E_e = T + V \qquad (I.21)$$

$$E_{HF} = T_0 + \underbrace{(V_H + V_x)}_{V} \qquad (I.22)$$

By subtracting (I. 22) from(I. 21), the functional correlation contribution appears to be:

$$Vc = T - T_0 \qquad (I.23)$$

With the Hartree functional given by:

$$E_H = \mathrm{T}_0 + V_H \qquad (\mathrm{I.}\,24)$$

Because exchange contribution is, absent in the Hartree solution so:

$$V_H = \mathrm{V} - V_X \qquad (\mathrm{I.}\,25)$$

Then $\mathrm{Vx} = \mathrm{V} - \mathrm{V_H}$ $\qquad (\mathrm{I.}\,26)$

The Hohenberg-Kohn functional can be rewritten in the following manner:

$$\mathrm{F_{HK}} = \mathrm{T} + \mathrm{V} + \mathrm{T}_0 - \mathrm{T}_0 \qquad (\mathrm{I.}\,27)$$

$$= \mathrm{T}_0 + \mathrm{V} + \underbrace{(\mathrm{T} - \mathrm{T}_0)}_{\mathrm{Vc}} \qquad (\mathrm{I.}\,28)$$

$$= \mathrm{T}_0 + \mathrm{V} + V_c + \mathrm{V_H} - \mathrm{V_H} \qquad (\mathrm{I.}\,29)$$

$$= \mathrm{T}_0 + \mathrm{V} + V_c + \underbrace{(\mathrm{V} - \mathrm{V_H})}_{\mathrm{V_x}} \qquad (\mathrm{I.}\,30)$$

$$= \mathrm{T}_0 + \mathrm{V_H} + \underbrace{(\mathrm{V_x} + V_c)}_{V_{xc}} \qquad (\mathrm{I.}\,31)$$

Kohn-Sham's effective potential is given by:

$$\mathrm{V_{eff}} = \mathrm{V_{ext}} + \mathrm{V_H} + \mathrm{V_{XC}} \qquad (\mathrm{I.}\,32)$$

Where

$$\mathrm{V_{XC}} = \frac{\delta \mathrm{E_{xc}}|\rho(\mathrm{r})|}{\delta\rho(\mathrm{r})} \qquad (\mathrm{I.}\,33)$$

is the exchange-correlation interaction.

$$\mathrm{V_H} = \frac{1}{2}\int \frac{e^2}{4\pi\varepsilon_0}\frac{\rho(r')}{|r-r'|}dr' \qquad (\mathrm{I.}\,34)$$

is the Hartree potential of electrons

The Schrödinger equation to be solved under the Kohn and Sham approach is of the form:

$$\left[-\frac{\mathrm{h}^2}{2\mathrm{m_c}}\nabla_{\mathrm{i}}^2 + \mathrm{V_{eff}}(\mathrm{r})\right]|\phi_{\mathrm{i}}(\mathrm{r})\rangle = \varepsilon_{\mathrm{i}}|\phi_{\mathrm{i}}(\mathrm{r})\rangle \quad (\mathrm{i} = 1, \dots, \mathrm{N}) \qquad (\mathrm{I.}\,35)$$

Thus, the total energy of the system will be written as:

$$\mathrm{E}[\rho] = \mathrm{T}_0[\rho] + \mathrm{V_H}[\rho] + \mathrm{V_{xc}}[\rho] + \mathrm{V_{ext}}[\rho] \qquad (\mathrm{I.}\,36)$$

The exchange-correlation energy is defined as the difference between the actual kinetic energy and the kinetic energy of an electron gas in the absence of interactions. It also represents the difference between the actual interaction energy and the Hartree energy, which includes all contributions from multiple bodies. The exchange-correlation potential is defined as the functional derivative.

$$V_{xc} = \frac{\delta V_{xc}[\rho]}{\delta \rho} \qquad (I.37)$$

The exact ground-state density $\rho(\vec{r})$ of an N-electron system is:

$$\rho(\vec{r}) = \sum_{i=1}^{N} \phi_i(\vec{r})^* \phi_i(\vec{r}) \qquad (I.38)$$

Where the single-particle wave functions $\phi_i(\vec{r})$ are the N lowest-energy solutions of the Kohn Sham equation:

$$H_{KS}\phi_i = \epsilon_i \phi_i \qquad (I.39)$$

The Kohn and Sham equations must be solved in a self-consistent manner, which entails initiating the process with an initial density and subsequently determining the density through the use of a set of trial molecular orbitals. The process commences with the acquisition of an effective potential, V_{eff}(r), and the resolution of an equation to determine a novel electron density. Based on this new density, a new effective potential can be calculated. This iterative process continues until convergence is achieved, defined as the point at which the new electron density is equal to or nearly equal to the previous one (according to a fixed convergence criterion).

To solve the Kohn-Sham equations, it is necessary to define the Hartree potential, which, in turn, requires knowledge of the electron density. However, the determination of the electron density is contingent upon the knowledge of the single-electron wave functions, which can only be obtained through the resolution of the Kohn-Sham equations [1]. This problem is commonly approached iteratively, as illustrated in the following figure.

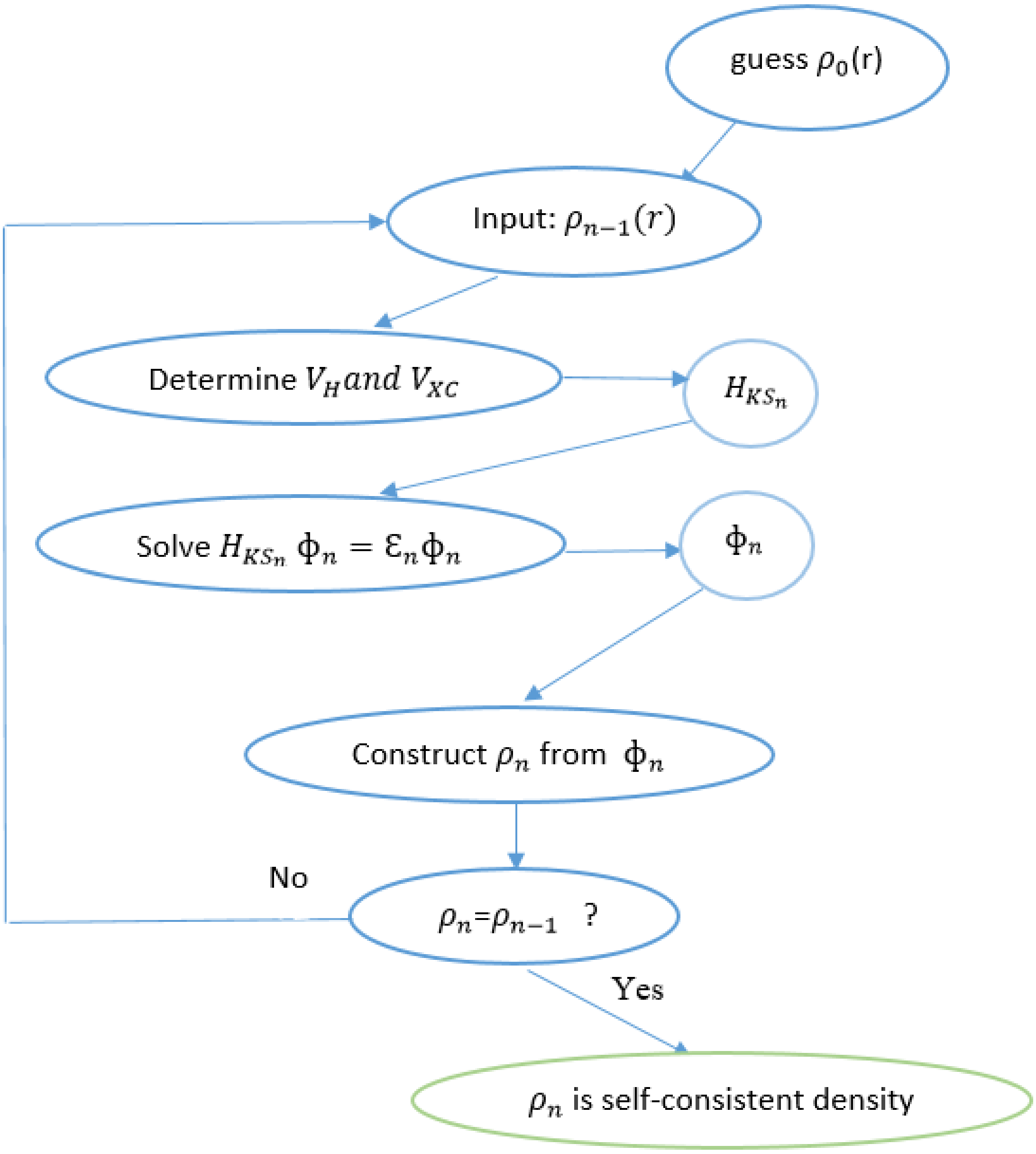

Figure I.1: A flowchart illustrating the steps involved in the nth iteration of the self-consistent procedure used to solve the Hartree-Fock or Kohn-Sham equations.

I.3.3. Exchange-correlation energy approximations

In order to solve the Kohn-Sham equations, it is necessary to define the exchange-correlation functional. However, this functional is only known approximately.

$$E_{xc} = E_c + E_x \qquad (I.40)$$

The exchange energy (E_X) represents the energy associated with the interaction between electrons of identical spin. It arises from the fundamental principle known as the Pauli Exclusion Principle, which dictates that two electrons with the same spin cannot occupy the same spatial location simultaneously. It is important to note that the exchange energy is independent of the electron's charge and is solely determined by the spin properties of the electrons. The exchange energy (E_X) arises due to the antisymmetric nature of the wave function, which ensures that the wave function changes sign when the coordinates of any two electrons are exchanged.

In contrast, E_C arises from the interaction between electrons of opposite spins. However, electrons also experience repulsion due to their shared negative charges. Moreover, electronic correlation leads to a reduced overlap of electron densities, resulting in relatively weak attractive energy. Unfortunately, this intricate n-electron effect was overlooked in the Hartree-Fock method and remains challenging to accurately approximate.

In materials with typical electron densities, the exchange energy dominates over the correlation energy. Yet, at extremely low electron densities, the correlation energy gains significance as the exchange interaction weakens in these sparse electron densities [14].

II.3.3.1. Local Density Approximation (LDA)

Local Density Approximation (LDA) represents an early and widely utilized approximation for the exchange-correlation interaction. The exchange-correlation energy of the system is postulated to be equivalent to that of a uniform electron gas with a density ρ(r). The precise formulation of the exchange-correlation energy for such a uniform electron gas is known.

$$E_{xc}[\rho] = \int \rho(r)\, \varepsilon_{xc}^{hom} \rho(r) dr \qquad (I.41)$$

ε_{xc}^{hom} is the exchange-correlation energy per electron of a homogeneous electron gas of a density ρ(r). The LDA approximation is most applicable to systems exhibiting low spatial variations in electron density. However, it has been demonstrated to be effective across a broader range of materials. Nevertheless, this approach is inadequate for accurately describing the properties of d and f compounds. Notably, the binding energies are consistently overestimated by this approximation [15]. The LDA is based on the local density within a given volume. Consequently, the exchange-correlation energy associated with a specific density $\rho(\vec{r})$ can be calculated by dividing the material into infinitesimal volumes of constant density [2].

II.3.3.2. Generalized Gradient Approximation (GGA)

The LDA approximation simplifies the problem significantly by treating each point in space as if it were part of a homogeneous electron gas with a density equal to that of the actual system at that point. While it is relatively simple and computationally efficient, it may not capture certain non-local effects accurately, leading to limitations in its predictive power for certain systems. While the Generalized Gradient Approximation (GGA) introduces an additional factor to the exchange-correlation contribution, considering the local density within each infinitesimal volume and the densities in neighboring volumes. This means that the density gradient becomes a significant factor. GGA demonstrates slight improvements over LDA, although it has a few drawbacks. However, it offers some flexibility in incorporating the density gradient. In contrast to LDA, which has a single exchange-correlation functional, GGA encompasses multiple versions, including PW86 (Perdew–Wang 1986) [16], PW91 (Perdew–Wang 1991) [17], and PBEsol (Perdew–Burke–Ernzerhof, 1996) is exact for solids under intense compression [18]. In GGA, the non-uniform nature of the electron density is accounted for by replacing ε_{xc}^{hom} with a semi-local function dependent on both the electron density and the magnitude of its gradient.

$$E_{xc}[\rho]=\int f((\rho(r),|\nabla\rho(r)|) \qquad (I.42)$$

where f is an analytical function, it can be parameterized in diverse manners [15].

The generalized gradient approximation (GGA) demonstrates strong performance across diverse systems, typically yielding structural properties with 1% to 3% errors. Addressing overbinding issues inherent in the local density approximation (LDA), GGA tends to increase lattice constants and decrease cohesive energies. Additionally, GGA computations often result in band gaps approximately 50% smaller than LDA, occasionally indicating no band gap. The Generalized Gradient Approximation (GGA) encounters limitations in systems characterized by strongly localized orbitals, an additional repulsive interaction occurs between two electrons on that site that was first recognized by Hubbard (1965). These instances commonly arise in rare-earth elements and their compounds, as well as in transition metal oxides featuring narrow and highly correlated d- and f-orbitals. The DFT is inaccurate in the calculation of the band gap, which is not sur prising as the method is not designed to describe the non-local nature of electron correctly. The band gap underestimation commonly reaches up to 50% when compared with experimental data [14].

I.3.3.3. Tran-Blaha modified Becke-Johnson approach

Two approaches stand out in the realm of theoretical methods for understanding excited states: LDA+U and GW. The applicability of LDA+U is limited to localized electron configurations, notably those of 3d and 4f electrons. On the other hand, GW methods provide unparalleled accuracy but at a significantly higher computational cost [19]. In 2006, Becke and Johnson proposed a new version of the exchange potential, TB-mBJ, and in 2009, a modified Becke-Johnson potential by Tran-Blaha was published. This modification enabled the accurate determination of band gaps for semiconductors and insulators using an orbital-independent exchange-correlation potential that relies solely on semi-local quantities [20]. By utilizing this proposed potential, Calculations of the band structure become computationally affordable and comparable to LDA and GGA methods, thus enabling an efficient application to large systems. This is particularly useful for studying materials like transition metal oxides with strong correlations and rare-earth compounds [21].

II.4. Level 3: Solving the Kohn–Sham equations

The solution of the Kohn-Sham (KS) equations necessitates the observance of three fundamental principles: self-consistency, the variational principle, and constraints. The self-consistency principle is an indispensable aspect of the Density Functional Theory (DFT) methodology, whereby the interconnectedness of KS orbitals, electron densities, and the Hamiltonian are considered throughout the calculation process. The KS orbitals determine the electron densities, which in turn determines the KS Hamiltonian, which determines the new electron densities (as well as the new KS orbitals). It is therefore essential to obtain a set of KS orbitals that yield a KS Hamiltonian whose solutions correspond to the initial KS orbitals. This process, known as self-consistency, ensures meaningful and accurate results.

The choice of the basis of the wave functions to project the Kohn-Sham monoelectronic states which can be taken as a linear combination of orbitals called Kohn-Sham orbitals (KS) written in the following form:

$$\phi_i = \sum_j C_{ij}\,\Phi_j \quad (I.43)$$

Solving in most methods means that we want to find the expansion coefficients C_{ij} needed to express single particle wave function $\phi_i$in a given basis set Φ_j for the occupied orbitals, which minimize the total energy.

The variational principle dictates that the total energy of a system is composed of four distinct terms, each being a functional that depends uniquely on the electron density at the ground state. However, the non-interacting kinetic energy remains an exception. When the density minimizes the variational energy at the ground state, the total energy becomes stationary against small density variations. The general variational principle can be applied to determine the total energy concerning the electron density, KS eigenvalues, or the norm of the residual vector for an eigenstate. However, it is important to observe constraints when seeking the minimum total energy. These constraints include maintaining a fixed total number of electrons or ensuring the orthonormality of orbitals [14].

Constraints play a crucial role when seeking the minimum total energy. Some of the key constraints that must be observed include:

1. **Fixed Total Number of Electrons**: The total number of electrons in the system must remain constant throughout the calculation, which can be represented mathematically as:

$$n = \int \rho(r) dr \qquad (\mathrm{I}.44)$$

2. **Orthonormality of Orbitals**: The orbitals used in the calculation must be orthonormal to each other. Mathematically, this can be expressed as:

$$\int \phi_i^* \phi_j dr = \delta_{ij} \qquad (\mathrm{I}.45)$$

where δij is the Kronecker delta ($0 \ if \ i \neq j, 1 \ if \ i = j$). If the Kronecker delta condition is not met, the density can assume any value, potentially resulting in energy lower than the ground-state energy, which is both unacceptable and unphysical.

To adhere to the principles of quantum mechanics, the Kohn-Sham orbitals undergo enhancements while satisfying the aforementioned constraints. These improvements ensure that the Kohn-Sham orbitals become both antisymmetric and unique, aligning with the fundamental characteristics of the quantum realm [14; 22].

Iterative diagonalization is an approach used to solve the Kohn-Sham equations iteratively. The following is a description of the method:

1. **Initial approximation:**

The electron density of the solid is approximated by combining the electron densities of each atom in its isolated state, as provided by the pseudopotential.

2. **Evaluation of KS System:**

Exchange-correlation potential (V_{XC}) and Hartree potential V_H to evaluate the Kohn-Sham system.

3. **Solution of Coupled KS Equations:**

A set of coupled Kohn-Sham equations is solved, yielding a set of Kohn-Sham orbitals as solutions (to determine the wave function of a single particleϕ_i)

4. **Calculation of new Electron Density:**

Utilizing the new Kohn-Sham orbitals $\phi_i(r)$, the new electron density $\rho(r)$ is calculated, incorporating a mixture of the previous and current densities.

5. **Iterative Refinement and Convergence Check:**

If the difference is within a pre-defined tolerance, the SCF cycle has converged, and you have found the self-consistent electron density and effective potential. If not, mix the new and old densities to form a better guess and return to step two. The iteration process continues until the energy change (or density change) of the system becomes smaller than a predefined stopping criterion, typically in the range of 10^{-4} to 10^{-5} eV.

Upon satisfaction of the pre-specified convergence criterion, self-consistency is established, and the resulting energy estimate is deemed to represent the system ground-state energy, as defined by the electron density at that state.

References

[1] D. S. Sholl, J. A. Steckel. John Wiley and Sons, *Density functional theory A Practical Introduction*, ISBN 978 0470 373170, 2009

[2] S. Cottenier, *Density Functional Theory and the Family of (L) APW-methods: a step-by-step introduction,* Ghent University, Belgium, 2013.

[3] M. K. Harbola, A. Banerjee, *Many-Electric problem in terms of the density: From Thomas Fermi to Modern Density-functional Theory*. J. Theoretical and Computational Chemistry, Vol. 2, No. 2, pp. 301–322, 2003

[4] J. D. Patterson, B.C. Bailey, *Solid-State Physics*, J. Springer, Berlin, 2007.

[5] V. Fock, *Approximation method for solving the quantum mechanicalmultibody problem. (naherungsmethode zur LSsung des quantenmechanischen Mehrkorperproblems)*, 1930

[6] J. C. Slater, *a Simplification of the Hartree Fock, J.* Physical Review, Vol. 81, No. 3, 1951

[7] L. H. Thomas, *The calculation of atomic fields,* In Mathematical Proceedings of the Cambridge Philosophical Society, Vol. 23, No. 05, pp. 542-548, 1927

[8] E. Fermi, *Eine statistische Methode zur Bestimmung einiger Eigenschaften des Atoms und ihre Anwendung auf die Theorie des periodischen Systems der Elemente, J.* Z. Phys., Vol. 48, No. 1-2, pp. 73-79, 1928.

[9] P. Hohenberg and W. Kohn, *Inhomogeneous electron gas*, Phys. Rev, Vol. 136, No. 3B, pp. B864, 1964

[10] D. J. SINGH, *Plane waves, Pseudopotentials and the LAPW method, Second Edition*, Uppsala University, Sweden ISBN 10: 0-387-29684, 2006

[11] J. Kohanoff, *Electronic Structure Calculations for Solids and Molecules Theory and Computational Methods* (Cambridge University Press UK, 2006).

[12] R. M. Martin, *Electronic structure Basic theory and practical methods*, university press Cambridge, ISBN 0 521 782856, 2004

[13] W. Kohn and L. J. Sham, *Self-Consistent Equations Including Exchange and Correlation Effects*, Phys. Rev. Vol. 140, pp. 1133-1138, 1965

[14] J. G. Lee, *Computational Materials Science An Introduction Second Edition*, Taylor & Francis Group, ISBN 9781498749732, 2017

[15] M. Freyss, *Density functional theory*. Centre de Cadarache, France, NEA/NSC/R5, 2015

[16] J. P. Perdew, Y. Wang, *Accurate and simple density functional for the electronic exchange energy: Generalized gradient approximation*, Phys. Rev. B, Vol 33, No 12, pp. 8800-8802, 1986

[17] J. P. Perdew, J. A. Chevary, S. H. Vosko, K. A. Jackson, M. R. Pederson, D. J. Singh, C. Fiolhais, *Atoms, molecules, solids, and surfaces: Applications of the generalized gradient approximation for exchange and correlation*, Phys. Rev. B, Vol. 46, pp. 6671-6687, 1992

[18] J. P. Perdew, K. Burke, M. Ernzerhof, *Generalized Gradient Approximation Made Simple,* Phys. Rev. Lett., Vol 77, pp. 3865, 1996

[19] A. D. Becke and E. R. Johnson, *A simple effective potential for exchange*, J. Chem. Phys., Vol. 124, No. 22, pp. 221101(4), 2006

[20] F. Tran, P. Blaha, and K. Schwarz, *Band gap calculations with Becke-Johnson exchange potential*, J. Phys.: Condens. Matter, Vol. 19, No 19, pp. 196208(8), 2007

[21] F. Tran and P. Blaha, *Accurate Band Gaps of Semiconductors and Insulators with a Semi-local Exchange-Correlation Potential*, Phys. Rev. Lett., Vol. 102, No. 22, pp. 226401(4), 2009

[22]G. Kresse, J. Furthmuller, *Efficient iterative schemes for ab initio total-energy calculations using a plane-wave basis set*, Phys. Rev. B, Vol. 54, No. 16, pp. 11169(18), 1996

Chapter II

Pseudo Potential Plane Wave and Full-Potential Linearized Augmented Plane-Wave

Chapter II

II.1. Pseudopotential Plane-Wave method (in brief)

In the study of condensed matter systems and the solution of the Schrödinger equation, atomic space can be divided into two distinct regions with different properties. The first region, situated in close proximity to the nuclei, is predominantly comprised of tightly bound core electrons. The core electrons exhibit minimal response to neighboring atoms and exert a negligible influence on the chemical bonding between atoms. Consequently, they can be considered essentially fixed in their positions. Conversely, the remaining volume encompasses the valence electron density, which actively participates in the bonding of atoms. This distinction between core and valence electrons is known as the frozen core approximation [1]. This approximation posits that the configuration of core electrons within a solid is equivalent to that of isolated atoms. Consequently, the treatment of core electrons is resolved at the atomic level, and the focus shifts to investigating the behavior and motion of valence electrons within the ionic potential, as initially suggested by Fermi in 1934 [2] and subsequently developed by Hellmann in 1935 [3].

The Bloch theorem represents a foundational concept in the field of solid-state physics, wherein it describes the behavior of electrons within a periodic crystal lattice. The theorem states that the electronic wave functions in a crystal can be expressed as a product of a periodic function and a plane wave. Consequently, each electronic wave function can be represented as a summation of plane waves. The plane wave basis set is employed to expand the electronic wave functions in reciprocal space. Plane waves are a mathematically simple basis set that can accurately describe periodic functions. The use of periodic boundary conditions, which assume the system repeats itself indefinitely in space, effectively treats the interactions between atoms in the finite system as if the system were part of an infinite, periodic crystal lattice. This simplifies the calculations and allows for the use of efficient algorithms based on the fast Fourier transform (FFT) to solve the Kohn-Sham equations in reciprocal space. In order to ensure that the interactions between neighboring unit cells do not affect the properties of the finite system, the size of the unit cell is chosen to be sufficiently large so that the interactions between the periodic replicas of the system are negligible. This implies that the unit cell should be sufficiently large to prevent significant overlap or coupling between the periodic replicas.

The finite system is placed in a unit cell of a fictitious crystal, and this cell is made sufficiently large to avoid interactions between neighboring cells. Subsequently, the Kohn-Sham equations can be solved for any system in momentum space. However, for finite systems, a very large number of plane waves is required, as the electronic density is concentrated on a small fraction of the total volume of the supercell. The valence wave functions of the large Z atoms exhibit strong oscillations in proximity to the atomic core, a consequence of the orthogonalization of the inner electronic wave functions. The description of these oscillations necessitates the use of a considerable number of plane waves, which can present a challenge in the calculation of the total energy.

The Kohn-Sham equations can be solved in momentum space, allowing for the examination of any system. However, due to the concentration of electronic density in a small portion of the supercell's total volume, a large number of plane waves is required for finite systems. It is noteworthy that the valence wave functions of atoms with a high atomic number (Z) exhibit significant oscillations near the atomic core as a consequence of orthogonalizing the inner electronic wave functions. However, the inner electrons are largely inactive and do not significantly contribute to the formation of chemical bonds. This indicates that an atom can be described based on its valence electrons, which experience an effective potential that includes both the nuclear attraction and the repulsion of the inner electrons.

The Pseudopotential Plane-Wave (PP-PW) method employs two primary elements: pseudopotentials and plane waves. The pseudopotential approximation is utilized to substitute the strong ionic potential with a weaker pseudopotential. This approximation simplifies the interaction between valence electrons and atomic nuclei. Instead of the true valence wave functions, the pseudopotential acts on a set of pseudo wave functions. In this approach, the external potential, denoted as Vext, is obtained by summing the pseudopotentials of all atoms within the system [4].

III.2. The APW method

The augmented plane wave (APW) method was initially proposed by Slater in 1937 [5], but it did not become widely utilized until 1964 [6]. Although the APW method itself is no longer widely used, it provided a foundational concept for modern computational techniques. The underlying concept of the APW method was derived from pseudopotential methods, with the objective of providing a more accurate description of wave functions in the atomic core regions.

The APW method is constructed by augmenting plane waves with additional basis functions that are localized around the atomic sites. These localized basis functions are capable of capturing the short-range behavior of the wave functions near the atomic cores, thereby allowing for a more accurate representation of the electronic structure in these regions.

In order to address the issue of electron motion in a periodic potential, Slater proposed a solution that involved dividing the crystal into non-overlapping atomic spheres surrounding each atom. Within each atomic sphere, the wave function is expanded using a basis set that includes both plane waves and augmented plane waves. Outside the atomic spheres, the wavefunction is expanded solely in terms of plane waves (Fig II.1). The following is an illustration of Slater's method in action:

- Inside spheres (region I): The potential is spherically symmetrical. The wave function is expanded using a combination of spherical harmonics and radial solutions. Around each atom, a sphere with radius R_α is drawn (referred to as S_α, or a "muffin tin sphere").
- Outside spheres (region II): The potential is constant, and a single plane wave is used to solve Schrödinger's equation [6,7].

A single augmented plane wave (APW) employed in the expansion of $\varphi_{\vec{K}}^{\vec{k}}(\vec{r})$ is defined as follows:

$$\varphi(r) = \begin{cases} \sum_{l,m} A_{lm}^{\alpha,\vec{k}+\vec{K}}\, \mu_l^\alpha(r', E) Y_m^l(\widehat{r'}) & \vec{r} \in \mathrm{I} \\ \frac{1}{\sqrt{V}} e^{\vec{i}(\vec{k}+\vec{K}).\vec{r}} & \vec{r} \in \mathrm{II} \end{cases} \qquad \text{(II.1)}$$

Where $\vec{k}$ is the Bloch vector (APW basis set is k-dependent), V is the cell volume, $\vec{K}$ is a reciprocal lattice vector, and $r = \acute{r} - r_\alpha$ is the position inside the spheres, relative to the center of each sphere. The $Y_{\ell m}$ are spherical harmonics. The $A_{lm}^{\alpha,\vec{k}+\vec{K}}$ are yet undetermined parameters. The $\mu_l^\alpha(r', E)$ are solutions to the radial part of the Schrödinger equation for a free atom α:

$$\left[-\frac{d^2}{dr^2} + \frac{l(l+1)}{r^2} + V^\alpha(r) - E_l\right] r\mu_l^\alpha(r, E) = 0 \qquad \text{(II.2)}$$

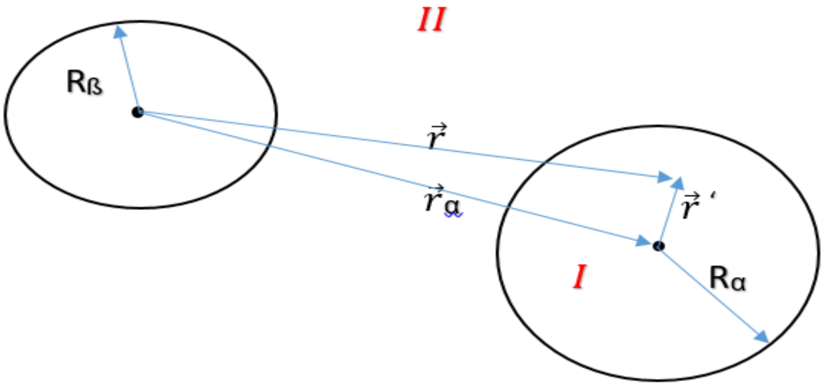

Figure II.1: The partitioning of a unit cell into muffin-tin regions and an interstitial region in the case of a system with two atoms non-overlap.

For a free atom at energy E, the boundary condition requires that $\mu_l^\alpha(r, E)$ vanishes as r tends to infinity, limiting the number of energies for which a solution $u_{\alpha\ell}$ can be obtained for a true free atom. However, as this boundary condition does not apply in this context, a numerical solution can be found for any EE. Consequently, it is possible to identify values of the energy E_l for which $\mu_l^\alpha(r', E)$) vanishes at the sphere's limit, resulting in a separation of the plane waves with respect to the radial functions. This issue is known as the asymptote problem.

As the bands approach the asymptote, the calculations become more complex. To address this problem, several modifications to the APW method have been proposed. One notable method, proposed by Andersen [8], ensures that both the basis functions and their derivatives are made continuous by matching them to a radial function μ_l^α at a fixed E_l, along with their derivatives $\dot{\mu}_l^\alpha$, with respect to the energy E_l. This modification effectively resolved the issues with the APW method, providing a more flexible and accurate method for calculating the band structure. This improvement led to the development of the LAPW method.

III.3. The Full Potential-Linearized Augmented Plane Wave (FP-LAPW) method

The Full Potential-Linearized Augmented Plane Wave (FP-LAPW) method was developed to address the computational challenges that were encountered when employing the standard augmented plane wave (APW) method. Two primary difficulties have been identified [9]:

1. Energy dependence: The Schrödinger equation exhibits energy dependence due to the nonlinearity of the energy parameter used for the radial solutions within the muffin-tin

   spheres. Here, the Schrödinger equation is solved exactly within each atomic sphere, which presents a significant computational challenge. In order to overcome this challenge, techniques such as the determination of determinants or more advanced methods for varying the energy parameter have been employed.

2. The secular equation exhibits singular behavior. Another challenge arises from the singular behavior of the secular equation, particularly when a radial solution node coincides with the muffin-tin-sphere boundary, a situation commonly referred to as the asymptotes.

In the full-potential method (FP-LAPW) [12,13], the basic functions inside the spheres are linear combinations of radial functions, $\mu_l^{\alpha}(r',E)Y_m^l(\widehat{r'})$ and their derivatives as a function of energy $\dot{\mu}_l^{\alpha}(r',E)Y_m^l(\widehat{r'})$ with respect to the linearization parameters, E_l. The μ_l are defined exactly as in the APW method (Eq II.2), with a fixed E_l. The energy derivative, $\dot{\mu}_l(r)Y_m^l(\hat{r})$ satisfies [10], which linearizes the Schrödinger equation within each atomic sphere, thereby simplifying the calculation and improving efficiency.

$$\left[-\frac{d^2}{dr^2}+\frac{l(l+1)}{r^2}+V(r)-E_l\right]r\dot{\mu}_l(r)=r\mu_l(r) \qquad (II.3)$$

The aforementioned functions are calibrated to align with the values and derivatives of the plane waves at the boundaries of the spheres. The resulting augmented plane waves serve as the basis for the LAPWs (Linearized Augmented Plane Waves), which are commonly referred to as such. The wave functions can be expressed in terms of this basis as follows:

$$\varphi(r)=\begin{cases}\sum_{lm}[A_{lm}\,\mu_l(r)+B_{lm}\dot{\mu}(r)Y_{lm}(\hat{r}) & r\in I\\ \frac{1}{\sqrt{V}}e^{\vec{i}(\vec{k}+\vec{K}).\vec{r}} & \vec{r}\in II\end{cases} \qquad (II.4)$$

Where B_{lm} is the coefficient corresponding to the function μ_l and is of the same nature as the coefficients A_{lm}.

In the LAPW method plane waves are used in the interstitial region, as in the APW method. Inside the spheres, the LAPWs offer greater variational freedom compared to APWs; the plane waves are used linearized augmented.

$$u_l\,(\epsilon,r)=u_l\,(E_l,r)+(\epsilon\text{-}E_l)\dot{u}_l(\epsilon,r)+O((\epsilon-E_l)^2) \qquad (II.5)$$

This is because, if E_l differs slightly from the band energy,ϵ, a linear combination, will reproduce the APW radial function constructed at the band energy (Going to the LAPW method introduces quadratic errors of order $(\epsilon-E_l)^2$in the wave function). Despite these minor limitations, the LAPW functions serve as a reliable basis for obtaining all the valence bands within a relatively broad energy range using a single E_l. However, it is also feasible to divide the energy interval into multiple energy windows, where each window corresponds to a specific energy E_l for which the solutions are obtained separately [11]. The final definition of an LAPW is then:

$$\varphi_{\vec{K}}^{\vec{k}}((\vec{r}) = \begin{cases} \sum_{lm} \left[A_{lm}^{\alpha,\vec{k}+\vec{K}} \mu_l^{\alpha}(r', E_{1,l}^{\alpha}) + B_{lm}^{\alpha,\vec{k}+\vec{K}} \dot{\mu}_l^{\alpha}(r', E_{1,l}^{\alpha}) Y_m^l(\hat{r}') \right. & \vec{r} \in I \\ \frac{1}{\sqrt{V}} e^{\vec{\imath}(\vec{k}+\vec{K}).\vec{r}} & \vec{r} \in II \end{cases} \quad \text{(II.6)}$$

Once the $E_{1,l}^{\alpha}$ values have been fixed, the basis functions can be computed definitively. Subsequently, the same procedure utilized for the plane wave basis set can be employed in the calculations [7].

In the LAPW method, a single diagonalization is sufficient to obtain accurate energy bands at a specific k-point. In contrast, the APW method necessitates a distinct diagonalization for each band [10].

III.3.1. LAPW with Local Orbitals (LAPW+LO)

The electronic states of matter are classified into three categories: core states, semi-core states (which lie between valence and core states), and valence states. In the LAPW+LO method, the electronic structure of materials is determined by treating the valence and core states differently. The valence states are expanded using LAPW basis functions, which allows for the accurate description of their extended nature by utilizing the crystal potential. Conversely, the core states are addressed using a numerical basis within an atomic approximation. This approximation constrains the core wave functions to be spherical and neglects any off-site overlaps. The core states are computed using an atomic code, where the spherical part of the crystal potential replaces the atomic potential within the atomic sphere. Consequently, both the core and valence states are calculated in a self-consistent manner. The core states are treated in a fully relativistic manner within the context of the spherical approximation, whereas the valence states utilize the full crystal potential, accounting for their extended character.

The LAPW method necessitates the use of non-overlapping spheres, which consequently renders the augmenting functions, u_l and u'_l, orthogonal (due to diagonalization) to any core state that is strictly confined within the MT sphere. However, for elements with diverse electronic configurations, there are extended core states that are not sufficiently close to zero on the sphere boundary to have u_l and u'_l orthogonal to them. It has been observed in numerous elements, including alkali metals, rare earths, actinides, and early transition metals [12, 13], as well as in 4f and 5f materials [14, 15], that high-lying and extended core states (e.g., the 5p state in the 4f elements) exist. These states are also referred to as semi-core states. Semi-core states possess a higher energy than core states but a lower energy than valence states.

As an illustrative example, consider the hybridization of the 3p core state in bcc copper. This state extends beyond the MT sphere, with a fraction of the charge outside the atomic sphere. This is because the 3*p* states are too high in energy (4.3 Ry below the Fermi level) to be confined within this sphere. In contrast, the 4*p* states in the valence region are approximately 0.2 Ry below the Fermi level. This issue may be mitigated by treating the 3p and 4p states in the valence region, although this approach may lack flexibility. An alternative approach would be to expand the muffin-tin sphere. However, when a compound is studied as a function of pressure or when atoms are moved from equilibrium positions to study lattice vibrations, the small bond distances do not allow the muffin-tin ball to expand sufficiently.

In 1991, Singh [16] solved this dilemma by adding another type of basis function to the LAPW basis set, called a local orbital (LO). A local orbital is defined for a particular ℓ and m, and for a particular atom α. It is local in the sense that it is completely confined within the MT. It is defined as:

$$\phi^{lm}_{\alpha,LO}=\begin{cases}\left(A^{\alpha,LO}_{lm}\,u^{\alpha}_{l}\left(r',E^{\alpha}_{1,l}\right)+B^{\alpha,LO}_{lm}\dot{u}^{\alpha}_{l}\left(r',E^{\alpha}_{1,l}\right)+C^{\alpha,LO}_{lm}u^{\alpha}_{l}\left(r',E^{\alpha}_{2,l}\right)\right)Y^{l}_{m}(\hat{r}') & \vec{r}\in I\\ 0 & \vec{r}\in II\end{cases} \tag{II.7}$$

Where $u^{\alpha}_{l}\left(r',E^{\alpha}_{1,l}\right)$ and $\dot{u}^{\alpha}_{l}\left(r',E^{\alpha}_{1,l}\right)$ as in the LAPW basis set are used, with as linearization energy$E^{\alpha}_{1,l}$, ℓ a value suitable for the highest of the two valence states (4p in our example). The three coefficients$A^{\alpha,LO}_{lm}$, $B^{\alpha,LO}_{lm}$ and $C^{\alpha,LO}_{lm}$ are determined by requiring that the LO is normalized and has zero value and zero slopes at the muffin tin boundary. This ensures that the wave function does not leak out of the muffin tin sphere.

The lower valence state, which is more free-atom-like, is sharply peaked at an energy $E^{\alpha}_{2,l}$. A single radial function, $u^{\alpha}_{l}\left(r',E^{\alpha}_{2,l}\right)$, at that same energy will be sufficient to describe it. Local orbitals are not connected to plane waves in the interstitial region; consequently, they lack k and K dependence. The size of the LAPW base set increases when local orbitals are added, resulting in a slight increase in computational time. However, this is offset by the high accuracy offered by local orbitals.

II.3.2. The APW+lo method

Local orbitals were initially introduced in the LAPW method by Singh to treat semi-core states [17]. An energy-independent APW basis set is insufficient for identifying solutions in a region around a fixed energy parameter. This dependence has been eliminated in the LAPW+LO method, however, this has come at the cost of a larger basis size. Sjöstedt, Nordström, and Singh have recently made an additional improvement by introducing a basis that combines the advantages of the APW method and those of the LAPW method. This method is designated as "APW+lo" and corresponds to an energy-independent basis set (analogous to the LAPW+LO method), which has been demonstrated to be highly efficacious in reducing the basis set sizes. The variational freedom can be enhanced by employing a complementary basis set comprising local orbitals for physically significant L-quantum numbers. The local orbitals impose no additional constraints on the APW basis set, thus maintaining the number of plane waves in the interstitial region. The definition of these functions is as follows:

$$\varphi_{\alpha,lo}^{lm}((\vec{r}) = \begin{cases} \sum_{lm}\left[A_{lm}^{\alpha,lo}\,\mu_l^{\alpha}\left(r',E_{1,l}^{\alpha}\right) + B_{lm}^{\alpha,lo}\,\dot{\mu}_l^{\alpha}\left(r',E_{1,l}^{\alpha}\right)Y_m^l(\hat{r}') & \vec{r} \in I \\ 0 & \vec{r} \in II \end{cases} \qquad \text{(II.8)}$$

$\varphi_{\alpha,lo}^{lm}$ and $B_{lm}^{\alpha,lo}$ are determined by normalization, and by requiring that the local orbital has zero value at the muffin tin boundary. The APW and the local orbital are continuous at the sphere boundary, but for both their first derivative is discontinuous [13].

References

[1] W.E. Pickett, *Pseudopotential Methods in Condensed Matter Applications,* Comp. Phys. Rep. 9, pp. 115, 1989.

[2] E. Fermi, *Above the Pressure Displacement of the High Lines of the Spectral Series*, Il Nuovo Cimento, Vol. 11, pp. 157, 1934.

[3]H. Hellmann, *A New Approximation Method in the Problem of Many Electrons*, J. Chem. Phys. 3, 61, 1935.

[4]C. Fiolhais, F. Nogueira and M. Marques, *A Primer in Density Functional Theory*, Springer, Berlin, 2003.

[5] J. C. Slater, *Wave Functions in a Periodic Potential*, Phys. Rev. 51, pp. 846-851, 1937.

[6] J. C. Slater, *Energy Band Calculations by the Augmented Plane Wave Method*, Advances in Quantum Chemistry 1, pp. 35-58, 1964.

[7] S. Cottenier, *Density Functional Theory and the Family of (L)APW-methods: a step by step introduction*, Ghent University, Belgium, 2013.

[8] O. K. Andersen, *Linear methods in band theory*, Phys. Rev. B 12, pp. 3060-3083, 1975.

[9] D. D. Koelling and G. O. Arbman, *Use of energy derivative of the radial solution in an augmented plane wave method: application to copper*, J. Phys. F (Metal Phys.) 5, pp. 2041-2054, 1975.

[10] D. J. Singh, L. Nordstrom, *plane waves, pseudopotentials and the LAPW method,2nd Edition*, U.S.A, 2006.

[11] L. F Mattheiss and D. R. Hamann, *Linear augmented-plane-wave calculation of the structural properties of bulk Cr, Mo, and W*, Phys. Rev. B, Vol. 33, No. 2, pp. 823-840, 1986.

[12] P. Blaha, D. J. Singh, P. I. Sorantin and K. Schwarz, *Electric-field-gradient calculations for systems with large extended-core-state contributions*, Phys. Rev. B 46, pp. 1321-1325, 1992.

[13] D. J. Singh, K. Schwarz and P. Blaha, *Electric-field gradients in* $YBa_2Cu_3O_7$*: Discrepancy between experimental and local-density-approximation charge distributions*, Phys. Rev. B 46, pp. 5849-5852, 1992.

[14] D. J. Singh, *Adequacy of the local-spin-density approximation for Gd*, Phys. Rev. B 44, pp. 7451-7454, 1991.

[15] S. Goedecker and K. Maschke, *Alternative approach to separable first-principles pseudopotentials*, Phys. Rev. B 42, pp. 8858-8863, 1990.

[16] D. Singh, *Ground-state properties of lanthanum: Treatment of extended-core states*, Phys. Rev. B 43, pp. 6388-6392, 1991.

Chapter III

Results and Discussion

Chapter III

III.1. Computational Details

Two complementary codes based on the density functional theory were employed for a complete investigation of the structural parameters, elastic moduli, electronic properties and optical spectra of quaternary chalcogenide compounds $Tl_2CdGeSe_4$ and $Tl_2CdSnSe_4$.

The first part of the present work, namely, the structural optimization and elastic constants, were performed using an efficient method to relax the crystal structure, namely the pseudopotential plane wave (PP-PW) approach based on density functional theory (DFT) as incorporated in the Cambridge Sequential Total Energy Package (CASTEP) [1]. The exchange–correlation interactions were modeled using the PBEsol form of the general gradient approximation (labeled GGA-PBEsol or GGA-08) [2], which was specially developed to better predict the optimized crystal structures of solids. Norm-conserving pseudopotentials [3, 4] were used to describe the Coulombic interactions between the valence electrons and ion cores. The electron states Tl: $5d^{10}6s^2$ $6p^1$, Cd: $4s^24p^64d^{10}5s^2$, Sn: $4d^{10}5s^25p^2$, Ge: $3d^{10}4s^24p^2$ and Se: $3d^{10}4s^24p^4$ were treated as the valence states. The Kohn–Sham electronic wave functions were developed on a plane wave basis set truncated at an energy cutoff of 1350 eV. Integrations over the Brillouin zone (BZ) were performed over a 7 × 7 × 6 special Monkhorst–Pack k-mesh [5]. The Broyden–Fletcher–Goldfarb–Shanno (BFGS) technique [6] was employed to relax the free structural parameters. The Se internal coordinates, x_{Se}, y_{Se}, z_{Se}, and the lattice parameters, a and c, with convergence cutoffs of 5.0×10^{-6}eV/atom, 0.01 eV/Å, 0.02GPa and 5.0×10^{-4}Å for the total energy, maximum ionic Hellmann–Feynman force, maximum ionic displacement and maximum stress, respectively. The well-known stress–strain technique [1] was used to calculate the monocrystalline elastic constants C_{ij}. In this approach, C_{ij} is estimated by computing the stress tensors $\leftrightarrow$ σ generated by applying different small deformation tensors $\leftrightarrow$ δ to the equilibrium lattice, and then C_{ij} is determined by a linear fit of the computed stress–strain curves. Two deformations, where the first is defined by a strain tensor $\leftrightarrow$ δ with only two nonzero components, viz., δ_{xx} and δ_{yz}, and the second with also only two non-zero components, viz.,δ_{zz} and δ_{xy}, are sufficient to determine the six independent elastic constants, namely, C_{11}, C_{33}, C_{44}, C_{66}, C_{12} and C_{13}, of a tetragonal system. The phonon-dispersion curves were calculated through a linear-response method based on density functional perturbation theory.

The second part of the present work, namely, the electronic and optical properties were carried out through the full-potential (linearized) augmented plane wave plus local orbitals (FP-L/APW + lo) as implemented in the WIEN2k code [7]. The FP-(L)APW + lo method is one of the most accurate approaches for calculating electronic structure and the associated properties. It is well established that the energy bandgap calculated through common exchange–correlation (XC) functionals, namely the local density approximation (LDA) and the generalized gradient approximation (GGA), are generally significantly smaller than that from experimental data. Thus, some XC functionals beyond the standard LDA and GGA, such as hybrid functionals, the GW method, and the Tran-Blaha-modified Becke-Johnson (TB-mBJ) potential, have been developed to overcome this deficiency. To remedy the systematic underestimation of the bandgap by the GGA, we used the TB-mBJ potential [8, 9], which has been shown to predict bandgaps that are in good agreement with experimental counterparts and with theoretical results obtained using more advanced calculations, such as those based on Green's function (GW) and hybrid functionals, for a wide variety of semiconductors and insulation [10–11]. Note that the computation cost when using the TB-mBJ potential is significantly lower than that when using the hybrid functionals and GW approximation [12]; the computation time using the TB-mBJ potential is comparable to that using the standard LDA and GGA. Therefore, TB-mBJ was chosen to correct the bandgaps of the studied Tl-based selenides. The valence wave functions inside the interstitial region were developed on a plane wave basis set, with the largest k vector (K_{max}) equal to $9/R_{MT}^{min}$, where R_{MT}^{min} is the smallest muffin-tin radius in the Bohr unit. The valence wave functions inside the muffin-tin spheres were developed on spherical harmonics up to $l_{max} = 10$. The muffin-tin sphere radius was chosen to equal 2.5 Bohr for Tl, 2.46 Bohr for Cd, 2.14 Bohr for Ge, 2.35 Bohr for Sn, and 2.14 Bohr for Se. The total energy convergence was set to 10^{-5} Ry, and the atom relaxation was determined with a force on each atom less than 0.1 eV/Å. The optical properties of a material affect the characteristics of electromagnetic waves passing through it by modulating their propagation vector (dispersion) or intensity (absorption). The linear macroscopic response of a solid medium to incident electromagnetic waves is modeled by the optical complex dielectric function $\varepsilon(\omega) = \varepsilon_1(\omega) + \varepsilon_2(\omega)$, where $\varepsilon_1(\omega)$ (the real part) models the dispersion of electromagnetic radiation and $\varepsilon_2(\omega)$ (the imaginary part) models the dissipation of the energy of electromagnetic radiation inside the crossed medium. Theoretically, the $\varepsilon_2(\omega)$ spectrum is calculated by summing all the individual contributions of the allowed direct electronic transitions between the pairs of electronic states (V_n, k) and ($C_{n'}$, k), where (V_n, k) is an occupied electronic state in a valence band of index n and ($C_{n'}$, k) is an unoccupied electronic state in a conduction band of index n'. The spectrum of the dispersive part of the dielectric function, $\varepsilon_1(\omega)$, is then computed from the $\varepsilon_2(\omega)$ spectrum through the Kramers–Kronig transformation. The spectra of the other macroscopic linear optical functions, namely, the refractive index n(ω), extinction coefficient k(ω), optical reflectivity R(ω), absorption coefficient α(ω) and energy-loss function L(ω), can be computed from the $\varepsilon_1(\omega)$ and $\varepsilon_2(\omega)$ spectra. All the reported spectra of macroscopic linear optical functions in this work were calculated using the random phase approximation formulation developed by Ambrosch–Draxl and Sofo [13] and implemented in the WIEN2k code. A large grid of 40×40×40 k-points was used to calculate the electronic properties and optical spectra, as they are very sensitive to the k-mesh. Due to the presence of heavy atoms in the studied compounds, all the performed calculations were carried out both with and without spin–orbit coupling, which we refer to hereafter as + SOC and NSOC, respectively.

III.2. Results and Discussion

III.2.1. Structural properties of the Tl_2CdXSe_4 (X= Ge, Sn) compounds

III.2.1.1 Structural description

The quaternary chalcogenide compounds $Tl_2CdGeSe_4$ and $Tl_2CdSnSe_4$ crystallize in the tetragonal system with the non-centrosymmetric space group I-42 m (No. 121), as determined through X-ray diffraction analysis [14; 15; 16]. The location and coordination of the surrounding atoms constituting the unit cell structure of $Tl_2CdGeSe_4$, as a representative, are depicted in Fig. III.1 The Cd and Ge atoms, which are bonded to four Se atoms forming slightly distorted tetrahedral (see the polyhedral diagrams in Fig. III.1b, c), occupy Wyckoff sites 2b (0, 0, 0.5) and 2a (0, 0, 0), respectively. The Tl atom, which is coordinated by eight Se atoms forming a distorted tetragonal antiprism (Fig III.1d), is located at Wyckoff site 4c (0, 0.5, 0). The Se atom, which is surrounded by 1Cd, 1Ge and 4Tl cations forming a trigonal prism, occupies Wyckoff site 8i(x_{Se}, x_{Se}, z_{Se}), wherex_{Se}, x_{Se} and z_{Se} are the internal coordinates of the Se atom. Thus, the crystal structure of the studied compounds has four free structural parameters not fixed by the space group, namely the following: the cell parameters, a and c, and the internal coordinate, x_{Se} and z_{Se}, which have to be relaxed to reach the equilibrium crystal structure.

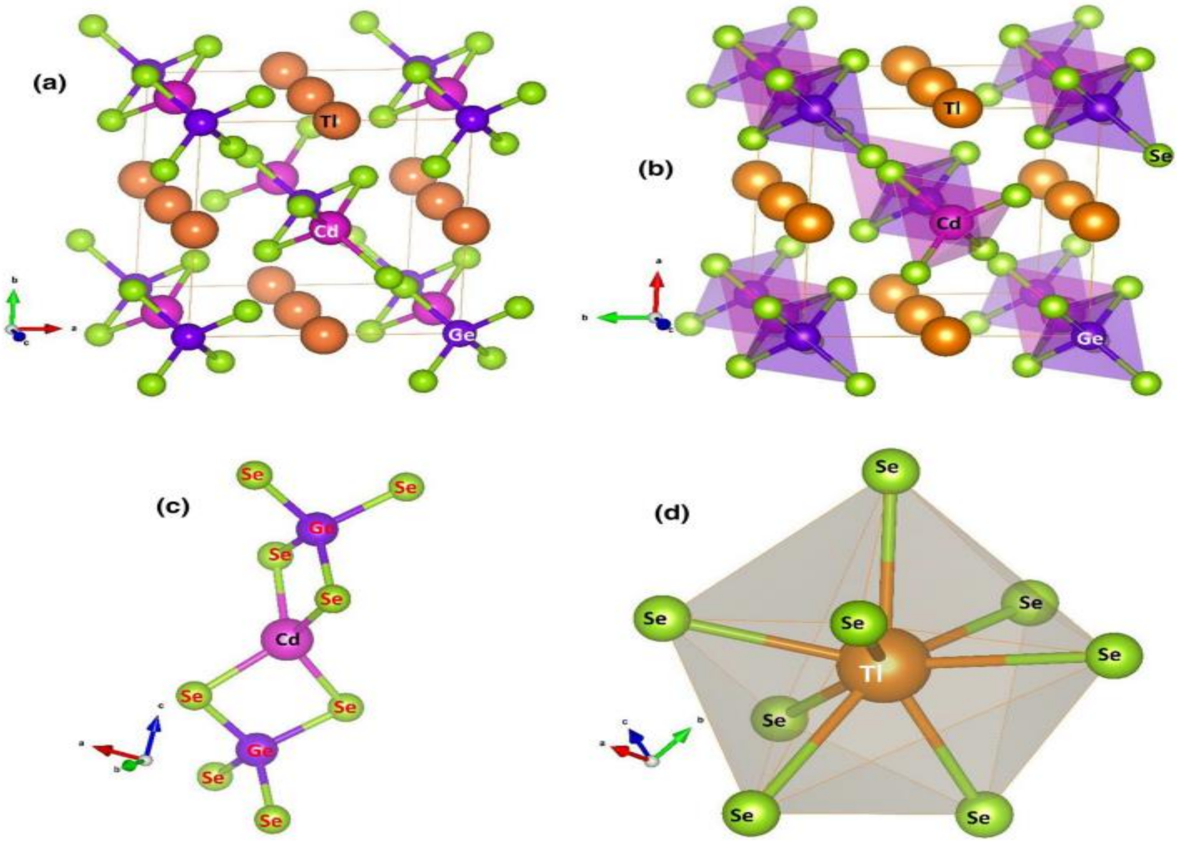

Figure III.1: (a) Depiction of the unit cell structure of $Tl_2CdGeSe_4$. **(b)** Polyhedral representation showing the arrangement of Cd and Ge atoms within the unit cell. **(c)** The closest neighboring Se atoms surround the Cd and Ge atoms, forming $CdSe_4$ and $GeSe_4$ tetrahedra. **(d)** The closest neighboring Se atoms surround the Tl atoms within the unit cell

III.2.1.2. Equilibrium structural properties

The equilibrium structural parameters of the studied compounds, viz., the lattice parameters, a and c, the internal coordinates of the Se atom and the distances between the nearest neighbors, computed both with and without spin–orbit coupling (labeled + SOC and NSOC, respectively), are presented in Tab. III.1 and III.2 along with the available corresponding measured values [14; 15; 16]. Our calculated values for the lattice parameters and the corresponding experimental data [17; 15; 16] demonstrate excellent agreement; the maximum relative discrepancy does not exceed − 0.8% when spin–orbit coupling is included $(d(\%) = ((x - x_{expt})/x_{expt} * 100)$. The calculated relaxed fractional internal coordinates of the Se atom and bond lengths are also consistent with the available corresponding experimental data.

Table III.1: Calculated equilibrium lattice parameters (a and c, in Å), unit cell volume (V, in Å^3), relative deviation of the computed values from the corresponding experimental data (d %), and relaxed fractional internal coordinates of the Se atom (x/a, y/a z/c) for the $Tl_2CdGeSe_4$ and $Tl_2CdSnSe_4$ compounds. Available results in the literature for the investigated compounds are tabulated for the sake of comparison. + SOC (NSOC) refers to calculations performed with (without) including spin-orbit coupling (SOC)

$Tl_2CdGeSe_4$

	Present		Expt [24]	Other[27]
	NSOC	**+SOC**		
a	7.8739	7.9453	8.0145	8.4502
d (%)	− 1.7	-0.8		5.4
c	6.7256	6.7107	6.7234	6.7740
d (%)	0.03	-0.2		0.4
V	416.976	423.632	431.859	483.703
d (%)	-3.5	-1.9		12.2
Se $_{x/a}$	0.1713	0.1689	0.1641	0.16044
Se $_{y/a}$	0.1713	0.1689	0.16410	0.16044
Se $_{z/c}$	0.2166	0.2185	0.2819	0.28758

$Tl_2CdSnSe_4$

	Present		Expt [15]	[14]	Theory[16]
	NSOC	**+SOC**			
a	7.9125	7.9888	8.04802	8.04901	8.1673
d (%)	-1.6	-0.7			1.5
c	6.8216	6.8651	6.8569	6.8573	6.9405
d (%)	-0.5	0.1			1.2
V	427.084	438.137	444.123	444.260	462.964
d (%)	-3.8	-1.3			4.2
Se $_{x/a}$	0.1759	0.1762	0.1742	0.1713	0.1761
Se $_{y/a}$	0.1759	0.1762	0.1742	0.1713	0.1761
Se $_{z/c}$	0.2275	0.2352	0.240	0.2520	0.2366

Table III.2: Calculated equilibrium interatomic distances (d, in Å), number of identical bonds (N.B.), and coordination numbers (C.N.) of atoms in the $Tl_2CdGeSe_4$ and $Tl_2CdSnSe_4$ including spin-orbit coupling, compared to available data in the literature

$Tl_2CdGeSe_4$				
Atom	Bond (N.B.)	d (Å)		C.N.
		Present	Expt.[15]	
Tl	Tl–Se (4)	3.2972	3.336	8
	Tl–Se (4)	3.5055	3.545	
Cd	Cd–Se (4)	2.6777	2.65	4
Ge	Sn–Se (4)	2.3986	2.368	4
Se	Se–Ge (1)	2.3986	0.2368	6
	Se–Cd (1)	2.6777	2.65	
	Se–Tl (2)	3.2972	3.336	
	Se–Tl (2)	3.505	3.545	

$Tl_2CdSnSe_4$					
Atom	Bond (N.B.)	d (Å)			C.N.
		Present	Expt.[15]	Expt. [14]	
Tl	Tl–Se (4)	3.3572	3.42	3.433	8
	Tl–Se (4)	3.4545	3.453	3.447	
Cd	Cd–Se (4)	2.6933	2.58	2.587	4
Sn	Sn–Se (4)	2.5673	2.63	2.605	4
Se	Se–Sn (1)	2.5673	2.63	2.605	6
	Se–Cd (1)	2.6933	2.58	2.587	
	Se–Tl (2)	3.3572	3.42	3.433	
	Se–Tl (2)	3.4545	3.453	3.447	

This excellent consistency between the calculated values and the experimental counterparts confirms the reliability of the PP-PW method in predicting the optimized structural geometry. Note that the unit cell parameters of $Tl_2CdSnSe_4$ are somewhat larger than those of $Tl_2CdGeSe_4$. Since all constituent atoms except D^{IV} (D^{IV} = Ge, Sn) are the same, the increase in unit cell volume when Sn substitutes for Ge is attributed to the fact that the atomic radius of the Sn atom (R = 2.81Å) is somewhat larger than that of the Ge atom (R = 2.45Å). To check the dynamic stability of the title compounds, the phonon-dispersion curves along the high symmetry lines in the Brillouin zone were calculated for both compounds. As seen from the phonon-dispersion curve of $Tl_2CdGeSe_4$ represented in Fig.III.2, the dispersion branches have positive frequencies at any vector, suggesting that the compounds of interest are dynamically stable.

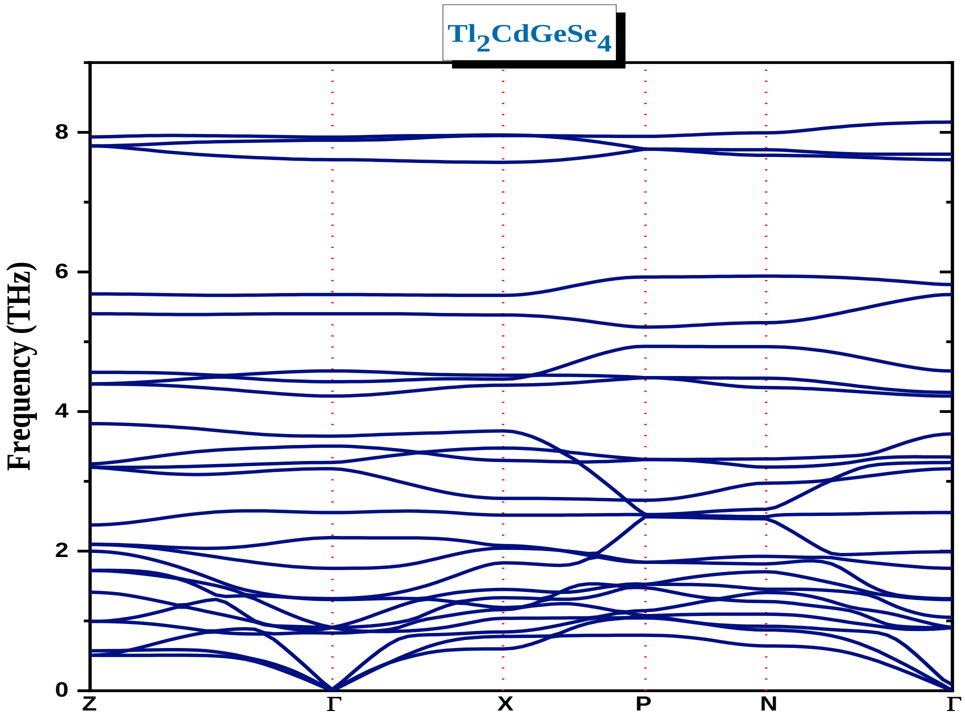

Figure III.2: Calculated phonon dispersion along the high symmetry lines in the Brillouin zone for $Tl_2CdGeSe_4$

III.2.2. Elastic properties of the Tl_2CdXSe_4 (X= Ge, Sn) compounds

III.2.2.1. Preamble

Elastic properties describe the mechanical behavior of materials; their measurement provides information about the forces binding the atoms or ions that make up a solid. A body, that is acted on by external forces, or, more generally, a body in which one part exerts a force on neighboring parts, is said to be in a state of stress are described by stress tensors that determine the direction of the forces and the plane on which they apply. A solid body changes its shape when subjected to stress. Provided the stress is below a certain limiting value (For small stresses, the elastic modulus is constant and the material behaves elastically), the elastic limit, the strain is recoverable, and that is to say, the body returns to its original shape when the stress is removed. The proportionality between stress and deformation within the limit of small deformations are respectively described by two symmetric tensors of second order σ_{ij} and ε_{ij}. The proportionality between the two tensors introduces two characteristic constants of the material.

For the monocrystalline, we often use the constants of elasticity C_{ij} or of deformabilityS_{ij}. The C_{ij} values are closely related to a wide range of fundamental solid-state properties, such as mechanical stability, phonon dispersion, heat capacity, Debye temperature, Gruneisen parameter, thermal expansion, the character and strength of the interatomic bonds, elastic wave velocities and melting point.

For an isotropic material (a polycrystalline), we can measure the polycrystalline modulus of elasticity. B_V, G_V, B_R, G_R, B_H, and G_H, where the subscripts V, R, and H denote the Voigt, Reuss, and Hill approximations, respectively. , Young’s modulus E and Poisson’s ratio ν, etc.

III.2.2.1.1. Hooke's Law

The relation connecting the state of stress and strain is determined from the physical properties of the solid undergoing deformation. Hooke in 1960 determined the states of stress and strain produced in a body by applied forces. During the deformation, the removal of the external forces leads in some cases to the complete recovery of a body to the natural state; the strain is recoverable, while in other cases the body retains compressed even though the load is removed the strains called permanent or plastic strains. For many materials, the relation is linear if the magnitude of the stresses is confined to a certain range so the object returns to its original shape and size upon removal of the load. The linear low for the relationship between stress and strain is called the generalized Hook's law. The general and inverse form of writing Hooke's law is as follows:

$$\sigma_{ij} = C_{ijkl}\varepsilon_{kl} \qquad \text{(III. 1)}$$

$$\varepsilon_{ij} = S_{ijkl}\sigma_{kl} \qquad \text{(III. 2)}$$

C is a tensor of rank four, called the stiffness tensor or elasticity tensor, and S is called the elastic compliance constant. The stiffness tensor is represented by a matrix of real numbers that contains 81 constants of stiffness C_{ijkl}. The symmetry of the stress tensor and the strain tensor will reveal the symmetry of the quantities.

$$C_{ijkl} = C_{ijlk} = C_{jikl} = C_{jilk} \qquad \text{(III. 3)}$$

Generally, reduce the number of components independent $C_{ijkl}$from 81 to 36. The components C_{ijkl}become C_{ij} by transforming the indices by Voigt notation [18]. Thus, Voigt's notation makes it possible to transform the stress and strain tensors into 6-component vectors and therefore Hooke's law can be written as:

$$\sigma_i = C_{ij}\varepsilon_j \qquad \text{(III.4)}$$

With

$$\begin{pmatrix} \sigma_1 \\ \sigma_2 \\ \sigma_3 \\ \sigma_4 \\ \sigma_5 \\ \sigma_6 \end{pmatrix} = \begin{pmatrix} C_{11} C_{12} C_{13} C_{14} C_{15} C_{16} \\ C_{21} C_{22} C_{23} C_{24} C_{25} C_{26} \\ C_{31} C_{32} C_{33} C_{34} C_{35} C_{36} \\ C_{41} C_{42} C_{43} C_{44} C_{45} C_{46} \\ C_{51} C_{52} C_{53} C_{54} C_{55} C_{56} \\ C_{61} C_{62} C_{63} C_{64} C_{65} C_{66} \end{pmatrix} \begin{pmatrix} \varepsilon_1 \\ \varepsilon_2 \\ \varepsilon_3 \\ \varepsilon_4 \\ \varepsilon_5 \\ \varepsilon_6 \end{pmatrix} \qquad \text{(III. 5)}$$

The symmetry elements of the crystal further reduce the number of independent constantsC_{ij}. Where

$$C_{ij} = C_{ji} \qquad \text{(III. 6)}$$

The symmetry of the C_{ij} matrice implied by relations (III.3) further reduces the number of independent stiffness constants and compliances from 36 to 21; these numbers will be decreased when we consider the symmetry of the crystal.

For a tetragonal material, the number of independent elasticity constants is reduced to six independent elastic constants in the form of the elastic matrix [19]:

$$C_{Tetrag} = \begin{pmatrix} C_{11} & C_{12} & C_{13} & & & \\ . & C_{11} & C_{13} & & & \\ . & . & C_{33} & & & \\ & & & C_{44} & & \\ & & & & C_{44} & \\ & & & & & C_{66} \end{pmatrix} \quad \text{(III. 7)}$$

III.2.2.1.2. Mechanical Properties

- Young's modulus (modulus of elasticity E): is the constant that connects the tensile stress (or compression) and the deformation for an isotropic elastic material, it is defined as the ratio of tensile stress σ to tensile strain Ɛ. It is constant that this compression remains small and that the elasticity limit of the material is not reached, whose stress is one-dimensional:

$$E = \frac{\sigma}{\varepsilon} \quad \text{(III. 8)}$$

- Poisson coefficient (ν): the ratio of transverse contraction strain versus longitudinal extension strain under a stretching force (unit transverse contraction/unit axial elongation).

$$\nu = \frac{(l_0 - l)/l_0}{(L_0 - L)/L_0} = -\frac{\Delta l/l_0}{\Delta L/L_0} = \frac{\varepsilon_{transveral}}{\varepsilon_{longitudinal}} \quad \text{(III. 9)}$$

The typical value of Poisson’s ratio for a covalent material is 0.2, while it is in the range of 0.3–0.4 for an ionic material and equal to 0.5 for the pure-ionic limit and the material is perfectly incompressible [21].

- The bulk modulus (B): is defined as the relative change in volume V under applied pressure P, which can be expressed as follows

$$B = -V\frac{dP}{dV} \quad \text{(III. 10)}$$

The bulk modulus is an extension of Young's modulus to three dimensions.

- The shear modulus (G): is a measure of strain strength, relates shear stress and strain for an isotropic elastic material, which describes the deformation of shape at constant volume.

To verify the brittleness or ductility of the studied materials are three important parameters, we can calculate Pugh's ratio (B/G), Poisson ratio (ν) and Cauchy pressure (C_{12}–C_{44}); the critical limits can be known from $\mathrm{B/G} > 1.75$, $\nu > 0.26$ for ductile nature and the opposite are true for fragile materials and if C_{12}–C_{44} is negative, a material is brittle; otherwise, it is ductile. [22; 23]. Another factor value (G/B) is about 0.57 distinguishing between brittle and ductile materials. A low G/B value means ductility, while a high G/B value implies more brittleness [24]. In the case of an isotropic material, Poisson's ratio makes it possible to directly connect the shear modulus G to Young's modulus E ($E = 2G(1 + \nu)$ for isotropic and homogenous materials). Furthermore, the calculated isotropic bulk moduli B and shear moduli G allow the calculation of Young's modulus E and Poisson's ratio (ν) via the following relationships:

$$\nu = \frac{3B-2G}{2(3B+G)} \qquad \text{(III. 11)}$$

and

$$E = \frac{9BG}{3B+G} \qquad \text{(III. 12)}$$

The hardness of a material is characterized by both intrinsic and extrinsic properties. Intrinsic properties encompass bond strength, cohesive energy, and crystal structure. On the other hand, extrinsic properties include defects, stress fields, and morphology. Experimental hardness values vary depending on measurement methods, temperature, and other factors. Similarly, theoretical hardness values are influenced by the formalism used in calculations[25]. We can calculate Vicker's hardness (H_v) using Young's modulus E and Poisson's ratio. It is well established that diamond is the hardest material on earth. It has a Vicker's hardness value in the range of 70–150 GPa. Hardness is an important mechanical property that is defined as the resistance of a material to localized deformation [26] using the following expression:

$$H_V = \frac{(1-2\nu)E}{6(1+\nu)} \qquad \text{(III. 13)}$$

An empirical model for Vicker's hardness has been proposed by Chen et al ; this model may not accurately predict the hardness of pure metals or materials dominated by metallic bonding with a very low Pugh's modulus ratio[27]. (H_V) based on a large sample of measured values from the literature as follows:

$$H_v = 2(K^2 G)^{0.585} - 3 \qquad \text{(III. 14)}$$

Where$K = G/B$. The bulk and shear moduli are the most important parameters for identifying the hardness. The high hardness requires that the bulk and shear modulus be as large as possible [28; 29]. Generally, the shear modulus is a significantly better qualitative predictor of hardness than the bulk modulus [30]. We can conclude that the shear modulus is more closely related to the hardness than the bulk modulus.

The propagation velocities of longitudinal V_l and transverse V_t acoustic waves are derived from [31]:

$$V_l = \sqrt{\frac{E(1-\nu)}{\rho(1+\nu)(1-2\nu)}} = \sqrt{\frac{B+4G/3}{\rho}} \qquad \text{(III. 15)}$$

$$V_t = \sqrt{\frac{E}{2\rho(1+\nu)}} = \sqrt{\frac{G}{\rho}} \qquad \text{(III. 16)}$$

Where ρ is the mass density

The V_m, obtained using theoretical V_l and V_t, is:

$$V_m = \left[\frac{1}{3}\left(\frac{1}{V_l^3} + \frac{2}{V_t^3}\right)\right]^{-1/3} \qquad \text{(III. 17)}$$

The Debye temperature is an important parameter of a solid. It appears in equations describing properties resulting from atomic vibrations and in phonics theories. At low temperatures the vibrational excitations arise solely from acoustic vibrations. Debye temperature can be estimated numerically from the average sound wave velocity V_m as follows [31]:

$$T_D = \frac{h}{k_B} V_m \left[\frac{3n}{4\pi}\frac{N_A\,\rho}{M}\right]^{1/3} \qquad \text{(III. 18)}$$

Where; h is Plank's constant ($h = 6.6262.10^{-34}\ \mathrm{kg\ m^2 s^{-1}}$ (j. s)), is Boltzmann's constant ($k_B = 1{,}3806.10^{-23} \mathrm{m^2 Kg\ s^{-2}} (\mathrm{j.deg^{-1}})$), N_A is Avogadro's number, p is the density, M is the molecular weight of the solid and n is the number of atoms in the molecule[32].

Another significant parameter that can be derived from the elastic constants C_{ij} is the melting point T_m , which is the temperature at which a substance transitions from a solid to a liquid state. The melting point can be estimated using the following empirical formula[33]:

$$T_m = 354 + 4.5\,((2C_{11} + C_{33})/3)$$

Where T_m, is in K, $C_{11} and\ C_{33}$ in GPa.

Polycrystalline materials are composed of many crystallites of varying sizes and orientations. Theoretically, the bulk modulus (B) and shear modulus (G) are important parameters of crystals to depict their abilities to resist compression and shear deformations. In view of the Voigt and Ruess [19] models the isotropic polycrystalline elastic moduli B and G can be calculated from the single-crystal elastic C_{ij} and compliance constants (S_{ij} (it is not possible to measure the C_{ij} values in this case). In the Voigt approximation a uniform strain is assumed throughout the polycrystal, and the upper limits of B and G, viz., B_V and G_V, can be evaluated. While Reuss [33] assumed that the stress is everywhere uniform, so his approximation yields the upper bound (upper limit) for the B and G moduli, Hill's approximation [19] assumes that the arithmetic means of the Voigt and Reuss limits constitutes the best theoretical value for the polycrystalline modulus of elasticity. B_V, G_V, B_R, G_R, B_H, and G_H, where the subscripts V, R and H denote the Voigt, Reuss and Hill approximations, respectively[34, 35].

III.2.2.2. Monocrystalline elastic constants

The monocrystalline elastic constants C_{ij}mirror the extent of the crystals' ability to recover their original shape after the stress is removed within the elastic limit, so they are key mechanical parameters of crystals. The C_{ij}values are closely related to a wide range of fundamental solid-state properties, it is of fundamental and practical interest to evaluate the C_{ij}values of a crystal using reliable theoretical approaches and precise experimental techniques. we determined the lattice parameters to match experimental values, we employed the "Energy-strain" method via the CASTEP code to compute the six independent second-order elastic constants C_{11}, C_{12}, C_{13}, C_{33}, C_{44}, and C_{66} for Tetragonal crystal. We are not aware of any experimental or theoretical determination of the C_{ij}values for the compounds of interest; hence, our results, listed in Table III.3, are the first numerical assessment. From the predicted C_{ij} values, information on the elastic and mechanical properties can be extracted.

Table III.3: Calculated monocrystalline elastic constants (C_{ij}, in GPa) for the $Tl_2CdGeSe_4$ and $Tl_2CdSnSe_4$ compounds with (+ SOC) and without (NSOC) including spin-orbit coupling

System	C_{11}	C_{33}	C_{44}	C_{66}	C_{12}	C_{13}
$Tl_2CdGeSe_4$						
NSOC	46.1	75.0	16.3	13.6	19.2	19.1
+SOC	35.8	67.3	9.8	9.6	12.8	13.9
$Tl_2CdSnSe_4$						
NSOC	46.4	74.8	11.0	11.8	17.8	17.8
+SOC	40.3	67.4	13.2	14.4	15.2	14.4

Based on the results obtained, we can draw the following conclusions:

- The computed C_{ij} values fulfill all the necessary conditions for the mechanical stability of a tetragonal crystal [36]:

  $C_{11} > |C_{12}|; 2C_{13}^2 < C_{33}(C_{11} + C_{12});\quad C_{44} > 0;\ C_{66} > 0$. Thus, $Tl_2CdGeSe_4$ and $Tl_2CdSnSe_4$ are mechanically stable.
- The C_{11} value, which reflects the resistance to linear compression or elongation of the crystal along the a-axis, is noticeably smaller than the C_{33} value, which mirrors the resistance to linear compression or elongation along the c-axis, indicating that the studied compounds show higher stiffness against strains along the c-axis than against strains along the a-axis. This suggests that under the same perpendicular uniaxial stress, the crystal is more compressible along the a-axis than along the c-axis; thus, the linear compressibility is dependent on the crystal direction. This result indicates that the interatomic bonds along the a-axis are weaker than those along the c-axis.
- The C_{11} and C_{33} values are noticeably larger than those of C_{12}, C_{13}, C_{44} and C_{66}, which characterize the resistance to shear deformations, indicating that the studied compounds are more resistant to compression than to shear.
- The velocities of sound waves propagating along the main crystal directions can be deduced from the monocrystalline elastic constants. The formulas used and the obtained results for the velocities of sound waves propagating along the [100]/[010], [110], and [001] crystallographic directions are listed in Table III.4. Table III.4 shows that the sound wave velocities depend considerably on their own polarizations and on the crystal directions. The noticeable differences between the velocities of the sound waves propagating in the

considered principal directions constitute proof of the considerable elastic anisotropy of the compounds of interest. The longitudinally polarized sound wave propagating along the [001] crystallographic direction is the fastest. The sound wave velocity is closely linked to the lattice thermal conductivity; the lower the sound velocity is, the lower the lattice thermal conductivity. The relatively low values of the anisotropic sound wave velocities suggest that the lattice thermal conductivities of both considered compounds are lower.

Table III.4: Computed velocities (in ms^{-1}) of the anisotropic sound waves propagating in the [100], [110], and [001] crystallographic directions in the monocrystals $Tl_2CdGeSe_4$ and $Tl_2CdSnSe_4$, isotropic longitudinal, transversal and average sound velocities (V_l, V_m and V_t, in ms^{-1}), and Debye temperature, the melting point (T_D, T_m , in K) for the polycrystalline aggregates $Tl_2CdGeSe_4$ and $Tl_2CdSnSe_4$. The mass density ρ is equal to 7.1307 $g/cm^3$for $Tl_2CdGeSe_4$ and 7.2670 $g/cm^3$for $Tl_2CdSnSe_4$. L and T refer to longitudinal and transversal polarization of the sound wave, respectively. Calculations were performed including spin-orbit coupling

Direction	Polarisation	Formula	$Tl_2CdGeSe_4$	$Tl_2CdSnSe_4$
[100]	[100] (L)	$\sqrt{C_{11}/\rho}$	2241	2355
	[010] (T1)	$\sqrt{C_{66}/\rho}$	1160	1408
	[001] (T2)	$\sqrt{C_{44}/\rho}$	1172	1348
[110]	[110] (L)	$\sqrt{(C_{11}+C_{12}+2C_{66})/2\rho}$	2180	2928
	$[1\bar{1}0]$ (T1)	$\sqrt{(C_{11}-C_{12})/2\rho}$	1613	1727
	[001] (T2)	$\sqrt{C_{44}/\rho}$	1172	1348
[001]	[001] (L)	$\sqrt{C_{33}/\rho}$	3084	3045
	(001)Plane T	$\sqrt{C_{44}/\rho}$	1172	1348
V_l			1286	1422
V_t			2346	2494
V_m			1504	1573
T_D			150	155
T_m			562.3	576

III.2.2.3. Polycrystalline elastic moduli

Generally, the synthesized samples are polycrystalline aggregates of single-phase monocrystals with random orientation; therefore, it is impossible to measure the C_{ij} values in this case. Instead, we can measure the isotropic bulk modulus B (which reflects the resistance to volume change under the hydrostatic pressure effect) and the shear modulus G (which characterizes the resistance to shape change under the influence of shear force). Theoretically, it is possible to calculate the isotropic elastic moduli B and G of a material from its elastic constants (C_{ij}values) and compliance constants (S_{ij}values) via Voigt–Reuss–Hill (VRH) approximations [19]. Voigt approximation assumed a uniform strain throughout the polycrystal, the upper limits of B and G, viz., B_V andG_V, can be evaluated. In contrast, through the Reuss approximation, which is based on an assumption of uniform stress, we can estimate the lower limits of B and G, viz., $B_R$and G_R. Hill's approximation [19] assumes that the arithmetic mean of the Voigt and Reuss limits constitutes the best theoretical value for the polycrystalline modulus of elasticity. B_V, G_V, B_R, G_R, B_H andG_H, where the subscripts V, R, and H denote the Voigt, Reuss, and Hill approximations, respectively, are given by the following relationships [34, 35]:

$$\mathrm{B_V} = \frac{1}{9}\{2(\mathrm{C_{11}} + \mathrm{C_{12}}) + 4\mathrm{C_{13}} + \mathrm{C_{33}}\} \tag{III. 19}$$

$$\mathrm{G_V} = \frac{1}{30}(\mathrm{M} + 3\mathrm{C_{11}} - 3\mathrm{C_{12}} + 12\mathrm{C_{44}} + 6\mathrm{C_{66}});\ \mathrm{M} = \mathrm{C_{11}} + \mathrm{C_{12}} + 2\mathrm{C_{33}} - 4\mathrm{C_{13}} \tag{III. 20}$$

$$\mathrm{B_R} = \frac{\mathrm{C^2}}{\mathrm{M}};\ \mathrm{C^2} = (\mathrm{C_{11}} + \mathrm{C_{12}})\mathrm{C_{33}} - 2\mathrm{C_{13}^2} \tag{III. 21}$$

$$\mathrm{G_R} = 15\{(18\,\mathrm{B_V}/\mathrm{C^2}) + [6/(\mathrm{C_{11}} + \mathrm{C_{12}})] + (6/\mathrm{C_{44}}) + (3/\mathrm{C_{66}})\}^{-1} \tag{III. 22}$$

$$\mathrm{B_H} = \frac{\mathrm{B_V} + \mathrm{B_R}}{2} \tag{III. 23}$$

$$\mathrm{G_H} = \frac{\mathrm{G_V} + \mathrm{G_R}}{2} \tag{III. 24}$$

In addition, Young's modulus E reflects the resistance of a material to uniaxial stresses. It is defined as the ratio of the vertically applied linear stress and the linear strain. In another hand Poisson's ratio σ mirrors the tendency of a material to expand or contract in a direction perpendicular to a loading direction, given by the negative value of the ratio of the transverse strain (vertical to the applied stress) to the longitudinal strain (in the direction of the applied stress), can be numerically estimated through the following relationships:

$$E = \frac{9BG}{3B+G};\ \nu = \frac{3B-2G}{2(3B+G)} \qquad \text{(III. 25; 26)}$$

Table III.5: Predicted Reuss, Voigt, and Hill bulk ($B_R, B_{V,}$ andB_H, in GPa) and shear ($G_R, G_{V,}$ and G_H, in GPa) moduli, Hill Young's modulus (E_H , E_V, E_R, in GPa) and Hill Poisson's ratio(ν_R , ν_V , ν_H dimensionless) for the polycrystalline aggregates $Tl_2CdGeSe_4$ and $Tl_2CdSnSe_4$. + SOC (NSOC) refers to calculations performed with (without) including spin-orbit coupling (SOC)

System		$Tl_2CdGeSe_4$		$Tl_2CdSnSe_4$	
		NSOC	+SOC	NSOC	+SOC
B_V		31.3	24.5	30.5	26.2
B_R		30.0	22.6	29.3	25.0
B_H		30.6	23.5	29.9	25.6
G_V		16.6	12.4	14.4	15.1
G_R		15.8	11.3	13.1	14.4
G_H		16.2	11.8	13.9	14.7
E_j	E_x	36.2	30.0	37.74	33.32
	E_y	36.2	30.0	37.74	33.32
	E_z	63.9	56.4	64.87	59.39
E_V		42.3	31.8	37.3	37.9
E_R		40.3	29.0	34.2	36.2
E_H		41.3	30.4	35.8	37.1
ν_V		0.274	0.283	0.296	0.258
ν_R		0.275	0.285	0.305	0.259
ν_H		0.275	0.285	0.300	0.259

The values of the isotropic elastic moduli B, G, E, and ν deduced from the predicted C_{ij}values are gathered in Table III.5. From the obtained results, we can get the following information:

- The isotropic elastic moduli B, G, and E have relatively small values, reflecting the materials' low hardness and stiffness. Hardness is an important mechanical property that is defined as the resistance of a material to localized deformation [1; 26]. The calculated Vickers hardness (3.30 GPa for $Tl_2CdGeSe_4$ and 2.42 GPa for $Tl_2CdSnSe_4$) confirms the low hardness of these materials.
- The B value is practically double that of G, suggesting that shear deformation can occur more easily than volume change and that G is the decisive elastic modulus affecting the mechanical stability of the title compound [37].
- Poisson's ratio (ν) is often used to indicate plasticity in materials. Indeed, from the ν value, we can predict whether a material is ductile or brittle. When the ν value is greater than 0.26; the material is predicted to be ductile, and when it is lower than 0.26, the material is brittle [38]. According to this indicator, $Tl_2CdGeSe4$ is rather ductile, while $Tl_2CdSnSe_4$ is on the border between ductile and brittle. Based on the fact that the shear modulus G mirrors the resistance to plastic deformation and the bulk modulus B mirrors the resistance to fracture, another empirical indicator claims that the quotient of B and G (B/G) of the polycrystalline phase can provide information about plasticity in materials [39]. According to this indicator, a compound is ductile if the B/G ratio is greater than 1.75; otherwise, it is brittle. Our predicted B/G ratio values, B/G = 2.08 for $Tl_2CdGeSe_4$ and B/G = 1.74 for $Tl_2CdSnSe_4$, confirm the results already obtained through Poisson's ratio, i.e., that $Tl_2CdGeSe_4$ is ductile and $Tl_2CdSnSe_4$ is on the border between ductility and brittleness. A ductile material is easily machinable and resistant to thermal shock.
- The typical value of Poisson's ratio for a covalent material is ≈ 0.2, while it is in the range of 0.3–0.4 for an ionic material and equal to 0.5 for the pure-ionic limit [40]. Based on these criteria, $Tl_2CdGeSe_4$, with ν ≈0.285, and $Tl_2CdSnSe_4$, with ν ≈ 0.259, exhibit a mixture of covalent and ionic interatomic bonds, but the ionic character is dominant.
- The Debye temperature T_D, which is closely related to the thermal parameters of solids, can be predicted from the average velocity of the elastic wave V_m, which can be numerically estimated from the B and G values [40, 41]. The predicted V_m and T_D values are presented in Table III.4. A high Debye temperature mirrors a high associated thermal conductivity [32]. These low values of V_m and T_D denote a low thermal conductivity for the studied compounds.

III.2.2.4. Elastic anisotropy

Microcracks and mechanical failures can occur in crystals with notable elastic anisotropy [41]. Thus, it is essential to analyze the extent of elastic anisotropy to understand its mechanism and possibly find a procedure to improve the mechanical properties of crystals to avoid the drawbacks of elastic anisotropy. A variety of experimental and theoretical metrics have been established to quantify the extent of elastic anisotropy in materials [42]. Here, we used five different ways to probe the degree of elastic anisotropy in the studied materials.

- Since the shear modulus G is a key elastic parameter for the mechanical stability of materials, we start by evaluating the extent of the shear anisotropy through the calculation of the shear anisotropic factors A_1, A_2 and A_3. For a tetragonal system, $A_1 = A_2$. The shear anisotropic factor$A_1 = A_2$, which characterizes the anisotropy of shear caused by the application of stress on the crystallographic planes {100} along the crystallographic directions < 011 > (symbolized by < 011 > {100}) and along the directions < 010 > (symbolized by (< 010 > {100}), is defined as: $A_1 = A_2 = 4C_{44}/(C_{11} + C_{33} - 2C_{13})$. The shear anisotropic factorA_3, which characterizes the anisotropy of the < 110 > {001} and < 010 > {001} shear, is given by $A_3 = 2C_{66}/(C_{11} - C_{12})$[41, 43]. For isotropic shear, the corresponding anisotropic factor is equal to unity. Thus, the degree of deviation of the anisotropy factors from unity reflects the elastic anisotropy degree of the crystal. The calculated values for A_1/A_2 and A_3 are equal to 0.52 and 0.84 (0.67 and 1.15), respectively, for $Tl_2CdGeSe_4$ ($Tl_2CdSnSe_4$), suggesting that these compounds are characterized by a large shear anisotropy.
- The ratio of the linear compressibility along the c-axis (βc) to the linear compressibility along the a-axis (βa), defined as [43]

$$\beta_C/\beta_a = ((C_{11} - C_{13})(C_{12} - C_{13})/(C_{33} - C_{13})) \qquad \text{(III.27)}$$

  Is usually used to assess the degree of elastic anisotropy in crystals. The calculated β_c/β_aratios are equal to 0.39 for $Tl_2CdGeSe_4$ and 0.52 for $Tl_2CdSnSe_4$, highlighting the strong anisotropy of the linear compressibility in both studied compounds.
- A widely used metric to quantify the degree of elastic anisotropy in crystals is the so-called universal elastic anisotropy A^U, defined as follows [44]:

$$A^U = \frac{5G_V}{G_R} + \frac{B_V}{B_R} - 6 \qquad \text{(III. 28)}$$

Where B_V (G_V) and B_R (G_R) are the estimated values of B (G) according to Voigt and Reuss approximations, respectively. For a perfect isotropic crystal, A^U is equal to zero. We never expect perfect isotropic behavior in a crystal; thus, the more the value of A^U deviates from zero, the greater the elastic anisotropy of the crystal. The computed value of A^U is equal to 0.51 for $Tl_2CdGeSe_4$ and 0.60 for $Tl_2CdSnSe_4$, confirming that the title compounds are characterized by considerable elastic anisotropy.

- The percent anisotropy in compression (A_{comp}) and in shear (A_{shear}), defined as

$$\begin{cases} A_{comp} = ((B_V - B_R)/(B_V + B_R) \times 100) \\ A_{shear} = \left((G_V - G_R/G_V + G_R) \times 100\right) \end{cases} \qquad \text{(III. 29)}$$

Where the subscripts V and R denote the Voigt and Reuss limits, respectively, are helpful indicators for estimating the elastic anisotropy in compressibility and in shear, respectively [45]. The degree of deviation of A_{comp} and A_{shear} from 0% mirrors the extent of the elastic anisotropy. In our case, A_{comp} and A_{shear} are equal to 4.0% and 4.6%, respectively, for $Tl_2CdGeSe_4$ and 2.3% and 2.4%, for $Tl_2CdSnSe_4$. Once again, these indicators highlight the strong elastic anisotropy in the compression and shear of the title compounds.

- The three-dimensional (3D) representation of the crystal direction dependence of the elastic moduli is the most straightforward method and is widely used to illustrate the degree of elastic anisotropy in crystals. Note that the 3D representation of the crystal direction dependence of the modulus of elasticity is a closed surface, where the distance between the center of that surface and any point on the surface in a given direction is equal to the magnitude of the represented elastic modulus in that direction.

Therefore, for an isotropic elastic modulus, the aforementioned closed surface has a perfect spherical shape, and thus, the extent of the deviation of the shape of this surface from the perfect spherical shape reflects the degree of anisotropy of that elastic modulus. In the present study, the elastic anisotropy degree of the $Tl_2CdGeSe4$ and $Tl_2CdSnSe_4$ crystals was assessed using 3D representations of the directional dependence of Young's modulus (E) and linear compressibility (β). The linear compressibility (β) measures the relative linear shrinkage of a crystal subjected to compression along a given crystallographic direction. The crystal direction dependent Young's modulus E and linear compressibility β for a tetragonal system are given by the following relationships [45]:

$$\frac{1}{\mathrm{E}} = (\mathrm{l}_1^4 + \mathrm{l}_2^4)\mathrm{S}_{11} + \mathrm{l}_3^4\mathrm{S}_{33} + 2\mathrm{l}_1^2\mathrm{l}_2^2\mathrm{S}_{12} + 2(\mathrm{l}_1^2\mathrm{l}_3^2 + 2\mathrm{l}_2^2\mathrm{l}_3^2)\mathrm{S}_{13} + (\mathrm{l}_2^2\mathrm{l}_3^2 + \mathrm{l}_1^2\mathrm{l}_3^2)\mathrm{S}_{44} + \mathrm{l}_1^2\mathrm{l}_2^2\mathrm{S}_{66} \qquad \text{(III. 30)}$$

$$\beta = (\mathrm{S}_{11}+\mathrm{S}_{12} + \mathrm{S}_{13}) - (\mathrm{S}_{11} + \mathrm{S}_{12} + \mathrm{S}_{13} + \mathrm{S}_{33})\mathrm{l}_3^2 \qquad \text{(III. 31)}$$

Here, l_1, l_2 and l_3 are the directional cosines of a given crystal direction in spherical coordinates. The 3D representations of the directional dependence of the linear compressibility (β) and Young's modulus (E) as well as their projections in the (ac)/(bc) and (ab) planes for $Tl_2CdGeSe_4$ and $Tl_2CdSnSe_4$ are shown in Figs III.3 and 4, respectively. Note that the overall topology of the closed surfaces of the Young's modulus and linear compressibility in $Tl_2CdGeSe_4$ are similar to those in $Tl_2CdSnSe_4$. Clearly, the closed surfaces representing the directional dependence of E and β deviate sharply from a spherical shape, mirroring the strong elastic anisotropy of these compounds. To facilitate greater insight into the changes in Young's modulus and linear compressibility along different crystal directions in a plane, we plot the cross-sections of the 3D representations of E and β in the (ac)/(bc) and (ab) ((100)/(010) and (001)) planes in Figs III.2 and 3. These figures demonstrate the considerable deviation of the projections (cross-sections) of the directionally dependent Young's modulus and linear compressibility in the (ac)/(bc) plane from the circular form for both considered compounds, highlighting the strong anisotropy of E and β in this plane. While the cross-sections in the (ab) plane exhibit a perfect circular form for β, highlighting the isotropic character of β in the (ab) plane. The cross-sections of E in the (ab) plane exhibit weak anisotropy. The degree of elastic anisotropy can also be quantified from the relative difference between the minimum and maximum values of the elastic modulus.

Figures III.2 and 3 show that the linear compressibility of the title compounds reaches the maximum (β_{max}) when the stress is applied along any crystal direction in the (ab) ((001)) plane (note that the linear compressibility is isotropic in the (ab) plane) and is minimum (β_{min}) when the stress is applied along the c-axis, i.e., perpendicular to the (ab) plane. This indicates that when hydrostatic pressure is applied, the contraction of the title crystals that occurs along any direction in the (ab) plane is greater than that occurring along the other crystal directions. The βmax of $Tl_2CdGeSe_4$ ($Tl_2CdSnSe_4$) is equal to 18.514 (15.935) TPa^{-1}, and βmin is equal to 7.211 (8.028) TPa^{-1}. The difference between β_{max} and β_{min} is noticeable; the former is almost twice the latter, indicating that the linear compressibility is remarkably anisotropic. Young's modulus value reaches the maximum (E_{max}) when the unidirectional stress is applied along the [001] crystal direction, while it reaches the minimum (E_{min}) when the unidirectional stress is applied along the [111] crystal direction. The E max of $Tl_2CdGeSe_4$ ($Tl_2CdSnSe_4$) is equal to 59.3 (59.9) GPa and the E min is equal to 25.2 (32.6) GPa. These results show that the [001] crystal direction is more resistant to uniaxial compression than the other crystal directions. This is consistent with the result that C_{33} is the largest elastic constant. The relatively large difference between the E max and E min values, where the former is almost twice the latter, demonstrates the strong anisotropy of Young’s modulus. Note that this large difference between the maximum and minimum values of linear compressibility as well as the large difference between the maximum and minimum values of Young’s modulus can make the comparison between the theoretical values and the corresponding experimental values slightly complex because the values of these moduli of elasticity depend on the direction of the applied stress with respect to the crystal direction.

Figure III.3: The directional variation of linear compressibility (a) and Young's modulus (b) and their respective cross-sections (a) and (b) within the (ab), (ac), and (bc) planes of the $Tl_2CdGeSe_4$ compound

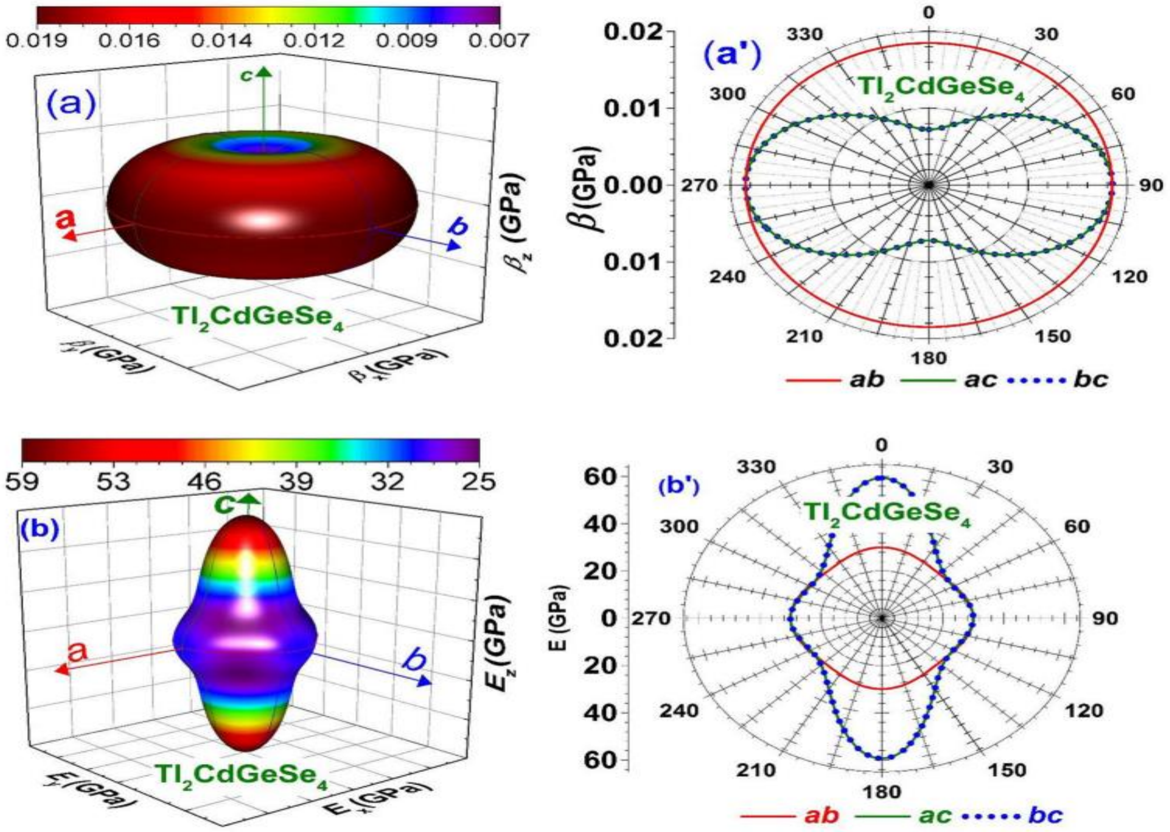

Figure III.4: The directional variation of linear compressibility (a) and Young's modulus (b) and their respective cross-sections (a) and (b) within the (ab), (ac), and (bc) planes of the $Tl_2CdGeSe_4$ compound

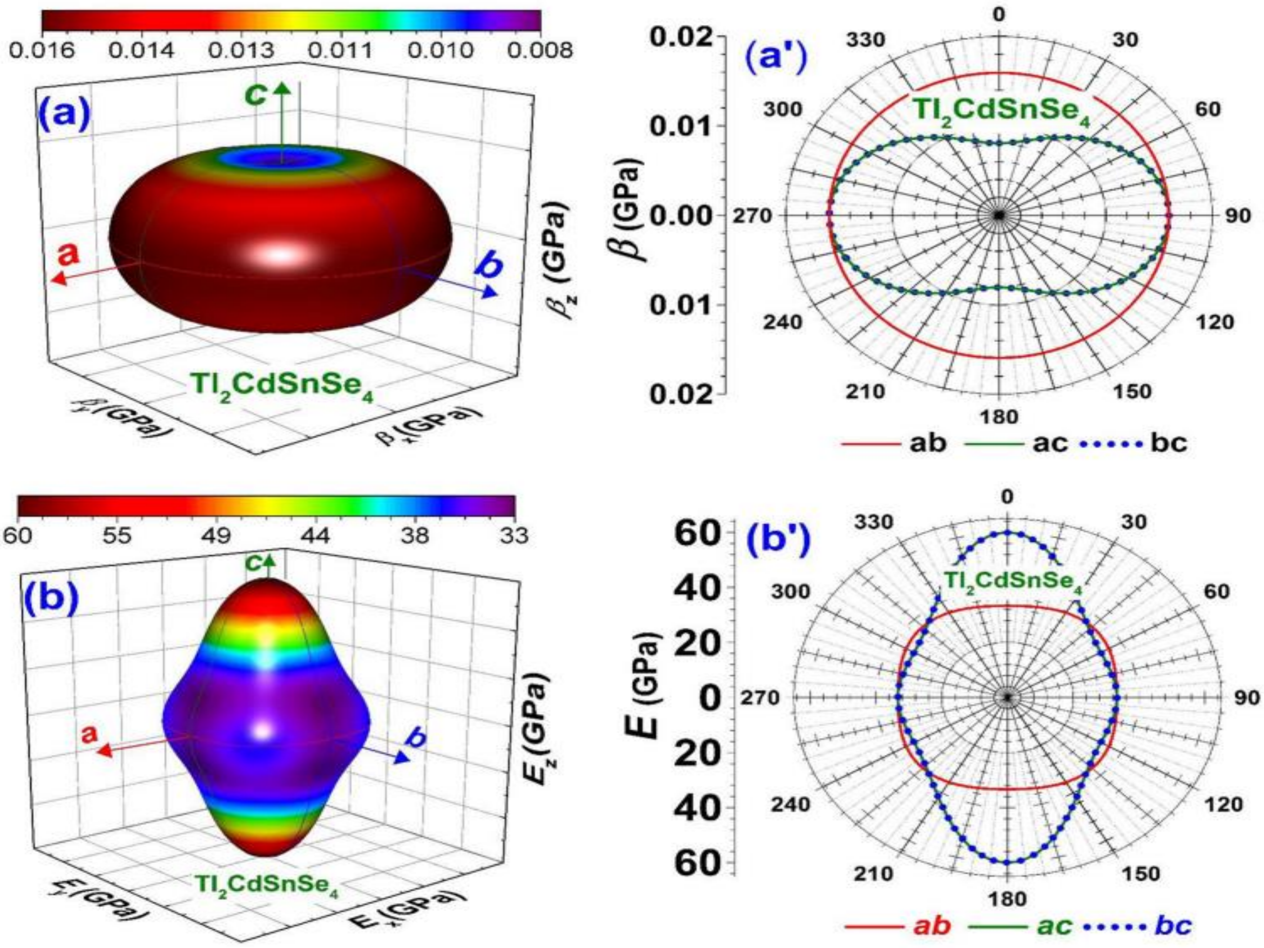

III.2.3. Electronic properties of the Tl_2CdXSe_4 (X= Ge, Sn) compounds

III.2.3.1 Preamble

It is well known in atomic physics when an atom is far apart or isolated the electrons levels (atomic orbitals) have a discrete energy level. As the atoms are brought closer, the electronic states are perturbed by the presence of neighboring atoms, their atomic orbitals overlap and discrete states broaden to form bands. The Pauli principle requires that no more than two electrons, of opposite spins, May occupy the same orbital state which is a state entirely defined by the space coordinates alone. Therefore, when two atoms are very close to each other, their respective energy bands will overlap with each other and transform into a Molecular orbit; each molecule orbital split into two, and the molecular orbit ends up having two discrete energy levels, the same thing happens when N atoms combine. In general, the more we add atoms; the more energy levels the molecular orbit will have (each atomic orbital splits into N discrete molecular orbitals, each one with a different energy). A solid cube one centimetre on an edge may contain 10^{23} atoms packed together; each molecular orbital of this solid will now have 10^{23} discrete energy levels. The gaps between them will be tiny such that, we no longer can we notice individual energy levels, it will appear that the energy is continuous (form an energy continuum called energy band) [47; 48].

Band theory helps to know the nature of materials, whether they are conductors, semi-conductors, or insulators; the forbidden band allows that, which separates the conduction (consists of free electrons) and valence band (consists of valence electrons). In an insulator, the valence band which is the highest energy electron is completely filled, and the band gap is more than 5 eV. When the conduction and valence bands overlap the material is a conductor (metal) and the conduction band is half full at 0 K and has a very low resistivity so a very high conductivity because of the very large number of electrons that can participate in current transport. In a semi conductor, the conduction band is unfilled and the valence band is normally filled. Semi-conductor materials have zero conductivity at 0 K, and quite low conductivity at finite temperatures, but it is possible to alter their conductivity by orders a magnitude, and at finite temperatures some electrons leave the valence band and occupy the conduction band. The band gap is between 1 to 5 eV; which allows electrons excited from the valence band to the conduction band by absorption of light in the visible and near infra-red region of the electromagnetic spectrum. It characterizes by three mechanisms, photon absorption, thermal, impurity (i.e. doping), Carriers that make it to the next band are like free carriers with new mass, m*. This is the key reason why semiconductor can be used in active devices [35; 49; 50].

III.2.3.2 Energy band dispersion

Some key physical parameters, especially those required for optoelectronic devices, such as bandgaps, effective masses of charge carriers, optical coefficients and transport parameters, are calculated from the energy band structure. Therefore, it is crucial to use an accurate theoretical method to correctly describe the energy band dispersions to obtain accurate estimations of the relevant properties. In the present work, the energy band dispersions along the lines joining the high symmetry points in the first Brillouin zone (X–M– Γ–Z–N–P–X) were calculated for $Tl_2CdGeSe_4$ and $Tl_2CdSnSe_4$ in their equilibrium crystal structures using the FP- (L)APW + lo approach within the DFT framework. Both the GGA-PBEsol and TB-mBJ functionals were used to model the exchange-correlation interactions, and calculations were performed both with and without spin-orbit coupling, referenced as + SOC and NSOC, respectively. From the band structure diagrams shown in Fig III.5, we highlight the following characteristics: First, the energy band structure diagrams of the studied compounds are very similar. This is attributed to the fact that these quaternary compounds have identical crystal structures, and three similar component atoms and the different component atoms belong to the same column of the periodic table. Second, the energy levels in the upper valence band at the M and Z points are so close to each other that it is difficult to determine which is the topmost of the valence band without carefully looking at the curve of the upper valence band and examining the numerical values of the energy levels. The numerical values show that the energy level in the upper valence band at the M-point is slightly higher than that at the Z-point for both considered materials, indicating that the valence band maximum (VBM) is located at the M-point for both compounds. As the conduction band minimum (CBM) is also located at the M-point for both compounds, we can state that both studied compounds are direct bandgap (M–M) semiconductors. Note that previous calculation results [27, 29] have shown that $Tl_2CdSnSe_4$ is a direct bandgap (M–M) semiconductor [27], which agrees with our findings, while $Tl_2CdGeSe_4$ has been shown to be an indirect bandgap (Z–M) semiconductor [29], which is inconsistent with what we found. To verify our results, the band structure calculation for $Tl_2CdGeSe_4$ was repeated using the PP-PW method as implemented in the CASTEP code [34], and the resulting bandgap character agrees with the results we obtained using the FP-LAPW method. Note that the band structure calculated by Vu et al [29].

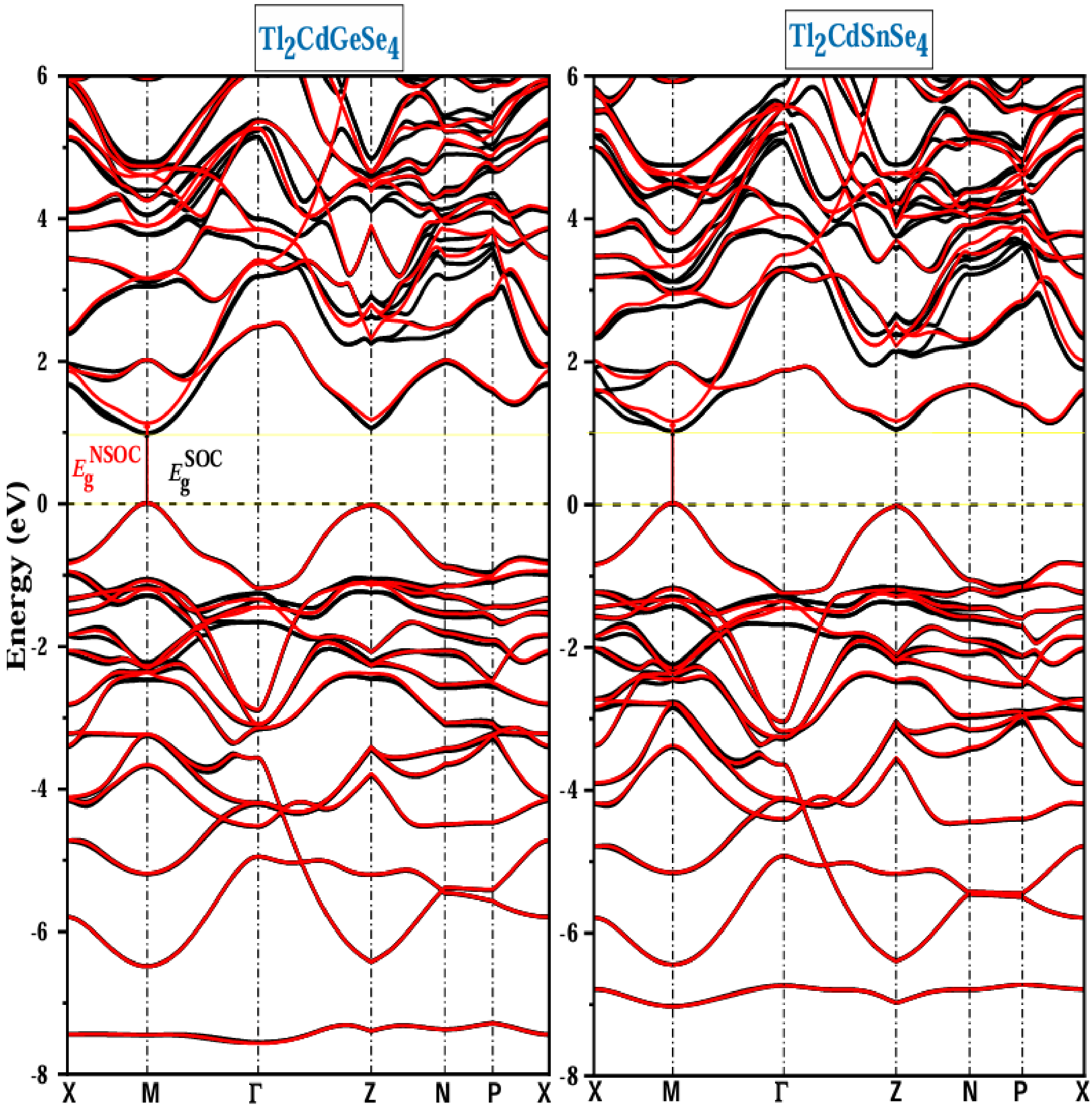

Figure III.5: The calculated TB-mBJ energy band structures for $Tl_2CdGeSe_4$ and $Tl_2CdGeSe_4$ along the X → M → Γ → Z → N → P → X k-point path. The VBM and CBM lie both at the M-point, thus both compounds are direct bandgap semiconductors. The black and the red lines represent the bands calculated with and without spin–orbit coupling, respectively. The zero of energy is chosen to coincide with the top of the valence band. E_g^{SOC} (E_g^{nsoc}) is the fundamental bandgap calculated with SOC (without SOC)

Also shows that the energy levels in the upper valence band at the M and Z points are so similar to each other that it is difficult to tell which is the topmost of the valence band without examining the numerical values of the energy levels. If we take into account that our optimized structural parameters with which the band structure of $Tl_2CdGeSe_4$ was calculated are slightly smaller than those with which Van et al [29]. Calculated the band structure (see Table III.1), it can therefore be stated that the bandgap may change from the direct type (M–M) to the indirect type (Z–M) depending on the values of the structural parameters with which the band structure is calculated. It should be noted that our optimized structural parameters for $Tl_2CdGeSe_4$ are more in agreement with the corresponding experimental counterparts than those optimized by Van et al. [29] (see Table III.6). Third, the energy band around the CBM is slightly more dispersive than that around the VBM, indicating that the electron effective mass is somewhat greater than that of the holes. Fourth, the energy band dispersions calculated using GGA08 and TB-mBJ have similar general characteristics, but they are significantly different with regard to the bandgap values. The predicted fundamental bandgaps using GGA08 and TB-mBJ both with and without taking into account spin–orbit coupling are gathered in Table III.5 along with available data from the literature [26, 27]. Table 6 shows that the GGA-PBEsol functional seriously underestimates the bandgaps compared to the counterparts provided by the TB-mBJ potential and the experiments [26, 27]. 75The use of the TB-mBJ potential with the inclusion of SOC widens the bandgap by more than 222% for $Tl_2CdGeSe_4$ and by more than 252% for $Tl_2CdSnSe_4$ compared to the GGA-PBEsol bandgap. Generally, the TB-mBJ potential rigidly pushes the conduction band toward higher energy away from the valence band maximum [51]. Fifth, the inclusion of SOC does not significantly affect the overall appearance of the energy band dispersions; in particular, the bands around CBM and VBM are almost unaffected by the inclusion of SOC, as expected from their Se-4p character. The only notable change in the band structure with SOC (+ SOC) is an approximately 13% reduction in the bandgap with respect to that of the counterpart calculated without SOC (NSOC); the CBM shifts to lower energies, thus decreasing the bandgap. Sixth, despite the considerable improvement of the bandgaps when using the TB-mBJ potential compared to the counterparts calculated using GGA-PBEsol, our numerical estimations of the bandgaps remain somewhat smaller than the experimental counterparts [26, 27], by about 35% for $Tl_2CdGeSe_4$ and 20% for $Tl_2CdGeSe_4$. A possible reason for the discrepancy between the theoretical predictions and the corresponding experimental values may be the uncertainties in the measurements. Indeed, even a small uncertainty in the measured spectra of the absorption coefficients from which the reported bandgaps were deduced could cause this discrepancy. Note that the reported bandgaps were evaluated from the tangent of the absorption coefficient at the lower energy and any deviation of the plotting tangent could cause a noticeable deviation in the determined bandgap value.

Thus, it is not easy to evaluate the error in the deduced bandgap from the measured absorption coefficient, which justifies why there is no information on the accuracy of the reported experimental data. Furthermore, small differences in the structural parameters could sometimes produce, for the same semiconductor, an appreciable difference in the calculated bandgap, possibly larger than 20% [47]. Note that there is no exchange-energy functional from which the TB-mBJ potential is derived; thus, the calculation of the optimized structural parameters is not possible within the TB-mBJ potential. Additionally, note that sometimes the optical bandgap is larger than the Kohn–Sham bandgap because sometimes the lower energy electronic transitions from the conduction band to valence band could be forbidden according to the selection rules. Further theoretical and experimental studies of the electronic structures of the considered systems are necessary to increase the reliability of both calculations and measurements.

Table III. 6: Energy bandgaps of $Tl_2CdGeSe_4$ and $Tl_2CdSnSe_4$ compounds using different methods: GGA-PBEsol and TB-mBJ. We considered both spin–orbit coupling (SOC) and the absence of spin–orbit coupling (NSOC). Our calculations were compared with existing theoretical and experimental data found in the literature

Functional	Bandgap (eV)	
	$Tl_2CdGeSe_4$	$Tl_2CdSnSe_4$
Present		
GG08-NSOC	0.431	0.398
GG08 + SOC	0.305	0.271
TB-mBJ +SOC	0.981	0.953
TB-mBJ NSOC	1.123	1.097
Expt. [25]	1.71[1]	1.39[1]
[26]	1.32[1]	1.29[2]
Calc. [26]	1.143[3]	1.243[4]

---

[1] From the absorption coefficient measurements; [2] From the photoconductivity Measurements;

[3] Using the TB-mBJ + SOC ; [4] TB-mBJ-NSOC

III.2.3.3 Charge carrier effective masses

The effective masses of charge carriers are key to the transport phenomena in materials. Thus, it is of great importance to estimate the effective masses of charge carriers in semiconductors. The effective mass is a tensor, but it can be treated as a scalar at the extremum of the energy bands. The dispersion of the energy band in the vicinity of its extremum can be adjusted by a parabola:

$$\mathrm{E(k)} = \frac{\hbar^2 \mathrm{k}^2}{2\mathrm{m}^*} \qquad \text{(III. 32)}$$

Where ħ is Planck's constant and m^* is the charge carrier effective mass. Thus, the charge-carrier m^* can be determined through the following expression:

$$\frac{1}{\mathrm{m}^*} = \hbar^2 \left(\frac{\partial^2 \mathrm{E(k)}}{\partial^2 \mathrm{k}}\right) \qquad \text{(III. 33)}$$

Before that we must fit the dispersion E(k) of the topmost valence band and lowest conduction band around the VBM and CBM respectively, to a quadratic polynomial in the reciprocal lattice vector k where $\mathrm{E(k)} = \mathrm{Ak}^2$. The predicted electron and hole effective masses, denoted m_e^* *and* m_h^*, respectively, at the CBM (located at the M -point) and VBM (located at the M -point), respectively, toward the G and X points (M → Γ and M → X directions) in the Brillouin zone are gathered in Table III.7. The obtained results reveal that $m_e^* > m_h^*$, which means that the mobility of holes is higher than that of electrons. The effective masses of electrons and holes exhibit a very weak anisotropy; the electron and hole effective masses toward the M → Γ direction are approximately equal to the corresponding masses toward the M → X direction. The inclusion of SOC in the calculations somewhat increases the electron and hole effective masses (Fig III.5).

Table III. 7: Calculated effective masses of electrons (m_e^*) and holes (m_h^*) at the conduction band minimum (CBM) and valence band maximum (VBM), respectively. These values are determined at the M-point and are further analyzed towards the G and X points in the Brillouin zone

$Tl_2CdGeSe_4$

	m_e^*		m_h^*	
	M → Γ	M → X	M → Γ	M → X
GGA08	0.376	0.395	0.344	0.351
GGA08+SOC	0.422	0.452	0.346	0.356
TB-mBJ+SOC	0.732	0.738	0.394	0.402
TB-mBJ+NSOC	0.542	0.561	0.387	0.392

$Tl_2CdSnSe_4$

	m_e^*		m_e^*	
	M → Γ	M → X	M → Γ	M → Γ
GGA08	0.326	0.343	0.307	0.315
GGA08+SOC	0.419	0.457	0.313	0.317
TB-mBJ+SOC	0.514	0.551	0.351	0.354
TB-mBJ+NSOC	0.466	0.487	0.348	0.354

III.2.3.4 Density of states

To determine the origin of the electronic states forming the valence and conduction energy levels of the quaternary selenides $Tl_2CdGeSe_4$ and $Tl_2CdGeSe_4$, the total density of states (TDOS) and l-projected atomic resolved density of states (PDOS) were calculated using the TB-mBJ potential with SOC. As seen in Fig III. 6:

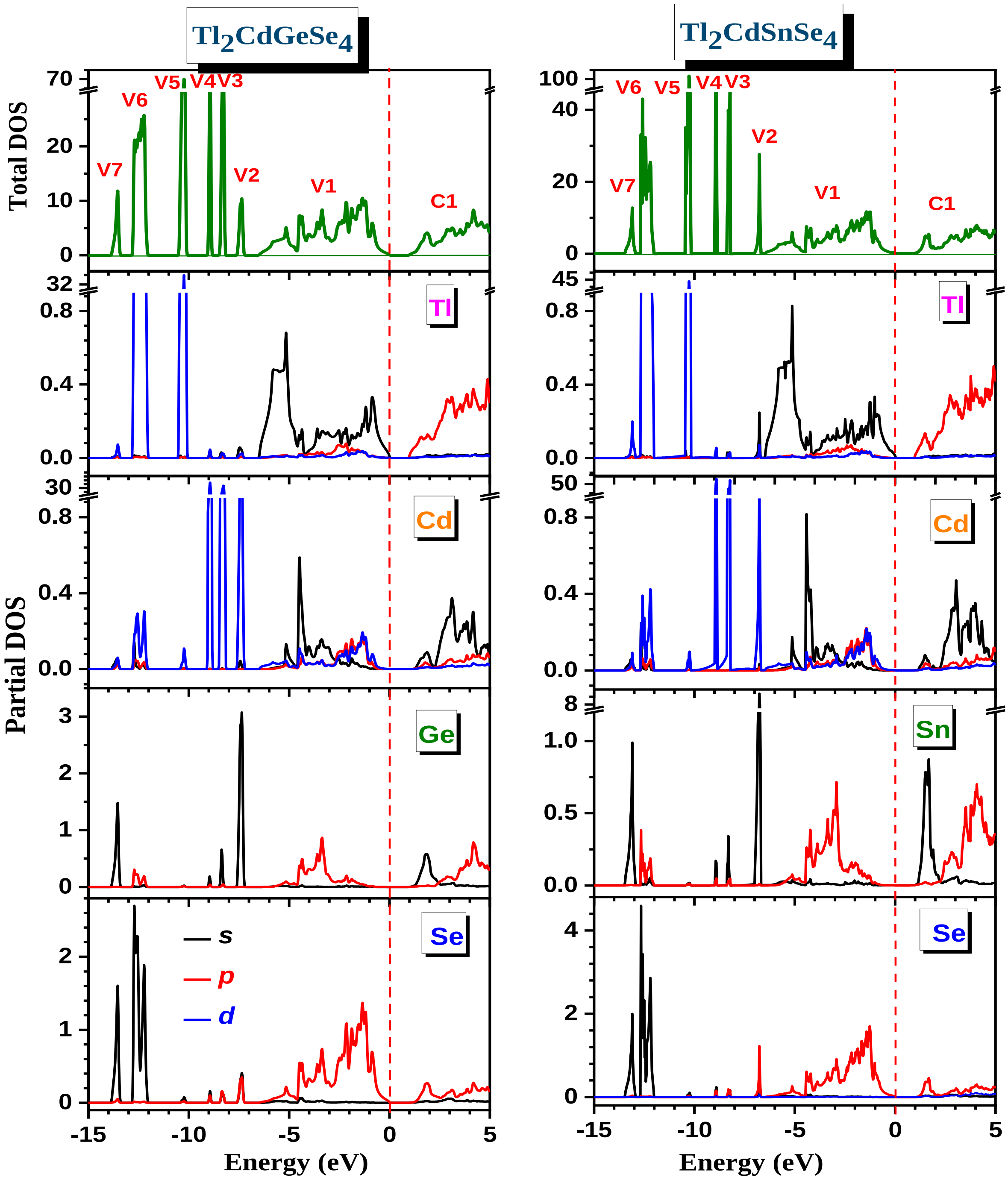

Figure III. 6: Total densities of states (TDOS) and partial densities of states (PDOS) were computed for $Tl_2CdGeSe_4$ and $Tl_2CdSnSe_4$ crystals using the TB-mBJ potential, taking into account spin-orbit coupling. The TDOS is given in states per eV per primitive cell, while the PDOS is expressed in states per eV per atom per orbital

The valence bands are regrouped in seven subbands denoted V1, V2, V3, V4, V5, V6 and V7. The V7, V6, V5, V4, V3 and V2 subbands are somewhat isolated, lying in narrow energy windows far from the upper valence band group V1. To shorten the text, the results relating to $Tl_2CdSnSe_4$ are given in brackets here after. The V7 subband, centered at − 13.5 (− 13.1) eV, comes from the Ge-4s (Sn-5s) and Se-4s states. The V6 subband, covering the energy range of − 12.9 to − 12.02 (− 12.7 to − 12.03) eV, is dominated by the contribution of the Tl-5d states, with a small contribution from the Se-4s states. The Tl-5d states form the V5 subband, peaking at − 10.2 (− 10.3) eV. The V4 subband, peaking at − 8.9 (− 8.9) eV, is composed of the Cd-4d states. The V3 band group, centered at − 8.3 (− 8.2) eV, is derived from the Cd-4d states. The V2 subband, centered at − 7.4 (− 6.8) eV, is a mixture of the Cd-4d and Ge-4s (Sn-5s) orbitals. As seen in Fig III.7, the upper valence band group V1, ranging from approximately − 6.5 (− 6.5) up to the Fermi level, is subdivided into two parts: V1-a and V1-b. The lower part, V1-a, ranging from approximately − 6.5 (− 6.5) eV to − 4.6 (− 4.5) eV, is composed of the hybridized Tl-6s and Se-4p states. The upper part, V1-b, ranging from approximately − 4.6 (− 4.5) eV to the Fermi level, is mainly associated with the Se-4p states, with a very small contribution from the Tl-6s, Cd-5s and Ge-4p (Sn-5p) states. This is quite consistent with the Se^{2-}, Tl^{1+} (the p shell is empty), Cd^{2+} and Ge^{4+}/Sb^{4+} oxidation states, suggesting that the Se–Tl, Se–Cd and Se–Ge (Sn) bonds predominantly exhibit ionic characteristics. In addition, the Se–Cd, Se–Tl and Se–Ge (Se–Sn) bonds are expected to have some degree of covalency due to weak hybridization between the Se-4p and Cd-5s states, between the Se-4p and Tl-6s states and between the Se4p and Ge-4p (Sn-5p) orbitals, respectively. The edge of the conduction band (the bottom of the C1 conduction subband) is mainly from the empty Se-4p and Ge-4s (Sn-5s) states, while the remainder of C1 is made up of a mixture of the Sn-sp, Cd-s, Tl-p and Se-p states, indicating that not all Se ions are saturated. Interestingly, in the case of $Tl_2CdGeSe_4$, the Se-4p states, which are the main contributors to the valence band, are positioned mainly in the upper part of the valence band and substantially in its central portion, while the main contributions of the Ge-4p states are in the central portion of the valence band. These theoretical findings are in excellent agreement with the experimental measurements of the energy distribution of the Se-4p and Ge-4p states in $Tl_2CdGeSe_4$ [29].

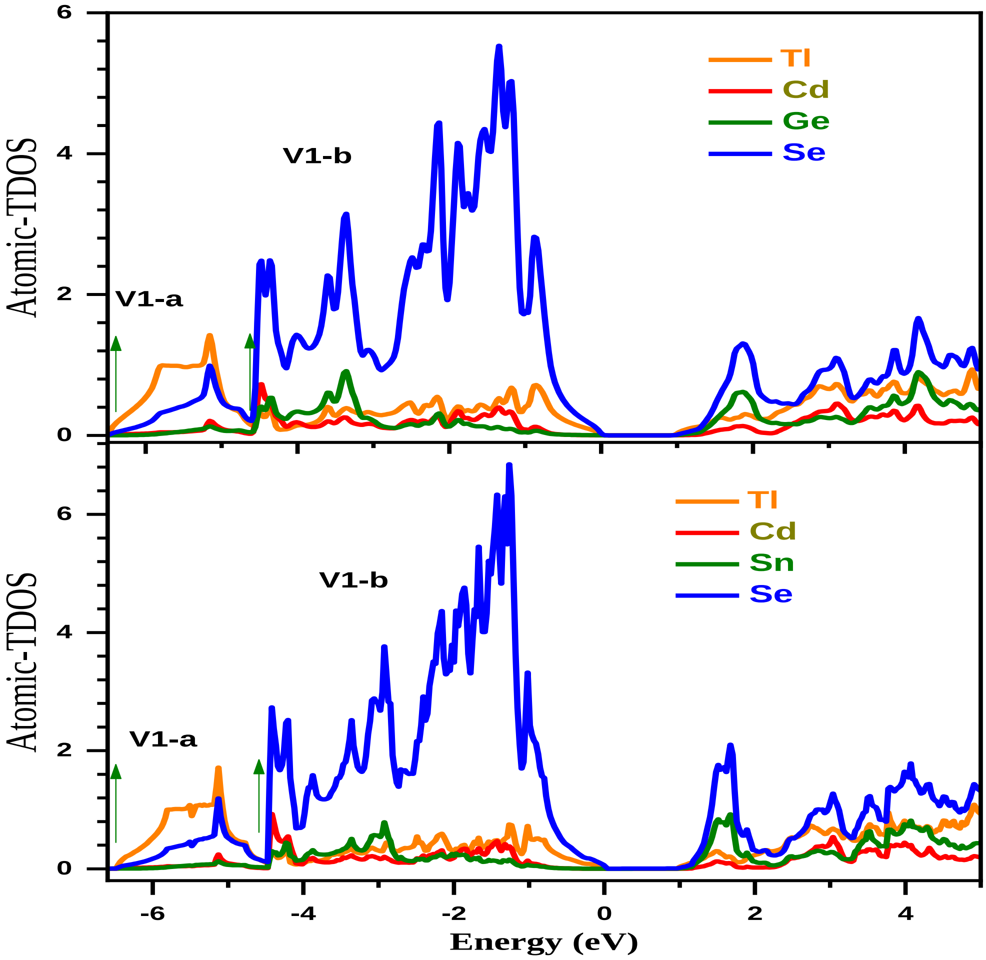

Figure III.7: The total densities of states (TDOS) for the upper valence subband in the Tl2CdGeSe4 and Tl2CdSnSe4 compounds at the atomic level

III.2.4. Optical properties of the Tl_2CdXSe_4 (X= Ge, Sn) compounds

Optical properties of a material change or affect the characteristics of light passing through it by modifying its propagation vector or intensity. The light is electromagnetic radiation, which includes infrared (IR) typically in fields 0.1 to 1 eV (12000_1200), visible range in 1.7 to 3 eV (700_400nm), ultraviolet (UV) between 3 to 100 eV (400_12). Optical properties of solids are dependent on their band gaps and can be gained from the complex dielectric function $\varepsilon(\omega) = \varepsilon_1(\omega) + i\varepsilon_2(\omega)$. The imaginary part ε2(ω) describes the electron transitions from occupied states below the fermi energy to unoccupied states above, so characterizes the absorption of the incident light by the matter, and it can be obtained by electronic structure through the joint density of states and the momentum matrix elements between the occupied and the unoccupied wave functions [52]

$$\varepsilon_2(\omega) = \frac{\mathrm{Ve}^2}{2\pi\hbar \mathrm{m}^2\omega^2} \int \mathrm{d}^3\mathrm{k} \sum_{\mathrm{nn}'} |\langle \mathrm{kn}|\mathrm{P}|\mathrm{kn}'\rangle|^2 \mathrm{f}(\mathrm{kn})\,[1 - \mathrm{f}(\mathrm{kn}')]\;\delta\,(\mathrm{E}_{\mathrm{kn}}\mathrm{E}_{\mathrm{kn}'} - \hbar\omega) \qquad \text{(III. 34)}$$

Where $\hbar\omega$ is the energy of the incident phonon, the $\langle \mathrm{kn}|\mathrm{P}|\mathrm{kn}'\rangle$ is the components of the dipole moment matrix, kn and kn′ are the initial and final states, respectively, $|\mathrm{kn}\rangle$ is the eigenfunction with eigenvalueE_{nk}, $f(\mathrm{kn})$ is the Fermi distribution function. $|\langle \mathrm{kn}|\mathrm{P}|\mathrm{kn}'\rangle|^2 \mathrm{f}(\mathrm{kn})(1 - \mathrm{f}(kn'))$ is the matrix element representing the probability of transition between the kn states of the valence band and the kn′ states of the conduction band. The conservation of energy during transitions is represented by the Dirac function: $\delta\,(\mathrm{E}_{\mathrm{kn}}\mathrm{E}_{\mathrm{kn}'} - \hbar\omega)$.

The real part $\varepsilon_1(\omega)$ can be attracted from the imaginary part $\varepsilon_2(\omega)$ using Kramer–Kronig relationship; and it depicts the polarization degree of the medium under an external electric field, it characterizes the dispersion of the incident radiation when it traverses a medium.

$$\varepsilon_1(\omega) = 1 + \frac{2}{\pi} P \int_0^\infty \frac{\omega'\varepsilon_2(\omega')}{\omega'^2\omega^2} d\omega' \qquad \text{(III. 35)}$$

Where ω is the frequency of the incident phonon, P the principal part of the Cauchy integral. There are two contributions to $\varepsilon(\omega)$, intraband transitions and inner-band (interband) transitions. The contribution from that intraband transitions is mainly present in metals while inner-band transitions occur primarily in semiconductors. Inner-band transitions can be divided into direct and indirect transitions. The indirect interband transitions are neglected which involves scattering of phonons and are expected to give only a small contribution to $\varepsilon(\omega)$[53].

Other optical properties are derived from the dielectric functions of solids such as absorption (The photons that constitute the light are absorbed by the material). Refraction (Photons pass through and do not interact with the medium (transmission), and change their velocity). Reflection (photons of identical energy are immediately reflected by the material). Loss of energy (loss of energy of a fast electron passing through matter).

The determination of the real and imaginary parts of the function dielectric allows us to evaluate other optical properties with the relations below: the absorption coefficient α(ω), the refractive index n(ω) , the extinction coefficient k(ω) , reflectivity R (ω), and the energy loss L(ω)

$$\alpha(\omega) = \frac{\sqrt{2}}{c}\omega\sqrt{-\varepsilon_1(\omega) + \sqrt{\varepsilon_1^2(\omega)+\varepsilon_2^2(\omega)}} \qquad \text{(III. 36)}$$

$$n(\omega) = \left[\frac{\varepsilon_1(\omega)}{2} + \frac{\sqrt{\varepsilon_1^2(\omega)+\varepsilon_2^2}}{2}\right]^{1/2} \qquad \text{(III. 37)}$$

$$k(\omega) = -\left[\frac{\varepsilon_1(\omega)}{2} + \frac{\sqrt{\varepsilon_1^2(\omega)+\varepsilon_2^2}}{2}\right]^{1/2} \qquad \text{(III. 38)}$$

$$R(\omega) = \left|\frac{\varepsilon(\omega)^{0.5}-1}{\varepsilon(\omega)^{0.5}+1}\right|^2 \qquad \text{(III. 39)}$$

$$L(\omega) = \left|\frac{\varepsilon_2(\omega)}{\varepsilon_1^2(\omega)\varepsilon_2^2(\omega)}\right| \qquad \text{(III. 40)}$$

At low frequency ($\omega = 0$), we get the following relationship:

$$n(0) = \varepsilon^{1/2}(0) \qquad \text{(III. 41)}$$

Figure 8 shows the spectra of the components of the imaginary part of the optical complex dielectric function, viz., $\varepsilon_2^{xx}(\omega)$ and $\varepsilon_2^{zz}(\omega)$, where $\varepsilon_2^{xx}(\omega)$ and $\varepsilon_2^{zz}(\omega)$ characterize the absorption of the energy of incident electromagnetic waves with an electric field vector E polarized parallel to the a-axis (E// a) and the c-axis (E// c), respectively. As clearly seen in the aforementioned figure, the $\varepsilon_2(\omega)$ spectra of both compounds exhibit notable anisotropy:

(i) the general characteristics of the spectra of the $\varepsilon_2^{xx}(\omega)$ and $\varepsilon_2^{zz}(\omega)$ components are remarkably distinct from each other throughout the considered energy window;

(ii) the number and positions of the major peaks and structures in the $\varepsilon_2^{xx}(\omega)$ spectrum are noticeably different from those in the $\varepsilon_2^{xx}(\omega)$ spectrum;

(iii) the amplitudes of the main peaks and structures of the $\varepsilon_2^{zz}(\omega)$ spectrum are remarkably higher than those of the $\varepsilon_2^{xx}(\omega)$ spectrum.

It is of fundamental interest to attempt to determine the microscopic origin of the electronic transitions between the occupied valence band states and the empty conduction band states that give rise to the peaks and structures of the $\varepsilon_2^{xx}(\omega)$ and $\varepsilon_2^{zz}(\omega)$ spectra based on the band structure and density of state diagrams. For this purpose, the $\varepsilon_2^{xx}(\omega)$ and $\varepsilon_2^{zz}(\omega)$ spectra were decomposed into the individual contributions of the electronic transitions between pairs of bands, $V_n \rightarrow C_{n'}$, where V_n is a valence band of index n and $C_{n'}$ is a conduction band of index n'. Once the pair of bands $(V_n, C_{n'})$ has been determined, we determine the wave vectors k of the electronic states that mainly contribute to the interband transition $V_n \rightarrow C_{n'}$ from the $(C_{n'} - V_n)(k)$ dispersion. Tables III.8, 9, 10 and 11 list the energetic positions of the main peaks (Pi) of the $\varepsilon_2^{xx}(\omega)$ and $\varepsilon_2^{zz}(\omega)$ spectra, the pairs of bands $(V_n, C_{n'})$ that dominantly contribute to the peaks and structures of the spectra and the electronic states involved in each interband direct transition $V_n \rightarrow C_{n'}$. Furthermore, based on the TDOS and PDOS diagrams, the main contributions to the $\varepsilon_2^{xx}(\omega)$ and $\varepsilon_2^{zz}(\omega)$ spectra in the energy range of 0–6 eV are the allowed direct interband electronic transitions from the valence subband V1 to the conduction subband C1. This evidence shows that the optical structures in the energy range of 0–6 eV in the$\varepsilon_2^{xx}(\omega)$ and $\varepsilon_2^{zz}(\omega)$ curves of the studied compounds mainly originate from the direct electronic transitions from the Se-4p occupied valence states to the Se-4p, Ge-4s (Sn-5s), Cd-5s and Tl-6p empty conduction states. Figure III.8 shows that the general characteristics of the $\varepsilon_1^{xx}(\omega)$ and spectra $\varepsilon_1^{zz}(\omega)$ (components of the real part of the dielectric function) are remarkably different, indicating the strong anisotropy of this optical property of the considered compounds. The peak amplitudes of the $\varepsilon_1^{zz}(\omega)$ spectrum are significantly higher than those of the $\varepsilon_1^{xx}(\omega)$ spectrum. The static components of the electronic part of the static dielectric constant ε(0), an optical parameter of crucial importance for optoelectronic devices, can be deduced from the limits of the $\varepsilon_1^{xx}(\omega)$ and $\varepsilon_1^{zz}(\omega)$ spectra when ω → 0. The estimated values of $\varepsilon^{xx}(0) = \varepsilon_1^{xx}(0) = \varepsilon_1^{xx}(\omega \rightarrow 0)$ and $\varepsilon^{zz}(0) = \varepsilon_1^{zz}(0) = \varepsilon_1^{zz}(\omega \rightarrow 0)$ are approximately equal to 8.23 and 8.82, respectively, for $Tl_2CdGeSe_4$ and 8.51 and 9.26, respectively, for

$Tl_2CdSnSe_4$. The $\varepsilon^{xx}(0)$ and $\varepsilon^{zz}(0)$ values of $Tl_2CdSnSe_4$ are slightly greater than those of $Tl_2CdGeSe_4$. This trend is consistent with Penn's model [54], which claims that a larger bandgap corresponds to a smaller static dielectric constant. The available data in the literature for the components of the static real part of the dielectric function for the $Tl_2CdSnSe_4$ compound ($\varepsilon_1^{xx}(0) = 14$ and $\varepsilon_1^{zz}(0) = 16.0$) [55] are almost double the values we obtained ($\varepsilon_1^{xx}(0) = 8.51$ and$\varepsilon_1^{zz}(0) = 9.26$. By comparing the magnitudes of our calculated $\varepsilon_2^{xx}(\omega)$ and $\varepsilon_2^{zz}(\omega)$ spectra with those reported in the literature [55], we notice that the magnitudes of the reported $\varepsilon_2^{xx}(\omega)$ and $\varepsilon_2^{zz}(\omega)$ spectra for $Tl_2CdSnSe_4$ are almost double those of our spectra. To check the reliability of our results, we recalculated the $\varepsilon_2^{xx}(\omega)$ and $\varepsilon_2^{zz}(\omega)$ spectra of $Tl_2CdSnSe_4$ using another computer code based on another ab initio method, and the obtained results are consistent with our previous results. A probable reason for the discrepancy between our results and those reported in the literature is that the results reported [55] were obtained using a relatively old version of the WIEN2k code, where the doubling of the number of energy bands upon inclusion of SOC is not taken into account when calculating optical properties. If the doubling of the number of energy bands when including SOC is not taken into account, the magnitude of the imaginary part of the dielectric function ($\varepsilon_2(\omega)$) is doubled, which has repercussions on the optical parameters deduced from $\varepsilon_2(\omega)$, such as the real part of the dielectric function ($\varepsilon_2(\omega)$) and all other optical functions.

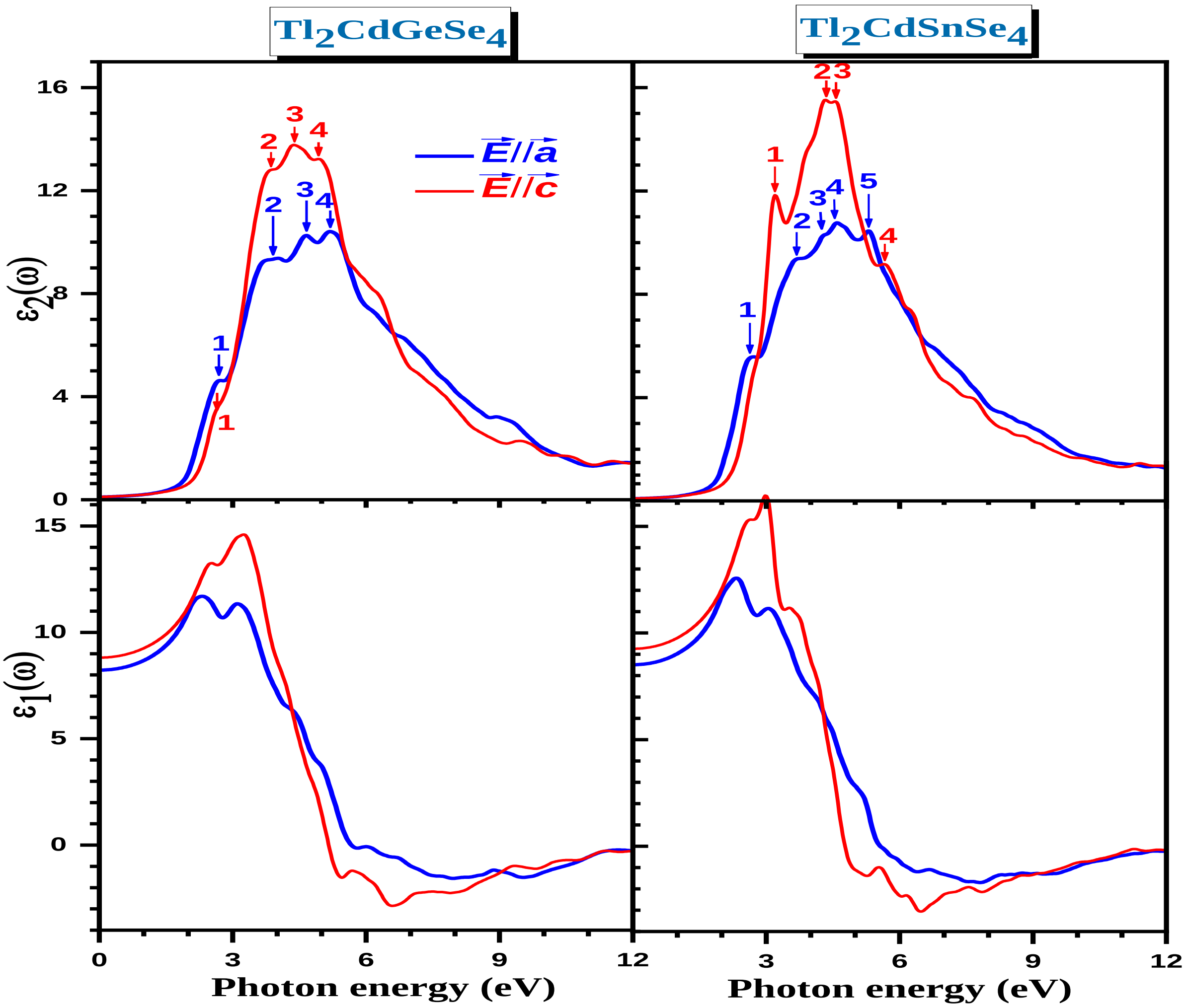

Figure III.8: Frequency dependent curves of the real ($\varepsilon_1(\omega)$) and imaginary ($\varepsilon_2(\omega)$) parts of the dielectric function for incident electromagnetic radiation polarized parallel to the a- and c-axes for the $Tl_2CdGeSe_4$ and $Tl_2CdSnSe_4$ materials. The critical point structures (peaks) are pointed out by the label i (i = 1, 2, 3. . .)

Table III. 8: Peak positions of the ε_2^{xx}spectrum for $Tl_2CdGeSe_4$, along with the prominent interband transition contributions for each peak in their location within the Brillouin zone. Bands are counted downward (upward) from the top (bottom) of the valence (conduction) band

Optical structure		Dominant interband transition contributions			
Peak	Position	Transition	BZ Region	Percentage	Position
E1	2.66	(V_1-C_1)	M-Γ-X,P-N	13.88	2.64
		(V_1-C_2)	X-M-Γ,X-P	2.18	2.64
		(V_2-C_1)	X-M-Γ,X-P	14.04	2.55
		(V_3-C_1)	X-M-Γ	2.08	2.66
E2	3.91	(V_1-C_2)	M-Γ-X-P-N-Γ	2.45	3.26
		(V_1-C_3)	M-Γ-X-P	8.28	3.66
		(V_2-C_2)	M-Γ-X, P-N-Γ	3.49	3.69
		(V_3-C_1)	M-Γ-X, P-N	2.36	3.11
		(V_3-C_2)	M-Γ-X-P-N-Γ	2.17	4.08
		(V_4-C_1)	X-M-Γ,X-P	3.10	3.02
		(V_4-C_2)	M-Γ-X-P-N-Γ	3.60	3.99
		(V_5-C_1)	X-M-Γ	6.39	3.21
		(V_5-C_2)	X-M-Γ-X-P-N-Γ	2.40	4.18
		(V_6-C_1)	M-Γ-X-P	4.86	3.99
		(V_6-C_2)	X-M-Γ-X-P-N-Γ	1.51	4.08
		(V_7-C_1)	X-M-Γ, X-P	2.47	4.08
E3	4.63	(V_1-C_5)	M-Γ-X-P, N-Γ	2.54	4.92
		(V_1-C_6)	X-M-Γ, X-P	5.34	4.82
		(V_2-C_3)	M-Γ-X-P	7.68	4.27
		(V_2-C_4)	M-Γ-Γ-X-P-N	5.51	4.86
		(V_3-C_3)	M-Γ-X-P, N-Γ	4.19	4.66
E4	5.20	(V_1-C_4)	M-Γ-X-P- N-Γ	3.41	4.57
		(V_3-C_4)	X-M-Γ-X-P- N-Γ	4.02	4.96
		(V_1-C_6)	M-Γ-X-P- N-Γ	4.33	5.11
		(V_2-C_5)	M-Γ-X-P, N-Γ	4.23	5.15
		(V_2-C_6)	X-M-Γ	3.95	5.35
		(V_2-C_7)	X-M-Γ-X-P	3.95	5.73
		(V_3-C_5)	X-M-Γ	3.39	5.15
		(V_3-C_6)	X-M-Γ-X-P-N-Γ	4.05	5.54
		(V_4-C_4)	M-Γ-X-P-N-Γ	2.14	5.24
		(V_4-C_6)	M-Γ-X-P- N-Γ	2.92	5.82
		(V_5-C_4)	M-Γ-X-P- N-Γ	2.18	5.54
		(V_6-C_4)	X-M-Γ-X-P	2.76	5.44
		(V_9-C_1)	M-Γ-X, P- N	3.31	5.15

Table III. 9: Peak positions of the ε_2^{zz}spectrum for $Tl_2CdGeSe_4$, along with the prominent interband transition contributions for each peak in their location within the Brillouin zone. Bands are counted downward (upward) from the top (bottom) of the valence (conduction) band

Optical structure		Dominant interband transition cntributions			
Peak	Position	Transition	Region	Percetage	Position
E1	2.6	$(V_1\text{-}C_1)$	M-Γ-X, P-N	4.71	2.74
		$(V_2\text{-}C_1)$	X-M-Γ,X-P	16.0	2.56
		$(V_3\text{-}C_1)$	X-M-Γ	3.76	2.51
E2	3.86	$(V_1\text{-}C_2)$	M-Γ-X-P-N-Γ	1.86	3.80
		$(V_2\text{-}C_2)$	M-Γ-X-P-N-Γ	4.46	3.90
		$(V_3\text{-}C_1)$	M-Γ-X,P-N	3.13	3.19
		$(V_3\text{-}C_2)$	M-Γ-X-P-N-Γ	4	3.90
		$(V_4\text{-}C_1)$	M-Γ-X,P-N	535	3.47
		$(V_4\text{-}C_2)$	M-Γ-X-P-N-Γ	2.25	3.96
		$(V_5\text{-}C_1)$	X-M-Γ,X-P	6.54	3.41
		$(V_6\text{-}C_1)$	M-Γ-X-P	3.81	3.85
E3	4.35	$(V_1\text{-}C_5)$	X-M-Γ,X-P	4.35	4.62
		$(V_2\text{-}C_3)$	M-Γ-X-P	5.72	4.27
		$(V_3\text{-}C_3)$	M-Γ-X-P	8.56	4.50
		$(V_5\text{-}C_2)$	M-Γ-X-P-N-Γ	2.19	4.69
		$(V_5\text{-}C_3)$	X-M-Γ-X-P	2.88	4.72
		$(V_6\text{-}C_2)$	M-Γ-X-P-N-Γ	4.61	4.59
		$(V_7\text{-}C_1)$	X-M-Γ, X-P	3.31	4.18
		$(V_8\text{-}C_1)$	X-M-Γ, X-P-N	4.33	4.72
E4	4.93	$(V_1\text{-}C_6)$	M-Γ-X-P-N-Γ	2.41	5.10
		$(V_2\text{-}C_4)$	M-Γ-X-P-N-Γ	2.61	4.86
		$(V_3\text{-}C_4)$	M-Γ-X-P-N-Γ	2.61	4.97
		$(V_3\text{-}C_5)$	X-M-Γ-X-P	3.05	5.17
		$(V_4\text{-}C_4)$	M-Γ-X-P	3.17	4.87
		$(V_4\text{-}C_5)$	M-Γ-X-P-N-Γ	2.46	5.49
		$(V_5\text{-}C_5)$	X-M-Γ-X-P-N-Γ	2.26	4.95
		$(V_6\text{-}C_3)$	X-M-Γ-X-P	2.83	5.21
		$(V_7\text{-}C_2)$	M-Γ-X-P, N	5.51	4.93
		$(V_9\text{-}C_1)$	M-Γ-X, P-N	2.84	5.16

Table III. 10: Peak positions of the ε_2^{xx}spectrum for $Tl_2CdSnSe_4$, along with the prominent interband transition contributions for each peak in their location within the Brillouin zone. Bands are counted downward (upward) from the top (bottom) of the valence (conduction) band

Optical structure		Dominant interband transition contributions			
Peak	Position	Transition	Region	Percentage	Position
E1	2.7	(V_1-C_1)	M-Γ-X, P-N	14.49	2.57
		(V_2-C_1)	X-M-Γ-X-P-N	15.75	2.73
E2	3.71	(V_1-C_2)	M-Γ-X-P, N-Γ	2.61	3.79
		(V_1-C_3)	M-Γ-X-P	4.15	3.34
		(V_2-C_2)	X-M-Γ-X-P	4.15	3.1
		(V_3-C_1)	M-Γ-X, N-Γ	6.03	3.14
		(V_4-C_1)	M-Γ-X, P-N	5.57	3.20
		(V_5-C_1)	X-M-Γ, X-P	4.74	3.10
		(V_6-C_1)	X-M-Γ-X-P	9.56	3.61
		(V_7-C_1)	X-M-Γ	2.95	3.79
E3	4.29	(V_1-C_3)	M-Γ-X-P, N-Γ	3.59	4.13
		(V_2-C_3)	M-Γ-X-P	7.94	4.28
		(V_3-C_2)	M-Γ-X-P-N-Γ	2.64	4.19
		(V_4-C_2)	M-Γ-X-P-N-Γ	3.45	3.95
		(V_8-C_1)	X-M-Γ,X-P-N	3.44	4.32
E4	4.65	(V_1-C_4)	M-Γ-X-P-N-Γ	4.81	4.55
		(V_1-C_5)	M-Γ-X-P, N-Γ	2.31	4.88
		(V_1-C_6)	M-Γ-X-P	2.57	4.73
		(V_2-C_4)	M-Γ-X-P-N-Γ	4.98	4.80
		(V_3-C_3)	M-Γ-X-P, N-Γ	4.15	4.58
		(V_3-C_4)	M-Γ-X-P, N-Γ	3.35	4.89
		(V_4-C_3)	M-Γ-X-P, N-Γ	2	4.79
		(V_9-C_1)	X-M-Γ, X-P-N	2.35	4.60
E5	5.34	(V_1-C_6)	M-Γ-X-P, N-Γ	2.86	5.14
		(V_1-C_7)	X-M-Γ, X-P, N-Γ	2.19	5.49
		(V_1-C_8)	X-M-Γ	2.09	5.24
		(V_2-C_5)	M-Γ-X-P, N-Γ	2.76	5.05
		(V_2-C_6)	X-M-Γ-X-P-N-Γ	6.53	5.31
		(V_2-C_7)	X-M-Γ, X-P, N-Γ	3.3	5.66
		(V_3-C_5)	M-Γ-X-P	3.13	5.13
		(V_3-C_6)	X-M-Γ	4.74	5.36
		(V_4-C_4)	M-Γ-X-P-N-Γ	2.29	5.06
		(V_4-C_5)	M-Γ-X-P	2.19	5.33
		(V_4-C_6)	M-Γ-X-P-N-Γ	3.17	5.70
		(V_5-C_4)	M-Γ-X-P-N-Γ	3.2	5.44
		(V_5-C_6)	X-M-Γ-X-P	3.19	5.74
		(V_6-C_4)	X-M-Γ-X-P	3.75	5.29
		(V_6-C_6)	X-M-Γ-X-P	3.9	5.99

Table III. 11: Peak positions of the ε_2^{zz}spectrum for $Tl_2CdSnSe_4$, along with the prominent interband transition contributions for each peak in their location within the Brillouin zone. Bands are counted downward (upward) from the top (bottom) of the valence (conduction) band

Optical structure		Dominant interband transition contributions			
Peak	Position	Transition	Region	Percentage	Position
E1	3.24	(V_2-C_1)	M-Γ-X, N-Γ	9.70	3.02
		(V_2-C_2)	X-M-Γ-X-P	3.46	3.12
		(V_3-C_1)	M-Γ-X, N-Γ	22.0	3.13
		(V_4-C_1)	M-Γ-X, P-N	16.4	3.21
		(V_5-C_1)	X-M-Γ, X-P	8.78	3.19
E2	3.8	(V_3-C_2)	M-Γ-X-P-N-Γ	4.02	4.02
	4.06	(V_4-C_2)	M-Γ-X-P-N-Γ	2.84	3.93
		(V_5-C_2)	X-M-Γ-X-P	1.90	3.96
		(V_6-C_1)	X-M-Γ-X-P	5.79	3.62
		(V_6-C_2)	X-M-Γ-X-P	5.88	4.06
		(V_7-C_1)	X-M-Γ, X-P	4.80	3.80
E3	4.24	(V_1-C_3)	M-Γ-X-P	1.99	4.12
	4.45	(V_1-C_5)	X-M-Γ, X-P	1.78	4.30
		(V_2-C_3)	M-Γ-X-P	6.5	4.27
		(V_2-C_4)	X-M-Γ-X-P	2.34	4.45
		(V_3-C_3)	M-Γ-X-P	5.03	4.33
		(V_5-C_2)	M-Γ-X-P-N-Γ	2.16	4.33
E4	4.55	(V_1-C_4)	M-Γ-X-P-N-Γ	2	4.55
	4.9	(V_4-C_4)	X-M-Γ-X-P	3.49	4.77
		(V_5-C_3)	X-M-Γ-X-P	2	4.9
		(V_6-C_3)	M-Γ-X-P, N-Γ	3.72	5.24
		(V_7-C_2)	M-Γ-X-P-N-Γ	3.77	4.70
		(V_8-C_1)	M-Γ-X, N-Γ	6.84	4.84
		(V_9-C_1)	X-M-Γ, X-P-N	4.66	4.63
E5	5.5	(V_2-C_7)	X-M-Γ, X-P, N-Γ	3.42	5.67
		(V_3-C_6)	M-Γ-X-P-N-Γ	2.17	5.55
		(V_4-C_6)	M-Γ-X-P	2.28	5.60
		(V_5-C_6)	X-M-Γ, X-P-N-Γ	3.37	5.72
		(V_6-C_4)	M-Γ-X-P	2.27	5.69
		(V_{11}-C_1)	M-Γ-X, P-N	4.13	5.83

The absorption coefficient α(ω), which is an important optical parameter quantifying the fraction of energy of incident radiation of frequency ω absorbed per unit length when it passes through a medium, is a key parameter in terms of possible implications of a semiconductor in optoelectronic devices. The calculated $\alpha^{xx}(\omega)$ and $\alpha^{zz}(\omega)$ spectra, components of the absorption coefficient α(ω) that correspond to incident electromagnetic radiation polarized parallel to the a and c-axes, respectively, are illustrated in Fig. 9a. Both the $\alpha^{xx}(\omega)$ and $\alpha^{zz}(\omega)$ curves consist of one structure extending from the absorption edge, which corresponds to the lower allowed electronic interband direct transition, up to the considered energy range. The $\alpha^{xx}(\omega)$ and $\alpha^{zz}(\omega)$ spectra start to increase sharply from the same absorption edge but at different rates; the $\alpha^{xx}(\omega)$ spectrum grows more rapidly than the $\alpha^{zz}(\omega)$ curve. Figure 9a clearly shows that in the low energy range (lower than 3.25 eV for $Tl_2CdGeSe_4$ and lower than 2.92 eV for $Tl_2CdSnSe_4$), the amplitude of the $\alpha^{xx}(\omega)$ spectrum is slightly higher than that of the $\alpha^{zz}(\omega)$ spectrum, indicating that the edge of the bandgap is somewhat anisotropic. The amplitudes of α(ω) spectra of the studied compounds are higher than (10^4cm^{-1}) in an energy range including the visible spectrum and higher than (10^5cm^{-1}) in a wide energy window extending approximately from 2.34 (2.53) eV up to the considered energy range (20 eV). In the case of $Tl_2CdGeSe_4$ for E//a (E// c) and from 2.28 (2.52) eV up to the considered energy range in the case of $Tl_2CdSnSe_4$ for E//a (E// c), suggesting that these materials could be potential candidates for optoelectronic devices operating in a wide energy range from the visible spectrum to the UV range. The α(ω) spectrum reaches a maximum magnitude of approximately 1.5×10^6 cm^{-1} at approximately 6.5 eV in both studied E// c materials. Figure 9b represents the frequency-dependent curves of $n^{xx}(\omega)$ and $n^{zz}(\omega)$, components of the refractive index n(ω), another important optical parameter describing the refraction of electromagnetic radiation propagating through a medium [55]. Figure 9b shows that both investigated compounds' refractive indices n(ω) are considerably anisotropic. The static components, $n^{xx}(0)$ and $n^{zz}(0)$, of the static refractive index, n(0), are equal to 2.88 (2.93) and 2.98 (3.05), respectively, for $Tl_2CdGeSe_4$ ($Tl_2CdSnSe_4$). The $n^{xx}(\omega)$ spectrum exhibits two summa, $n^{xx}_{summ-1}(\omega) = 3.46(3.60)$ at 2.38 (2.38)eV and $n^{xx}_{summ-2}(\omega)3.50(3.49)$ at 3.24 (3.16)eV for $Tl_2CdGeSe_4$ ($Tl_2CdSnSe_4$), while $n^{zz}(\omega)$ exhibits one summa, $n^{zz}_{summ}(\omega) = 3.98(4.20)$ at 3.31 (3.05)eV for $Tl_2CdGeSe_4$ ($Tl_2CdSnSe_4$). The frequency-dependent curves of the components of the optical reflectivity R(ω), namely, $R^{xx}(\omega)$ and$R^{zz}(\omega)$, of the title compounds are shown in Fig. 9c.

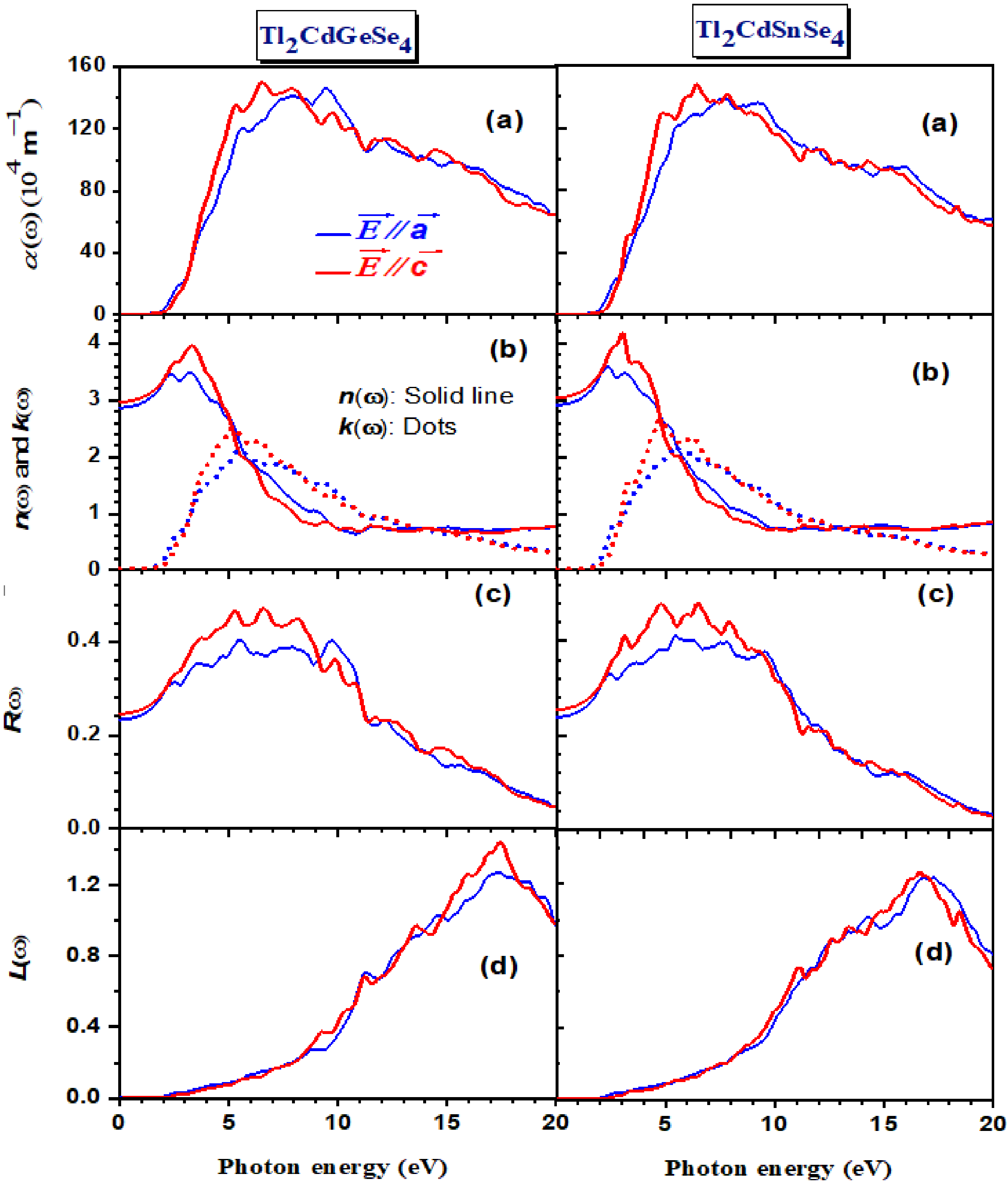

Figure III.9: Calculated frequency-dependent curves of the absorption coefficient α(ω), b refractive index n(ω) and extinction coefficient k(ω), c reflectivity R(ω) and d energy-loss function L(ω) for the $Tl_2CdGeSe_4$ and $Tl_2CdSnSe_4$ materials

It is noted that the R(ω) spectra of $Tl_2CdGeSe_4$ and $Tl_2CdSnSe_4$ are characterized by a notable anisotropy in the energy range of 0–9 eV; the amplitude of $R^{zz}(\omega)$ is clearly higher than that of $R^{xx}(\omega)$ in this energy window. The amplitudes of the $R^{xx}(\omega)$ and $R^{zz}(\omega)$ spectra become too close and decrease rapidly toward zero value in the energy range of 10—20 eV. The components of the static reflectivity, viz., $R^{xx}(0)$ and $R^{zz}(\omega)$, are equal to approximately 23 (24)% and 25 (26)%, respectively, for $Tl_2CdGeSe_4$ ($Tl_2CdSnSe_4$). The optical reflectivity$R^{zz}(\omega)$ is higher than $R^{xx}(\omega)$ by 40% in a large energy window expanding from approximately 3.5 eV to 8.9 eV.

The spectra of $L^{xx}(\omega)$ and $L^{zz}(\omega)$, components of the electron energy-loss function L(ω), an optical parameter describing the energy lost by fast electrons traversing a homogeneous dielectric material, are illustrated in Fig. 9d. The main peak of L(ω) spectra is usually associated with the plasma frequency ωp. The $L^{xx}(\omega)$ and $L^{zz}(\omega)$ spectra exhibit a maximum centered at approximately 17.5 (16.7) eV, which is associated with the plasma oscillations in $Tl_2CdGeSe_4$ (Tl2CdSnSe4). The main structures in the $L^{xx}(\omega)$ and $L^{zz}(\omega)$ spectra correspond to the trailing edges in the $R^{xx}(\omega)$ and $R^{zz}(\omega)$ spectra, respectively.

References

[1] S.J. Clark, M.D. Segall, C.J. Pickard, P.J. Hasnip, M.J. Probert, K. Refson, M.C. Payne, *First principles methods using CASTEP*, J. Z. Kristallogr. Vol. 220, pp. 567–570, 2005

[2] J.P. Perdew, A. Ruzsinszky, G.I. Csonka, O.A. Vydrov, G.E. Scuseria, L.A. Constantin, X. Zhou, K. Burke, *Restoring the density-gradient expansion for exchange in solids and surfaces.* Phys. Rev. Lett. Vol. 100, pp. 136406–136414, 2008

[3] J.S. Lin, A. Qteish, M.C. Payne, V. Heine, *Optimized and transferable nonlocal separable ab initio pseudopotentials*, Phys. Rev. B, Vol. 47, pp. 4174–4180, 1993

[4] S.B. Zhang, L.W. Shi, Comput. Mater. Sci. 142, 99 (2018)

[5] H.J. Monkhorst, J.D. Pack, *Special points for Brillouin zone integrations*, Phys. Rev. B, Vol. 13, pp. 5188–5192, 1976

[6] B.G. Pfrommer, M. Cˆot´e, S.G. Louie, M.L. Cohen, *Relaxation of crystals with the quasi-Newton method*, J. Comput. Phys. Vol. 131, pp. 233–240, 1997

[7] S. Baroni, S. de Gironcoli, A. Dal Corso, P. Giannozzi, *Phonons and related crystal properties from densityfunctional perturbation theory*, Rev. Mod. Phys, Vol. 73, pp. 515–562, 2001

[8] P. Blaha, K. Schwarz, F. Tran, R.T. Laskowski, G.K.H. Madsen, L.D. Marks, *WIEN2k: an APW+lo program for calculating the properties of solids*, J. Chem. Phys, Vol. 152, pp. 74101–74130, 2020

[9] F. Tran, P. Blaha, *Accurate band gaps of semiconductors and insulators with a semilocal exchangecorrelation potential*, Phys. Rev. Lett, Vol. 102, pp. 226401–226404, 2009

[10] D. Koller, F. Tran, P. Blaha, *Improving the modified Becke–Johnson exchange potential*, Phys. Rev. B, Vol. 85, pp. 155109, 2012

[11] D. Koller, F. Tran, P. Blaha, *Merits and limits of the modified Becke-Johnson exchange potential*, Phys. Rev. B, Vol. 83, pp. 195134–195210, 2011

[12] D.J. Singh, S.S.A. Seo, H.N. Lee, *Optical properties of ferroelectric* $Bi_4Ti_3O_{12}$, Phys. Rev. B, Vol. 82, pp. 180103(R) – 180104, 2010

[13] J.A. Camargo-Martinez, R. Baquero, *Performance of the modified Becke–Johnson potential for semiconductors*, Phys. Rev. B, Vol. 86, pp. 195106–195108, 2012

[14] A.O. Selezen, L.V. Piskach, O.V. Parasyuk, I.D. Olekseyuk, *The* Tl_2SnSe_3*-CdSe system and the crystal structure of the* $Tl_2CdSnSe_4$ *compound*, J. Phase Equilib. Diffus. Vol. 40(6), pp. 797–801, 2019

[15] A.O. Selezen, I.D. Olekseyuk, G.L. Myronchuk, O.V. Smitiukh, L.V. Piskach, *Synthesis and structure of the new semiconductor compounds* $Tl_2BII\text{-}DIV\text{-}X_4$ *(BII–Cd, Hg; DIV–Si, Ge; X–Se, Te) and isothermal sections of the* $Tl_2Se–CdSe–Ge(Sn)Se_2$ *systems at 570 K.* J. Solid State Chem. Vol. 289, pp. 121422–121427, 2020

[16] T.V. Vu, A.A. Lavrentyev, B.V. Gabrelian, A.O. Selezen, L.V. Piskach, G.L. Myronchuk, M. Denysyuk, V.A. Tkach, K.D. Pham, O.Y. Khyzhun, *Crystal growth, electronic and optical properties of* $Tl_2CdSnSe_4$*, a recently discovered prospective semiconductor for application in thin film solar cells and optoelectronics*, J. Opt. Mater, Vol. 111, pp. 110656–110712, 2021

[17] A. Gutzmann, C. Nather, W. Bensch, K4Vp2S9. Acta Cryst. C 60, i11–i13 (2004)

[18] J. F. Nye, *Proprties physiques des cristaux*, Dunod, 1961.

[19] F. Mouhat, F.-X. Coudert, *Necessary and sufficient elastic stability conditions in various crystal systems*, Phys. Rev. B, Vol. 90, pp. 224104–224114, 2014

[20] Yu. A. Amenzade, *Theory of Elasticity*, 1979

[21] S. Pugh, *Relations between the elastic moduli and the plastic properties of polycrystalline pure metals.* Philos. Mag, Vol. 7, pp. 823–843, 1954

[22] M . Z. Hasan, K. M. Hossain, S. K. Mitro, M. Rasheduzzaman, J. K. Modak, M. A. Rayhan, *Structural, mechanical, electronic, and anisotropic properties of niobium-doped strontium ferrite: frst-principle calculations*, J. Applied Physics A, 2021

[23] W. Voigt, reprinted, *With an Additional Appendix, Johnson Reprint*, Leipzig, Teubner, New York, 1928, 1966

[24] F. Litimein, R. Khenata, A. Bouhemadou, Y. Al-Douri, S. Bin Omran, *First-principle calculations to investigate the elastic and thermodynamic properties of* $RBRh_3$ *(R=Sc, Y and La) perovskite compounds*, Molecular Physics Vol. 110, No. 2, 121–128, 2012

[25] M. T. Nasir, M. A. Hadi, M. A. Rayhan, M. A. Ali, M. M. Hossain, M. Roknuzzaman, S. H. Naqib, A. K. M. A. Islam, M. M. Uddin, K. Ostrikov, *First-Principles Study of Superconducting ScRhP and ScIrP Pnictides*, Phys. Status Solidi B, 2017.

[26] Z. Wu, E. Zhao, H. Xiang, X. Hao, X. Liu, J. Meng, *Crystal structures and elastic properties of superhard* IrN_2 *and* IrN_3 *from first principles*, Phys. Rev. B, Vol. 76, pp. 54115–54215, 2007

[27] X.Q. Chen, H. Niu, D. Li, Y. Li, *Intermetallics*, 19-1275, 2011

[28] Y.X. Wang, Appl. Phys. Lett. 91-101904, 2007

[29] H. Ozisik, E. Deligoz, K. Colakoglu, G. Surucu, Chin. Phys. B,Vol. 22, 2013

[30] X. Gao, Y. Jiang, R. Zhou, J. Feng, J. Alloy Comp, pp. 587-819, 2014

[31] S.K. Saha, G. Dutta, *Elastic and thermal properties of the layered thermoelectrics BiOCuSe and LaOCuSe*. Phys. Rev. B, Vol. 94, 125209–125218, 2016

[32] O.L. Anderson, *A simplified method for calculating the Debye temperature from elastic constants*, J. Phys. Chem. Solids, Vol. 24, pp. 909–917, 1963

[33] M. Alouani, R. C. Albers, and M. Methfessel, *Calculated elastic constants and structural properties of Mo and* $MoSi_2$, Phys. Rev. B, Vol. 43, No 8, pp. 6500, 1991

[33] A. Reuss, *Berechnung der Fließgrenze von Mischkristallen auf Grund der Plastizitätsbedingung für Einkristalle*, Z. angew. Math. Mech., Vol. 9, No. 1, pp. 49-58, 1929

[34] R. Hill, *The elastic behavior of a crystalline aggregate*. Proc. Phys. Soc. A 65, 349–354 1952

[35] K. Boudiaf, A. Bouhemadou, O. Boudrifa, K. Haddadi, F. S. Saoud, R. Khenata, Y. Al-Douri, S. Bin-omran, M.A. Ghebouli, *Structural, Elastic, Electronic and Optical Properties of LaOAgS-Type Silver Fluoride Chalcogenides: First-Principles Study*, *Journal of Electronic Materials*, 2017

[36] C. Ambrosch-Draxl, J.O. Sofo, *Linear optical properties of solids within the full-potential linearized augmented planewave method*. Comput. Phys. Commun, Vol. 175, pp. 1–14, 2006

[37] Y. Tian, B. Xu, Z. Zhao, *Microscopic theory of hardness and design of novel superhard crystals*. Int. J. Refract. Hard Met. Hard Mater, Vol. 33, pp. 93–106, 2012

[38] Q.-J. Liu, Z.-T. Liu, L.-P. Feng, *Elasticity, electronic, chemical bonding and optical properties of monoclinic ZrO_2 from first-principles*. Phys. B, Vol. 406, pp. 345–350, 2011

[39] S. Chen, Y. Sun, Y.-H. Duan, B. Huang, M.-J. Peng, *Phase stability, structural and elastic properties of C15- type Laves transition-metal compounds MCo_2 from first-principles calculations*, J. Alloys Compd, Vol. 630, pp. 202–208, 2015

[40] S. Pugh, *Relations between the elastic moduli and the plastic properties of polycrystalline pure metals*, Philos. Mag, Vol. 7, pp. 823–843, 1954

[41] E. Langenberg, E. Ferreiro-Vila, V. Lebor´an, A.O. Fumega, V. Pardo, F. Rivadulla, *Analysis of the temperature dependence of the thermal conductivity of insulating single crystal oxides*. Appl. Phys. Lett. Mater. 4, 104815–104819, 2016

[42] P. Ravindran, L. Fast, P.A. Korzhavyi, B. Johansson, *Density functional theory for calculation of elastic properties of orthorhombic crystals: application to $TiSi_2$*, J. Appl. Phys. 84, 4891–4904, 1998

[43] H. Ledbetter, A. Migliori, *A general elastic-anisotropy measure*, J. Appl. Phys. 100, 063516–063525, 2006

[44] D.-D. Pang, X.-Q. Huang, H.-Y. Xue, C. Zhang, Z.-L. Lv, M.-Y. Duan, *Properties of a predicted tetragonal carbon allotrope: first principles study. Diam. Relat. Mater*. 82, 50–55, 2018)

[45] S.I. Ranganathan, M. Ostoja-Starzewski, *Universal Elastic Anisotropy Index*, Phys. Rev. Lett. 101, 055504–055514, 2008

[46] D.H. Chung, W.R. Buessem, in: *Anisotropy in Single Crystal Refractory Compounds*, vol. 2, ed. by F.W. Vahldiek, S.A. Mersol (Plenum Press, New York, 1968), pp. 217–245

[47] W. A. Harrison, *electronic structure and the properties of solids, the physics of the chimicsl bond*, Stanford university, New York, 1989

[48] S. L. Altmann, Band Theory of Solids - An Intro. from the Point of View of Symmetry, Oxford University Press Inc., New York (USA), (1991).

[49] J. Singleton, *Band Theory and Electronic Properties of Solids*, Oxford University Press Inc., New York (USA), 2001

[50] R. Singh, *Excitons in Semiconductor Quantum Wells Studied Using Two Dimensional Coherent Spectroscopy*, Doctorat these, University of Colorado Boulder, 2013

[51] J.F. Nye, *Properties of Crystals*, Oxford University Press, Oxford, 1985

[52] Q. J. Liu, Z. –T. Liu, L. P. Feng, H. Tian, *First-principles study of structural, elastic, electronic, and optical properties of g-*TeO_2, Physica B, 405, pp. 3159–3163, 2010

[53] M. Dadsetani, A. Pourghazi, *Optical properties of strontium monochalcogenides from first principles*, Phys. Rev. B, 73-195102, 2006

[54] O. Boudrifa, A. Bouhemadou, S¸ U˘gur, R. Khenata, S. Bin-Omran, Y. Al-Douri, *Structural, electronic, optical and elastic properties of the complex* K_2PtCl_6*-structure hydrides ARuH6 (A = Mg, Ca, Sr and Ba): first-principles study*. Philos. Mag. 96, 2328–2361, 2016

[55] T.V. Vu, A.A. Lavrentyev, B.V. Gabrelian, A.O. Selezen, L.V. Piskach, G.L. Myronchuk, M. Denysyuk, V.A. Tkach, K.D. Pham, O.Y. Khyzhun, *Crystal growth, electronic and optical properties of* $Tl_2CdSnSe_4$*, a recently discovered prospective semiconductor for application in thin film solar cells and optoelectronics*. Opt. Mater. 111, 110656–110712, 2021

[56] D.R. Penn, *Wave-number-dependent dielectric function of semiconductors*. Phys. Rev. 128, 2093, 1960

Conclusion

Conclusion

In this thesis, we presented an ab-initio study of the structural, elastic, electronic, and optical properties of the considered quaternary thallium selenide systems, namely $Tl_2CdSnSe_4$ and Tl_2dGeSe_4. We used the pseudopotential plane wave (PP-PW) approach based on density functional theory as incorporated in the Cambridge Sequential Total Energy Package (CASTEP) in the optimized structural parameters and monocrystalline elastic constants. While the calculations of the electronic and optical properties were carried out through the full-potential (linearized) augmented plane wave plus local orbitals (FP-L/APW + lo) as implemented in the WIEN2k code. The exchange-correlation interactions were modeled using the PBEsol form of the general gradient approximation (labeled GGA-PBEsol or GGA-08) and TB-mBJ approximation. The obtained results can be summarized as follows:

1. **Structural properties:**

The optimized structural parameters are in excellent agreement with the experimental counterparts, confirming the reliability of the theoretical method used to predict the physical properties of the title compounds, the maximum relative discrepancy does not exceed − 0.8% when spin–orbit coupling is included.

2. **Elastic properties:**

Analysis of the monocrystalline elastic constants reveals that the investigated materials are mechanically stable, soft, and substantially structurally and elastically anisotropic.

- The C_{11} is smaller than the C_{33} value, so the crystal is more compressible along the a-axis than along the c-axis. This result indicates that the interatomic bonds along the a-axis are weaker than those along the c-axis
- The C_{11} and C_{33} values are larger than those of C_{12}, C_{13}, C_{44}, and C_{66}, which characterize the resistance to shear deformations, indicating that the studied compounds are more resistant to compression than to shear.
- The sound wave velocity is closely linked to the lattice thermal conductivity; the relatively low values of the anisotropic sound wave velocities suggest that the lattice thermal conductivities of both considered compounds are lower.

- The isotropic elastic moduli B, G, and E have relatively small values, reflecting the low hardness and stiffness of the considered materials.
- The B value is practically double that of G, suggesting that shear deformation can occur more easily than volume change and that G is the decisive elastic modulus affecting the mechanical stability of the title compound
- According to Poisson's ratio (σ), $Tl_2CdGeSe_4$ is rather ductile, while $Tl_2CdSnSe_4$ is on the border between ductile and brittle.
- Based on B/G ratio values, $B/G \approx 2.08$ for $Tl_2CdGeSe_4$ and $B/G \approx 1.74$ for $Tl_2CdSnSe_4$, confirm the results already obtained through Poisson's ratio, i.e., that $Tl_2CdGeSe_4$ is ductile and $Tl_2CdSnSe_4$ is on the border between ductility and brittleness.
- A ductile material is easily machinable and resistant to thermal shock
- Based on Poisson's ratio (for a covalent material is 0.2, while it is in the range of 0.3–0.4 for an ionic material and equal to 0.5 for the pure-ionic limit) $Tl_2CdGeSe_4$, with$\sigma = 0.285$, and $Tl_2CdGeSe_4$, with $\sigma = 0.259$, exhibit a mixture of covalent and ionic interatomic bonds, but the ionic character is dominant.
- The low values of the average velocity V_m and the Debye temperature T_D denote a low thermal conductivity for the studied compounds.
- These compounds are characterized by a large shear anisotropy, where $A_1,\ A_2$and $A_3$are equal to 0.52 and 0.84 (0.67 and 1.15), respectively, for $Tl_2CdGeSe_4$ ($Tl_2CdSnSe_4$).
- The ratios of the linear compressibility βc/βa are equal to 0.39 for $Tl_2CdGeSe_4$ and 0.52 for $Tl_2CdSnSe_4$, highlighting the strong anisotropy of the linear compressibility in both studied compounds.
- The computed value of universal elastic anisotropy A^U equal to 0.51 for $Tl_2CdGeSe_4$ and 0.60 for $Tl_2CdSnSe_4$, confirming that the title compounds are characterized by considerable elastic anisotropy.
- Anisotropy in compression A_{comp} and in shear A_{shear} are equal to 4.0% and 4.6%, respectively, for $Tl_2CdGeSe_4$ and 2.3% and 2.4%, respectively, for $Tl_2CdSnSe_4$, these indicators highlight the strong elastic anisotropy in the compression and shear of the title compounds.

3. **<u>Electronic properties:</u>**

Analysis of the energy band dispersions and the density of states diagrams shows that the studied materials are direct bandgap semiconductors, the upper valence band dominantly originates from the Se-4p states, and the Se-Tl, Se-Cd, Se-Ge, and Se-Sn bonds dominantly have an ionic character with a certain degree of covalency.

- The energy band dispersions calculated using GGA-08 and TB-mBJ have similar general characteristics, but they are significantly different with regard to the bandgap values.
- The TB-mBJ potential considerably improves the bandgap value, but it is still somewhat smaller than its experimental counterpart. The inclusion of the spin–orbit coupling reduces the bandgap.
- Small differences in the structural parameters could sometimes produce, for the same semiconductor, an appreciable difference in the calculated bandgap.
- The energy band around the CBM is slightly less dispersive than that around the VBM, indicating that the electron effective mass is somewhat greater than that of the holes.
- The effective masses of electrons and holes exhibit a very weak anisotropy; the electron and hole effective masses toward the M → Γ direction are approximately equal to the corresponding masses toward the M → X direction.
- The inclusion of SOC in the calculations somewhat increases the electron and hole effective masses.

4. <u>Optical properties:</u>

The frequency-dependent linear optical functions, viz., complex dielectric function, refractive index, optical reflectivity, and energy-loss function, were determined for incident photons with energies between 0 and 20 eV.

- The ε2(ω) spectra of both compounds exhibit notable anisotropy.
- The studied materials exhibit a high absorption in an energy window involving the visible spectrum. A tentative analysis was performed to determine the microscopic origin of the observed optical structures in the imaginary part of the dielectric function.
- In the low energy range (lower than 3.25 eV for $Tl_2CdGeSe_4$ and lower than 2.92 eV for $Tl_2CdGeSe_4$), the amplitude of the $\alpha_{xx}(\omega)$ spectrum is slightly higher than that of the $\alpha_{zz}(\omega)$ spectrum, indicating that the edge of the bandgap is somewhat anisotropic.
- these materials could be potential candidates for optoelectronic devices operating in a wide energy range from the visible spectrum to the UV range.
- a larger bandgap corresponds to a smaller static dielectric constant.

Appendix

Appendix

A.1. CASTEP Code

The name, CASTEP stands for "Cambridge Serial Total Energy Package". This package was developed in 1990s by Professor Mike Payne and his team at Cambridge University and then it was completely redesigned from the ground up in 2004 [1]. Serial means to run on serial processors, now it can be run in parallel computers as well. CASTEP employs the density functional theory within the plane-wave pseudopotential approach. Here is a guide on how to calculate structural properties using CASTEP

- Prepare the input file: the file should contain the structural parameter of the material studied, atomic coordinates, and other relevant such as K-point, and energy cut-off. You can use .cell or .cif file format for input file
- Run the calculation: using a graphical user interface in Materials Studio. The calculation may take hours or days depending on the complexity of the system
- Analyses the results: using CASTEP analysis tools

Using this ab initio code, one can calculate:

- lattice constants, atomic positions, bond lengths, and bond angles.
- Electronic density of state provided information about the distribution of energy levels in the material, Band structures, electron density, electron localization function, and electron density difference.
- optical properties; dielectric function, absorption coefficient, loss function, reflectivity, refractive index, …
- Phonon dispersion spectra and phonon density diagram, from which one can determine the dynamical stability and thermal properties of the material.
- anisotropic elastic constants of the material and isotropic elastic moduli, which can be used to compute other related properties like material hardness, minimum thermal conductivity, fracture toughness, and melting point, …

Optimize the crystalline structure: The steps involved in setting up a relaxation calculation in CASTEP are as follows:

- Define the optimization parameters (to obtain a stable structure): using the input "geometry optimization" keyword. This allows you to specify the optimization method, convergence criteria, and other relevant parameters. CASTEP offers several relaxation methods for optimizing the structure of the system including the Broyden-Fletcher-Goldfarb-Shanno (BFGS) method.

- Specify the unit cell before you choose the exchange-correlation functional
- Choose cell optimization: full, fix volume, fix shape. By default, CASTEP will perform a full relaxation of the atomic positions and cell parameters.
- Specify the relaxation method (BFGS or LBFGS); the user should select the method that is most appropriate for their system. You can add the Pressure effect (hydrostatic pressure).
- Choose pseudopotential, the best cut-off energy and k-point
- Set the convergence criteria, including the maximum number of SCF cycles (dependent on material), the tolerance for the total energy, and the tolerance for the electronic density.
- Run the optimization process.

BFGS Geometry optimization method:

By default, CASTEP uses the BFGS geometry optimization method. The BFGS minimizer is a method used to find the minimum energy configuration of a system by iteratively adjusting the atomic positions. BFGS stands for Broyden-Fletcher-Goldfarb-Shanno, which is a quasi-Newton optimization algorithm. It uses the gradient of the energy function concerning the atomic positions to iteratively improve the configuration of the system until a minimum energy state is reached. The algorithm maintains an approximation of the inverse Hessian matrix of the energy function, which allows it to estimate the optimal direction to move in at each iteration. BFGS is a popular choice due to its relatively low computational cost and robustness in finding local minima. However, other minimization algorithms may also be available in CASTEP, depending on the specific version and settings used.

To Calculate elastic constants C_{ij}: you can follow the following steps:

- Prepare the input file and optimize the crystalline structure with full relaxation.
- Define the elastic constants: You can define several distorted structures generated for each strain pattern. Displays a matrix showing the nonzero components of the strain tensor for each generated strain.
- Run, then analyze.

Generally, CASTEP is more efficient for large systems due to the use of plane-wave basis sets and pseudopotentials, which can simplify the computation. Well-suited for systems with a large number of atoms or complex periodic structures. Often considered more user-friendly with extensive documentation and support. Integrated with many graphical user interfaces and scripting options for ease of use.

A.1. Wien2k Code

The name Wien2k originates from Vienna University, where Karlheinz Schwarz and Peter Blaha developed the program. The first version was called WIEN and it was published in 1990 [2]. “2k” refers to the fact that the code was rewritten in the early 2000s to take advantage of new computational technologies and advances in DFT methods. The code is based on the full-potential linearized augmented plane wave (FLAPW) method, which considers all electrons (core and valence) self-consistently. It has been running on LINUX (UNIX) system. The code has been updated continuously and improved over the years with the addition of new features and capabilities. It is highly flexible and adaptable with a wide range of options in the interface for calculating various properties. Some of the key features of Wien2k include:

- Self-consistent field calculation: it is an iterative SCF approach to solving the Kohn-Sham equation of DFT to accurately predict the properties of the material studied.
- Relativistic effects can be used such as spin-orbit coupling, which is used in heavy elements.
- Multiple basis sets, LAPW and APW+lo, which allow it accurate model.
- Wien2k can calculate structural, elastic, electronic, optical, thermoelectric, thermodynamic (should add BoltezTrap code and Gibbs2 program, and magnetic properties.

To optimize the crystal structure using Wien2k, you can follow these basic steps:

- Prepare the structural file, that contains the position atomic, lattice parameter, and space group, and choose the reduction of rayon and save for found case. struct file.
- Do initialization by the command ‘init_lapw’ in a terminal window or in the interface (running consists of NN, SG, SYMMETRY, LSTART, KGEN, and DSTART). This will create a new directory for the calculation, where all the input and output will be stored.

- Set up the input files: In the new directory, you need to create the input files for the optimization calculation. The main input file is typically called case.in1, and it should contain the details of the calculation, including the optimization method, convergence criteria, and other parameters. You also need to specify the k-point mesh for the Brillouin zone sampling, as well as the basis set and other details of the calculation.
- Run the optimization: input the change in volume “-10; -5; 0; 5; 10”, choose “xdstart “ , then change the command "run_lapw –p F 0.5 -i 500 -ec 0.0001 -min". This will run the self-consistent field (SCF) calculation for a maximum of 500 iterations, and it will stop the calculation once the energy convergence criteria of 0.0001 were reached.
- Analyze the results: Once the optimization calculation is complete, you can analyze the results to see if the crystal structure has been optimized. The output files will contain information about the optimized structure, including the atomic positions, lattice constants, and energy. You can use a program like XCRYSDEN to visualize the optimized structure and compare it with the original structure.
- Repeat if necessary: If the structure has not been fully optimized, you can repeat the optimization calculation with different parameters or methods until convergence is achieved.

If you have an internal coordinate in your material, you should optimize it: you can do the same thing just change in initialization the option ‘optimize position’.

Wien2k can be more computationally intensive due to the full-potential treatment, which requires more basis functions and can be more demanding in terms of memory and processing power. Provides very accurate results, making it suitable for smaller systems where high precision is critical. Requires more expertise to set up and run, as it involves more complex input and configuration files. Preferred by researchers who require precise control over their calculations and are experienced in electronic structure methods.

A.3. Spin-Orbit Coupling

Spin-orbit coupling (SOC) is a crucial element in the in-depth exploration of quantum systems. It refers to the interplay between a particle's spin and its motion, causing modifications in the electron's atomic energy levels, leading to the splitting of spectral lines. This phenomenon is a result of the electromagnetic interaction between the electron's spin and the electric field of the nucleus through which it moves. In a solid as in atomic physics, the dominant contribution to spin-orbit Pauli is from the motion in the bare Coulomb potential in the innermost region of the atomic cores.

The Hamiltonian for a single electron, taking into account the spin-orbit interaction, is expressed as:

$$H = \frac{p^2}{2m} + V(r) + \frac{\hbar}{4m^2c^2}(\nabla \mathrm{V} \times \mathrm{p}).\sigma \qquad (\mathrm{A.}\ 1)$$

The initial two terms signify the kinetic energy and periodic potential of the one-electron Hamiltonian within a basic periodic potential V (r), which mirrors the crystal symmetry. ħ is Planck's constant, *m* is the mass of a free electron, *c* is the velocity of light, and σ is the dimensionless spin operator [S = (p/2)σ]. The third term signifies the spin-orbit interaction H'_{SO}

$$H'_{SO} = \frac{\hbar}{4m^2c^2}(\nabla \mathrm{V} \times \mathrm{p}).\sigma \qquad (\mathrm{A.}\ 2)$$

Where $H = H_0 + H'_{SO}$

The Hamiltonian (A. 1) is appropriate when the spin–orbit splitting is significant compared with typical energy gaps [3].

The weak interaction spin-orbit coupling is a mixture of L and S. The orbital movement of the electron gives rise to an internal magnetic field proportional to a field, which can interact with the intrinsic magnetic moment associated with the spin of the same electron. The quantum numbers associated with the eigenvalues of the operators, of the total angular momentum, then

$$J = L + S, \dots, |L - S| \qquad (\mathrm{A.}\ 3)$$

In a crystalline solid, the behavior of electrons is described by energy bands denoted as n(k), where "n" represents the band index, and "k" is the wave vector. Spin–orbit (SO) coupling plays a significant role in shaping the energy band structure (n(k)) in such materials.

An illustrative example is found in semiconductors like GaAs, where SO interaction induces a splitting in the topmost valence band, as depicted in Fig A. 1.

In the absence of spin in a tight-binding model, the electron states at the valence band edge exhibit p-like characteristics, associated with an orbital angular momentum of 1. However, when considering spin-orbit (SO) coupling, the electronic states exhibit a total angular momentum of $L = 3/2$ and$L = 1/2$. These =$L = 3/2$ and$L = 1/2$ states are split in energy by a gap, identified as the SO gap. This serves as an illustrative example highlighting how the orbital motion of electrons within a crystal is influenced by spin–orbit coupling [4].

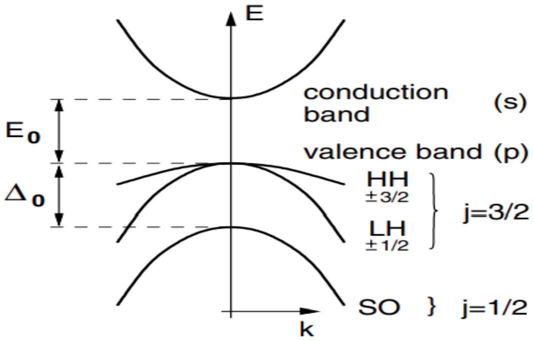

Fig. A.1: The band structure of GaAs close to the fundamental gap

The spin splitting of the Bloch states in the zinc blend structure must result from SO coupling. In addition, the effects of SOC observed in different studies in the literature like reducing the energy band gap [5], and splitting of the first degenerated conduction levels as we sow in GaAs valence band. Spin-orbit coupling can play a crucial role in determining the electronic properties of materials, such as their magnetic and transport properties. Spin-orbit coupling is also the basis for many emerging technologies, such as spintronic, which uses the spin of electrons to store and process information.

References

[1] S.J. Clark, M.D. Segall, C.J. Pickard, P.J. Hasnip, M.J. Probert, K. Refson, M.C. Payne, *First principles methods using CASTEP*, J. Z. Kristallogr, 2004

[2] P. Blaha, K. Schwarz, P. Sorantin, *Full-Potential OTENTIAL, Linearized Augmented Plane Wave Programs for Crystalline Systems*, Computer Physics Communications, Vol. 59, pp. 399-415, 1990

[3] M.S. Dresselhaus G. Dresselhaus A. Jorio, *Group Theory Application to the Physics of Condensed Matter, S*pringer-Verlag Berlin Heidelberg, ISBN 978-3-540-32897-1, 2008

[4] R. Winkler, *Spin-Orbit Coupling Effects in Two-Dimensional Electron and Hole System,* springer Tracts in Modern Physics Volume 191, ISBN 3-540-01187-0, 2003

[5] J. Even, L. Pedesseau, J. M. Jancu, and C. Katan, *Importance of spin–orbit coupling in hybrid organic/ inorganic perovskites for photovoltaic applications*, J. Phys. Chem. (2013)

Abstract

Motivated by the increasing need for high-performance semiconductor materials, we conducted a comprehensive investigation into the structural, elastic, electronic, and optical properties of two recently synthesized compounds, namely $Tl_2CdGeSe_4$ and $Tl_2CdSnSe_4$, using the full potential linearized augmented plane wave (FP-LAPW) and pseudopotential plane wave (PP-PW) employing density functional theory calculations. The calculations were carried out with the inclusion of relativistic effects, specifically accounting for spin-orbit coupling (SOC). The resulting equilibrium structural parameters obtained from the computations exhibit remarkable agreement with available measurements. It should be noted that the calculations for all the properties examined were carried out using the theoretic equilibrium lattice parameters. The obtained results for both monocrystalline and polycrystalline elastic constants indicate that the investigated compounds exhibit softness, ductility, mechanical stability, and significant structural and elastic anisotropy. By employing the Tran-Blaha modified Becke-Johnson potential and considering the inclusion of spin-orbit coupling (SOC), our calculations reveal that both $Tl_2CdGeSe_4$ and $Tl_2CdSnSe_4$ are direct bandgap semiconductors. Incorporating SOC leads to a reduction in the fundamental bandgap of $Tl_2CdGeSe_4$ from 1.123 to 0.981 eV and that of $Tl_2CdSnSe_4$ from 1.097 to 0.953 eV. The l-decomposed atom-projected densities of states were utilized to determine the individual contributions of each constituent atom to the electronic states within the energy bands. The upper valence subband predominantly arises from the Se-4p states, while the bottom of the conduction band primarily originates from the Se-4p and Ge-4p/Sn-5p states. Furthermore, frequency-dependent linear optical parameters, including the complex dielectric function, absorption coefficient, refractive index, reflectivity, and energy-loss function, were calculated across a wide energy range for electromagnetic waves polarized parallel and perpendicular to the c-axis. Efforts were made to elucidate the microscopic origins of the observed peaks and structures in the calculated optical spectra

ملخص

بدافع الحاجة المتزايدة لمواد أشباه الموصلات عالية الأداء، أجرينا تحقيقًا شاملاً في الخصائص البنيوية والمرنة والإلكترونية والضوئية لمركبين تم تصنيعهما مؤخرًا، وهما $Tl_2CdGeSe_4$ و$Tl_2CdSnSe_4$ ، ، وذلك باستخدام الموجة المستوية المتزايدة خطيا (FP-LAPW) والموجة المستوية الكاذبة (PP-PW) اللذان يستخدمان حسابات نظرية دالية الكثافة. تم إجراء الحسابات مع تضمين التأثيرات النسبية ، على وجه التحديد لحساب اقتران الدوران والمدار(SOC) . تظهرنتائج الثوابت البنيوية للتوازن التي تم الحصول عليها من الحسابات اتفاقًا ملحوظًا مع القياسات المتاحة. وتجدر الإشارة إلى أن العمليات الحسابية لجميع الخصائص التي تم فحصها أجريت باستخدام ثوابت شبكة التوازن النظري. النتائج التي تم الحصول عليها لكل من الثوابت المرنة أحادية البلورية ومتعددة التبلور تشير إلى أن المركبات التي تم فحصها تظهر ليونة ، صلابة، إستقرار ميكانيكي ، وتباين بنيوي ومرن كبير. من خلال استخدام كمون Becke-Johnson المعدلة من Tran-Blaha والنظر في ادخال اقتران مدار الدوران (SOC)، تكشف حساباتنا أن كلا من $Tl_2CdGeSe_4$ و $Tl_2CdSnSe_4$ هما أشباه نواقل ذات فجوة نطاق مباشرة. يؤدي دمج SOC إلى تقليل فجوة النطاق الأساسية لـ $Tl_2CdGeSe_4$ من 1.123 إلى 0.981 فولت وتلك الخاصة بـ $Tl_2CdSnSe_4$ من 1.097 إلى 0.953 فولت. تم استخدام كثافات الدول المتحللة لتحديد المساهمات الفردية لكل ذرة مكونة للحالات الإلكترونية داخل نطاقات الطاقة. ينشأ النطاق الفرعي التكافؤ العلوي في الغالب من حالات Se-4p، بينما ينشأ الجزء السفلي من نطاق التوصيل بشكل أساسي من حالات Se-4p و Ge-4p / Sn-5p. علاوة على ذلك ، تم حساب اطياف الدوال الضوئية المعتمدة على التردد ، بما في ذلك دالة العزل الكهربائي المعقدة ، ومعامل الامتصاص ، ومعامل الانكسار ، والانعكاسية ، ووظيفة فقدان الطاقة ، عبر نطاق طاقة واسع للموجات الكهرومغناطيسية المستقطبة المتوازية والعمودية على المحور c. بُذلت جهود لتوضيح الأصول المجهرية للقمم والتراكيب التي لوحظت في الأطياف الضوئية المحسوبة .